Some studies of gas gain measurements in proportional drift chambers

Thesis submitted in accordance with the requirements

of

the University of Liverpool

for

the degree of Master of Science

by

David Gustavo Nunn B.Sc. (Hons)

March 1991

Oliver Lodge Laboratory

University of Liverpool

Some studies of gas gain measurements in proportional drift chambers

David Gustavo Nunn B.Sc. (Hons)

March 1991

Abstract

The avalanche gas gain at the sense wires of some radial wire drift chambers (RWDC's) has been measured. The chambers were designed and constructed for the HERA H1 forward track detector. Two methods for determining the gas gain multiplication factor, G, were used. The first involved an analysis of the amplified chamber output using a 6-bit monolithic FADC, and the second involved the measurement of the proportional chambers cathode current with a sensitive ammeter. The value of G was determined for various values of electric field at the surface of the sense wires for the RWDC's and for a single wire drift chamber (SWDC).

The study shows that a gas gain of $[2.75 \pm 0.22 \pm 0.52\{syst\}] \times 10^4$ is obtained at a sense field of 170 kV/cm with a sense wire diameter of 50 μm using an Ar {50%}/C_2H_6 {50%} gas mixture. The result is consistent with expectations based upon previous measurements with different wire diameters.

A first attempt at studying the deterioration of gas avalanche gain of the SWDC sense wire with irradiation dose, has been made using a ruthenium β-source. After 1.5 months of continuous exposure, and a total charge of 0.26 C deposited per cm of the wire, no discernible deterioration was observed.

Contents

List of Figures

List of Tables

Acknowledgements

I should like to thank the Science and Engineering Council for their financial support, and the University of Liverpool for giving me the opportunity to submit this M.Sc. thesis, and Dr J.B. Dainton for his supervision and guidance.

The work would certainly not have been completed without the tremendous help and advice from the the H1 group at Liverpool, which includes Professor E. Gabathuler F.R.S., Drs G.A. Beck, S. J. Maxfield, J. M. Morton, G. D. Patel, D. P. C. Sankey, Mr C. D. King, Mr M. Wormald, and my fellow postgraduates, Lindsay Womersley, Douglas Gillespie, Roland Martin, and Alan Goodall. I would also like to thank Sandra Owen for our chats and her assistance in the presentation of this thesis.

Thanks also to Justin McCarthy, without whom this work would have been twice as difficult. His thesis [26] was invaluable in the composition of this work. The constant support, understanding, and friendship of my good pal Peter Sutton was very important, and I would sincerely like to thank him. Thanks also to Fiona Cooke and her family for their friendship. I must not forget to thank my friends from home and from Southampton University wherever they may be now.

Finally I would like to thank my Mother, Father, and brother Ian for all their support and encouragement, and for simply being great, and it is to them that this thesis is dedicated.

Radial chamber

This logo was attatched to the three radial wire drift chambers which are now embedded within the H1 detector, HERA.

References

[1] D. Newton, H1 note on the solenoid field measurements, H1-8/90-145

[2] Hunting Composite review (1989), private communication, Hunting composites

[3] Noryl: polyetherpolyphenylene plus 6% filler (titanium oxide)

[4] Permali Ltd, Gloucester, UK

[5] Ni/Cr/Al alloy manufactured by California Fine Wire Company, Grover City, Ca., USA

[6] Yeovil Circuits, Yeovil, Somerset, UK

[7] Röhm GmbH, Darmstadt, FRG

[8] W. Zimmerman, private communication

[9] W. Zimmerman, DESY, Struck F1000 FADC system

[10] Hunting Components, Havant, Hants, UK

[11] Noryl hub and templates manufactured by Marcus Engineering, Wirral, UK

[12] G.A. Beck et al., Nucl. Instr. and Meth. A283 (1989) 471

[13] G.A. Beck, Electrostatics of the radial wedge (unpublished 1987)

[14] F. Sauli, Principles of operation of multiwire proportional and drift chambers CERN 77-09 (1977)

[15] M.E. Rose and S.A. Korff, Phys. Rev. 59 (1941) 850

[16] T. Hessing and R.W. Kadel, Gas gain as a function of electric field, CDF note № 176 (1983)

[17] G.L. Salmon, Centaur Gas Gain, ZEUS-Oxford-89-7, (1989)

[18] G.A. Beck (private communication) Internal Liverpool note on Pulse Shapes

[19] Landau, J. Phys. USSR 8 (1944) 201

[20] D. Gillespie (private communication), Setting up of the 6-bit non-linear Heidelberg-Struck DL300 FADC system

[21] Valet-Plus package, Hardware Guide, OC Group-CERN, Data Handling Division

[22] D.P.C. Sankey, Ph.D. thesis, University of Liverpool, UK, 1990

[23] E. Bateman, private communication, RAL

[24] J. Adam et al., A study of ageing effects in wire chambers, CERN/EF 83-7 (1983)

[25] J.B. Dainton, private communication, Liverpool University

[26] J. McCarthy, M.Sc. thesis, University of Liverpool, UK, 1990

Chapter 1

HERA and the H1 detector

1.1 The HERA accelerator

The concept of the Hadron-Electron Ring Accelerator (HERA) began in the early 1970's at the Deutsches Elektronen-Synchrotron (DESY) in Hamburg, West Germany. Construction began at the end of May 1984 and HERA is now almost complete. It is expected that the accelerator will be switched on for first physics sometime towards the end of 1991, or early 1992. HERA is located around the DESY site in Hamburg, and only one-fifth of the machine is actually contained within the grounds of DESY (Figure 1.1.1).

HERA is an electron-proton collider. It includes two storage rings, one for electrons or positrons (energy ~ 30 GeV), and one for protons (maximum energy 820 GeV). The older rings, DESY and PETRA, have been modified, and are to be used to pre-accelerate the particles before they are injected into the main HERA rings. The electron ring of HERA is a conventional "warm" (not liquid helium cooled) accelerating ring, which can accelerate the electrons to a maximum energy of 30 GeV. The proton ring is capable of accelerating the protons to a maximum energy of 820 GeV, but requires superconducting magnets for bending and focusing the beam. A high

powered radio frequency resonator system is used to accelerate the particles to such high energies.

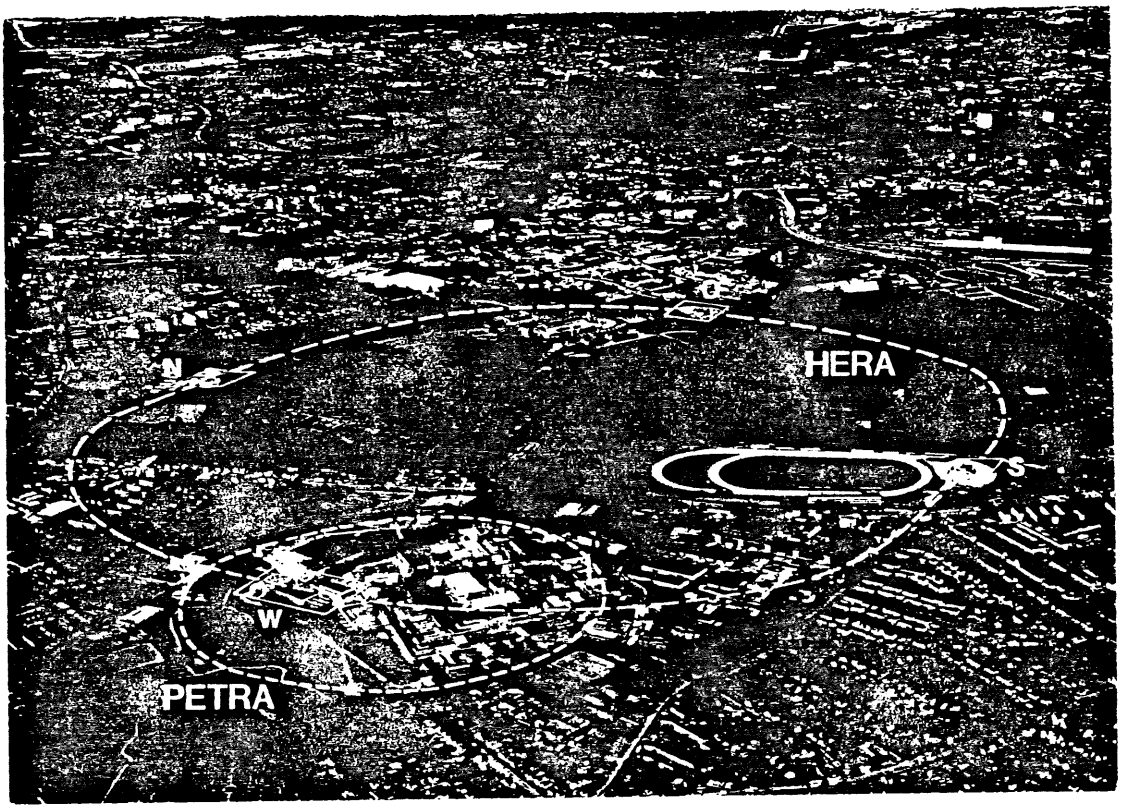

Figure 1.1.1 An aerial view of the DESY site, Hamburg, with the projected position of the HERA ring.

The accelerating rings are contained within a 6.3 km long tunnel which runs between 10 and 20 metres below ground, with a 1% incline to the horizontal. The rings were designed and constructed to provide four interaction points where the electron and proton beams collide head on, producing a maximum centre of mass energy of 314 GeV. Situated at the four interaction regions are multi-storey underground halls, where the large detectors are housed. The two projects at the moment

under construction, and nearing completion, are H1 and ZEUS, both having strong UK involvement. The Liverpool group is working on the H1 experiment, which is housed in the north hall at DESY (Figure 1.1.2).

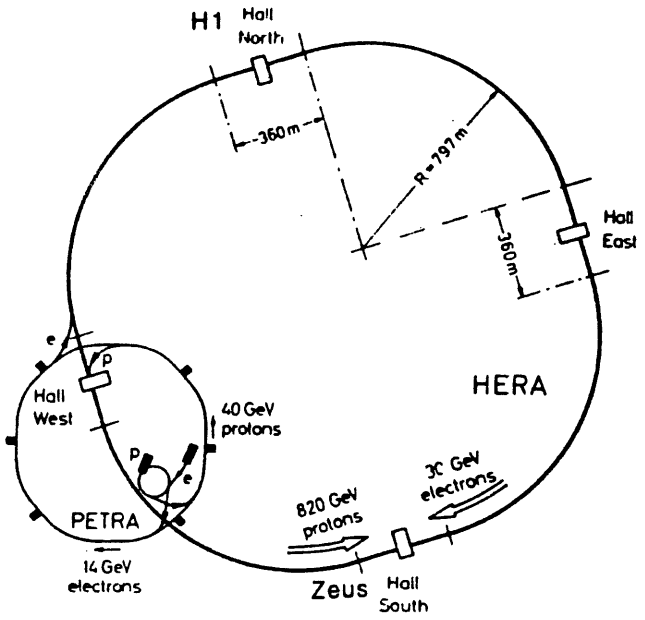

Figure 1.1.2 The HERA complex, DESY.

The purpose of HERA is to answer some of the mysteries that exist in our theories about the quark and lepton substructure of matter. The three generations of quarks and leptons are thought to be fundamental, though one quark, the so called 'top' quark, is so far undiscovered. HERA uses the elemental electron to probe deeper into the proton than ever before possible. It may be able to search for quark substructure, and may even be able to confirm the existence of the top quark, if its mass is small enough. The collision of the proton and electron can be viewed as a basic first order Feynman diagram (Figure 1.1.3).

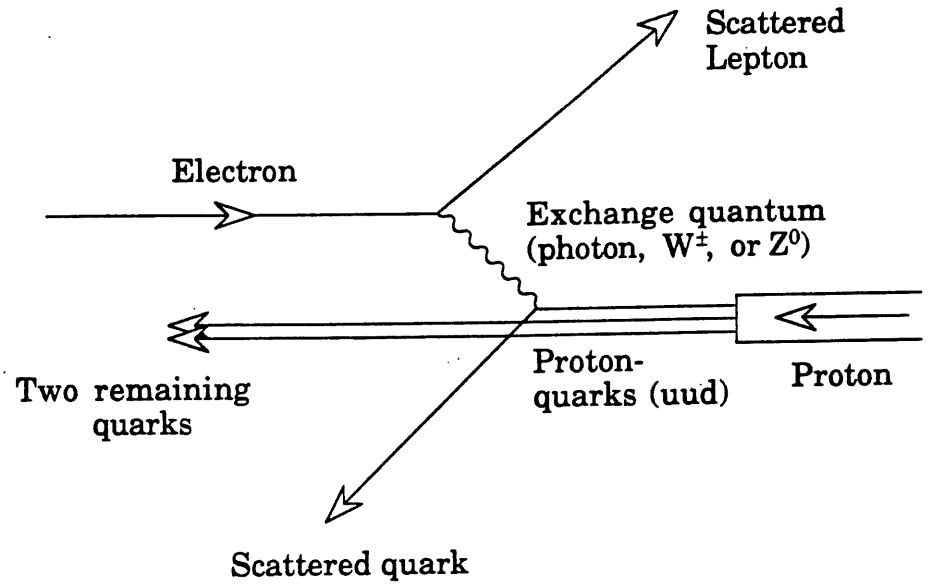

Figure 1.1.3 A basic first order Feynman diagram for the interaction of the proton and electron in HERA.

1.2 The H1 detector

The H1 detector layout is shown in Figure 1.2.1 (the 'x' marks the electron/proton interaction point). The fragments produced in any interaction will be boosted in the proton direction because the proton's energy exceeds that of the electron. This is why the detector is itself asymmetric in design. The general structure of the detector is as follows.

(1) Central and Forward Tracking detectors (CTD and FTD).

These are gaseous drift detectors for reconstructing charged particle tracks from the interaction region. The FTD will be discussed in Section 1.3.

Experiment H1

Vertical cut along the beam/
Längsschnitt in Strahlrichtung

Overall size: 12 x 10 x 15m
Abmessungen: 12 x 10 x 15m
Total weight: 2800 tons
Gesamtgewicht: 2800 Tonnen

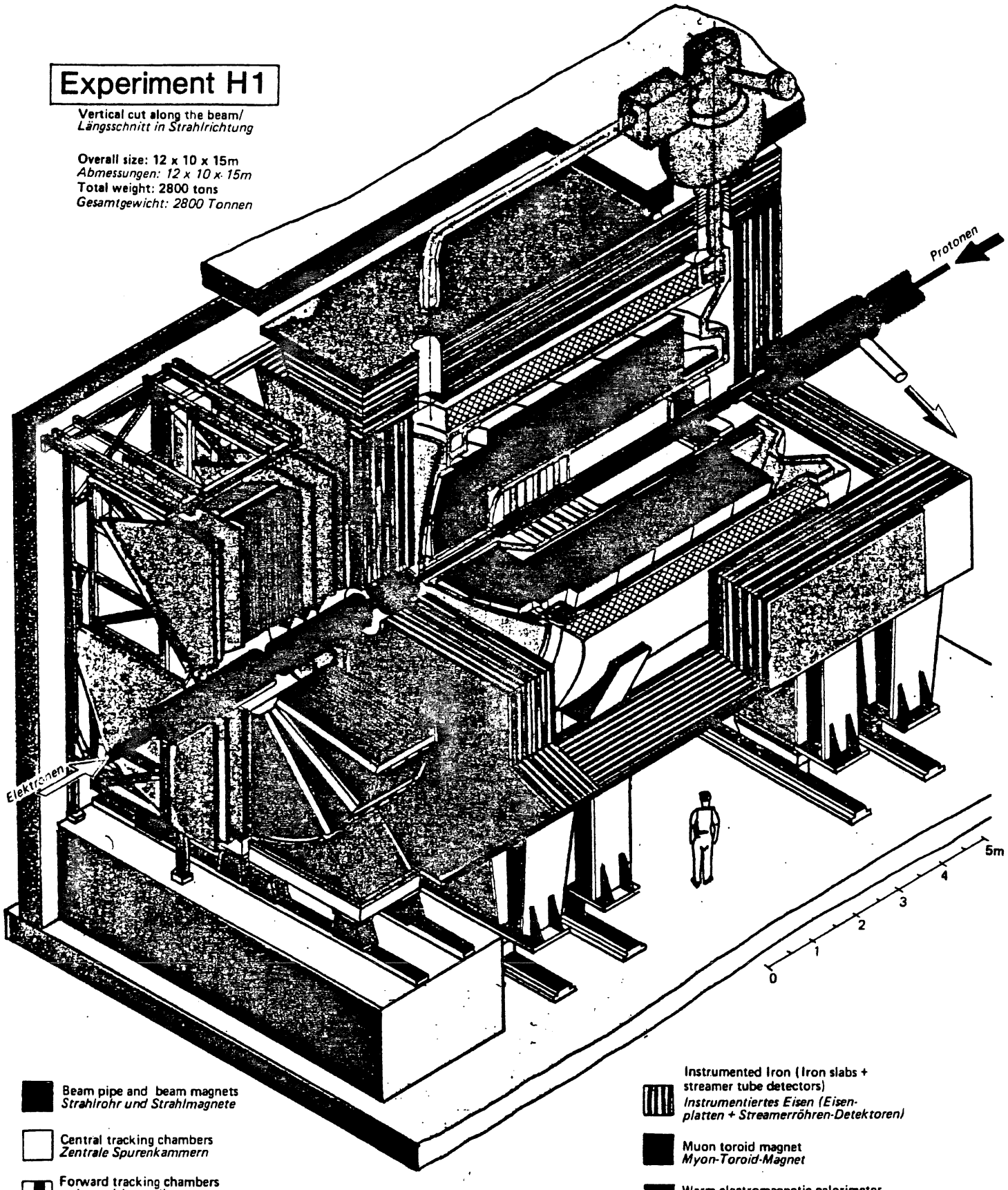

Beam pipe and beam magnets
Strahlrohr und Strahlmagnete

Central tracking chambers
Zentrale Spurenkammern

Forward tracking chambers and transition radiators
Vorwärtsspurenkammern und Übergangsstrahlungsmodul

Electromagnetic Calorimeter (lead)
Elektromagnetisches Kalorimeter (Blei)

Hadronic Calorimeter (stainless steel)
Hadronisches Kalorimeter (Edelstahl)

Liquid Argon
Flüssiges Argon

Superconducting coil (1.2 Tesla)
Supraleitende Spule (1,2 Tesla)

Compensating magnet
Kompensationsmagnet

Helium cryogenics
Helium Kälteanlage

Muon chambers
Myon-Kammern

Instrumented Iron (Iron slabs + streamer tube detectors)
Instrumentiertes Eisen (Eisenplatten + Streamerröhren-Detektoren)

Muon toroid magnet
Myon-Toroid-Magnet

Warm electromagnetic calorimeter
Warmes elektromagnetisches Kalorimeter

Plug calorimeter (Cu,Si)
Vorwärts-Kalorimeter

Concrete shielding
Betonabschirmung

Liquid Argon cryostat
Flüssig Argon Kryostat

(2) Liquid argon calorimeter.

This consists of two distinct parts:

(i) The electromagnetic (EM) calorimeter measures the deposited energy of the electrons and photons. It consists of lead plates in the forward and barrel regions, which act as the showering material, with liquid argon as the detector medium.

(ii) The hadronic calorimeter consists of stainless steel absorber plates, again with liquid argon as the detector medium, and measures the energy of the hadrons.

(3) Plug Calorimeter.

This is used to detect hadronic energy at small angles (>3°), and is composed of a copper/silicon sandwich.

(4) Superconducting coil.

This provides a magnetic field of 1.2 T, which is uniform to within 3% throughout the tracking detector region [1].

(5) Instrumented Iron plates.

These act as a return yoke for the magnetic field of the superconducting magnet, and as part of the 'tail catcher' to measure the remaining energy leaking out of the calorimeter. It has wire chambers to detect muon tracks, and streamer tubes in the laminations to act as 'tail catchers' for the remaining hadronic energy.

(6) Muon Chambers.

These are to provide muon detection in the forward and barrel regions of the detector. Additional muon spectrometery is located forward of the muon filter, and consists of four muon chambers and a magnetised iron toroid.

(7) Compensating Magnet.

This magnet compensates for the distortion of the proton and electron beams caused by the field of the superconducting solenoid.

(8) Backward EM Calorimeter (BEMC).

This has the same structure as the EM calorimeter except it is warm (i.e. no liquid argon). Its purpose is to detect the backward scattered electron in the collision.

(9) Time of Flight (TOF).

This provides information about the direction of particles detected in H1. Its primary purpose is to veto events with energy coming from upstream of the interaction region.

1.3 The H1 Forward Track Detector (FTD)

Due to the fragments being boosted in the proton direction, the FTD plays a major role in the detection of particles in the H1 experiment. Figure 1.3.1 shows the internal structure of the FTD. It covers the angles between 5° and 30° with respect to the interaction

point, and consists of three identical sections known as supermodules (Figure 1.3.2).

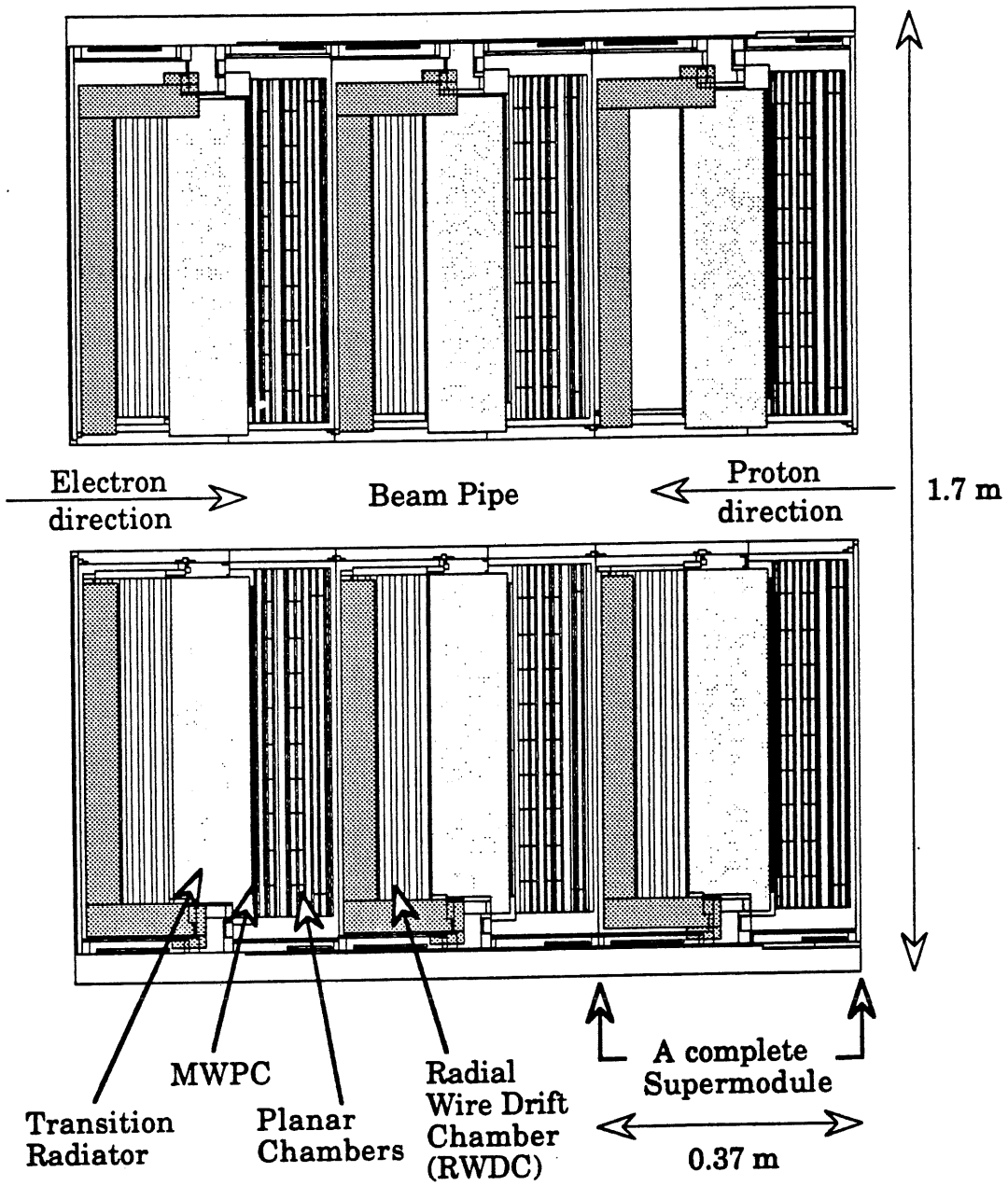

Figure 1.3.1 The side view of the H1 Forward Track Detector (FTD) showing the internal structure. The interaction point is about 2.5 m to the right of the FTD.

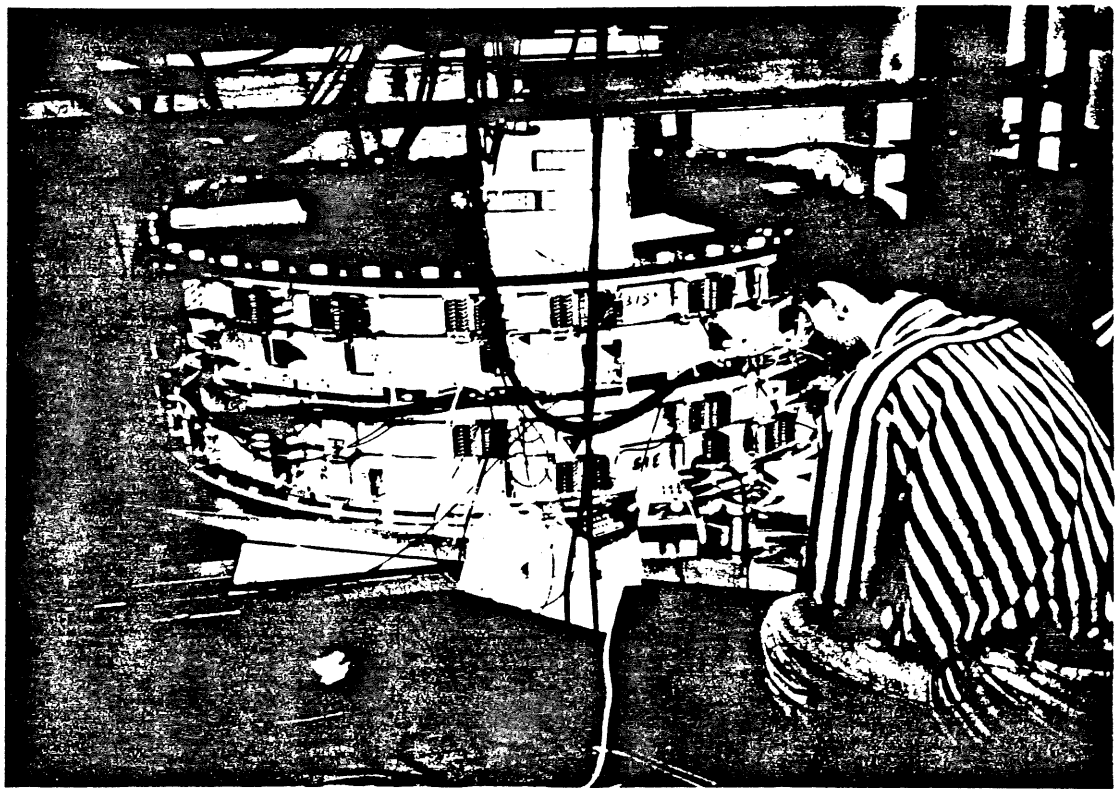

Figure 1.3.2 One of the supermodules being assembled at the Rutherford-Appleton Laboratory (RAL).

Each individual supermodule is composed of the following elements:

(1) Radial Wire Drift Chamber (RWDC).

This is a gaseous drift chamber with radial wire geometry. It gives good space point determination - the radial coordinate (to within 1-2 cm) by charge division, and the drift distance (to within 150 μm) from drift time measurement. Enhanced electron/hadron discrimination is achieved by good X-ray detection. Efficient dE/dx measurements (the average energy deposited per cm) is possible

because of proportional mode operation (Section 3.4). More detail will be given on the RWDC's in Chapter 2.

(2) Transition Radiator (TR).

This consists of 400 polypropylene foils, each 19 μm thick, spaced regularly within a thickness of 96 mm. A probability exists for particles to produce X-rays when they pass through the TR material, depending on their Lorenz γ (Energy /mass). The TR X-rays then enter the adjacent RWDC through a mylar window, which is directly upstream of the TR, and their energy deposition is measured to give enhanced electron/hadron discrimination.

(3) Multi Wire Proportional Chamber (MWPC).

The MWPC provides a fast trigger within the HERA bunch crossing time interval of 96 ns.

(4) Three layers of Planar drift chambers.

These are gaseous drift chambers with planar wire geometry. The chambers are oriented at 90°, 150°, and 30° in Φ. The RWDC's measure the radial coordinate to within an accuracy of 1-2 cm by charge division. The planar chambers can, however, improve this accuracy to 200 μm when the information from the three orientations is combined.

The planar chambers and MWPC's use an argon/propane gas mix, which was chosen for its good drift chamber performance and its capability of producing fast clean pulses. The TR's are filled with a

mixture of helium and ethane, an X-ray transparent gas mixture. The RWDC's, however, are designed such that they can detect X-rays, and so need an X-ray opaque gas mixture which also gives good spatial accuracy for track reconstruction. For this a xenon/helium/ethane mix has been chosen. It is quite clear, therefore, that each individual detector, within each supermodule, must be extremely gas tight to prevent any chance of the gas from one detector leaking into another, and thus destroying the carefully chosen conditions for operation.

Chapter 2

The Radial Wire Drift Chambers (RWDC's)

2.1 Introduction

The three RWDC's form an essential part of the H1 FTD. They were designed, constructed, and tested in the Department of Physics at the University of Liverpool. Three major design requirements were met.

(i) The materials used in the construction had to have low densities. This was to minimise the effects of multiple scattering and secondary interactions immediately before the main H1 calorimetry. The available space also had to be used as efficiently as possible.

(ii) They must give good space-point reconstruction, where the radial coordinate will be obtained from charge division along the length of the sense wire, and the drift distance by drift time measurement.

(iii) They must have efficient X-ray detection for electron/hadron discrimination.

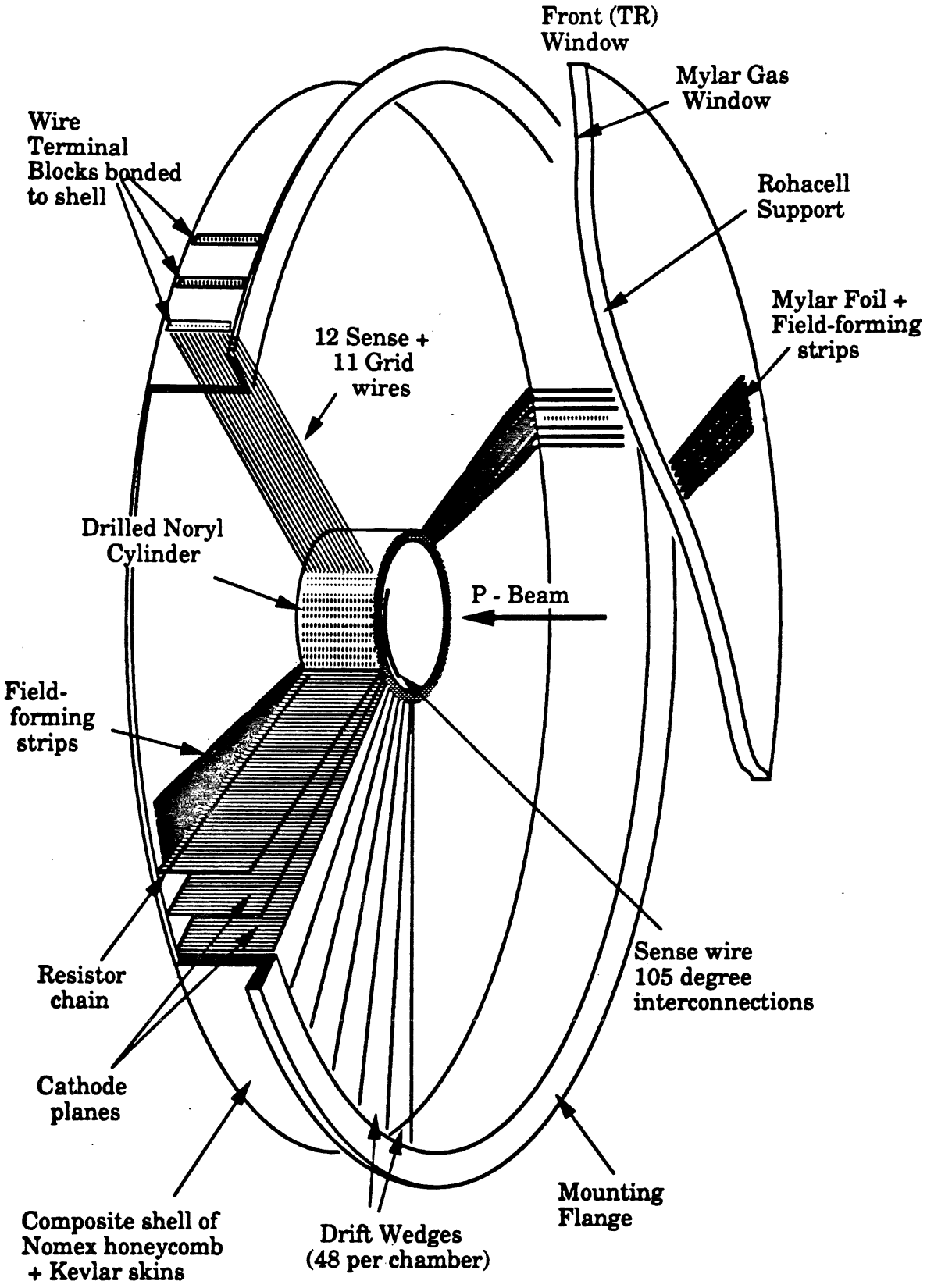

Figure 2.1.1 A diagrammatic view of the RWDC.

A number of test chambers, including a full-size prototype RWDC, were initially built for design checks and general testing. Three final RWDC's have been completed and have undergone numerous tests here and at RAL, where they were installed into their respective supermodules. A fourth RWDC is under construction at present, and will be used as a replacement if necessary. Figure 2.1.1 shows the geometry of the RWDC's.

The gas to be used in the RWDC's, when they are installed in the H1 detector, is a helium/xenon/ethane mix (40%, 30%, 30%, respectively) at atmospheric pressure. A small amount of isopropanol may be added to minimise deterioration of the sense wires. During testing, however, the RWDC's were filled with an argon/ethane mix (50%, 50%) as it is a well understood chamber gas, and cheap compared with xenon. The reasons for choosing these chamber gases will be discussed in Section 3.5.

2.2 The design and construction of the RWDC's

The basic structure of the RWDC's was based around a low mass, but rigid, main body made from Kevlar skinned Nomex honeycomb [2]. This material is widely used in aircraft construction, where extreme rigidity is required with the minimum weight used. The internal structure of the RWDC was designed to create precise electrostatics for efficient ionisation collection. We can summarise the components of the RWDC's as follows.

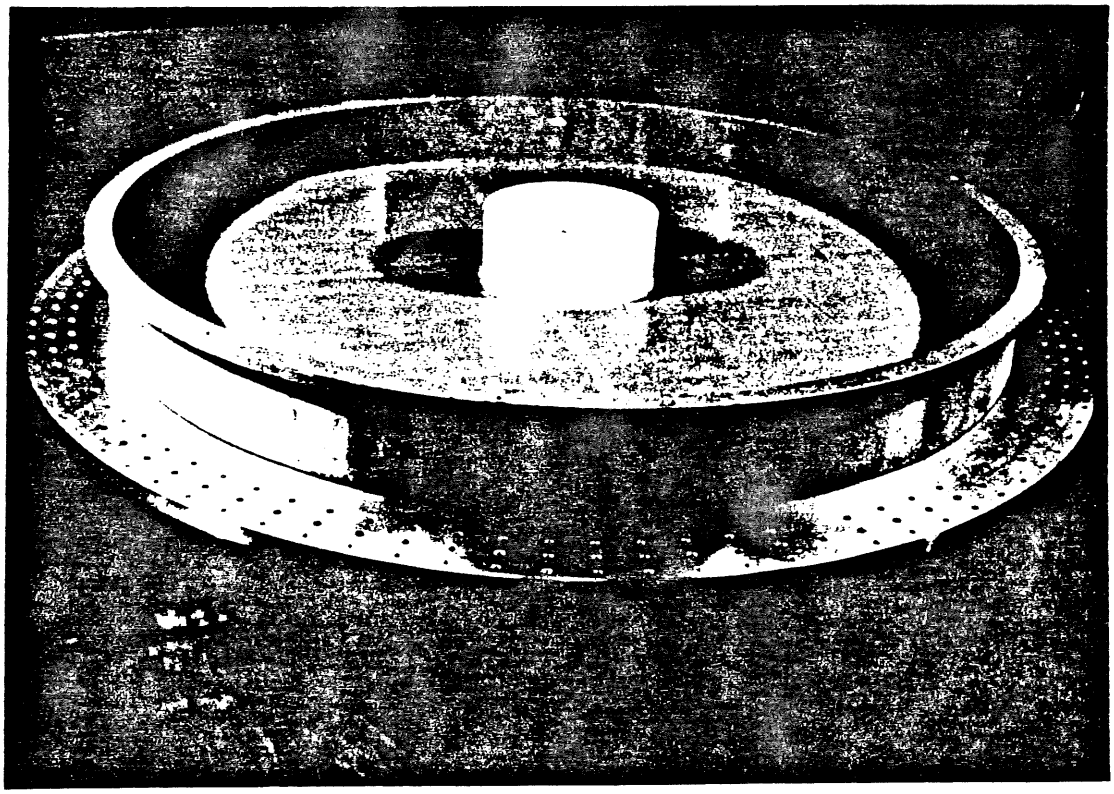

Figure 2.2.1 The Nomex honeycomb shell covered in Kevlar skins, with the central hub positioned. The shell is held horizontally on the jig plate.

(1) Main Body.

This is a dish shaped structure made from Nomex honeycomb with Kevlar skins. It was designed to support the highly tensioned sense and field wires which are strung radially from the central hub to the outer wall (Figure 2.2.1).

(2) Central Hub.

This is made from Noryl [3], a thermoplastic which can be accurately machined. The hub has precision drilled holes for the

sense and field wires, and slots to support the cathode planes (Figure 2.2.1).

(3) Back Field Formers.

The purpose of the back field formers is to maintain the drift field (Section 2.3) at the back and outer circumference of the RWDC's. They are made from 0.3 mm paper epoxy [4], with 2 mm wide copper strips (3 mm spacing) running parallel to the wire plane. They are bonded to the composite shell (Figure 2.2.2).

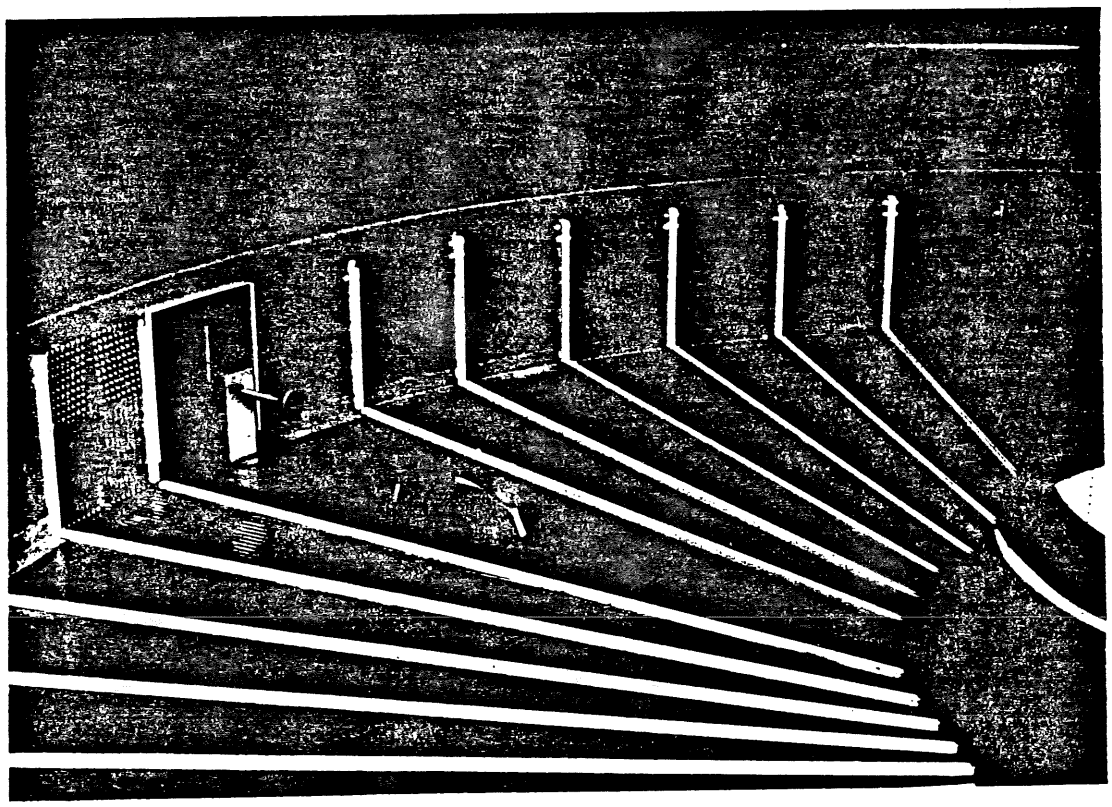

Figure 2.2.2 The back field formers being bonded to the composite shell. The Noryl locating strips are also positioned.

(4) Cathode planes.

These divide the RWDC into 48 wedge-shaped cells (7.5° in Φ), and are made from 0.6 mm thick paper-reinforced epoxy. The planes extend radially from the central hub and are segmented into 86 copper strips (6 mm wide, separated by 1 mm) on both sides. The strips are connected in series by surface-mount resistors (10 MΩ). They are located, and supported, at the back of the RWDC by slotted Noryl strips bonded to the shell (Figure 2.2.3).

Figure 2.2.3 The cathode planes being located in the shell. Note the Noryl strips for location.

(5) Sense wires.

These are made from Stablohm-800 [5], which is composed of 80% nickel, 19% chromium, and ~1% aluminium, with a diameter of 50 μm. Each wedge contains 12 sense wires strung radially out from the central hub to the outer wall. They are tensioned to 170 g.wt., and secured at both ends by crimped pins. The sense wires are spaced 1 cm apart along the beam direction, with a stagger of 285 μm about the mean wire plane to resolve the left-right track ambiguity (Figure 2.2.4). At the inner radius each sense wire is connected to its partner 105° away in Φ to ensure uniform distribution of mass. They are read out at the outer circumference (Section 4.5.1).

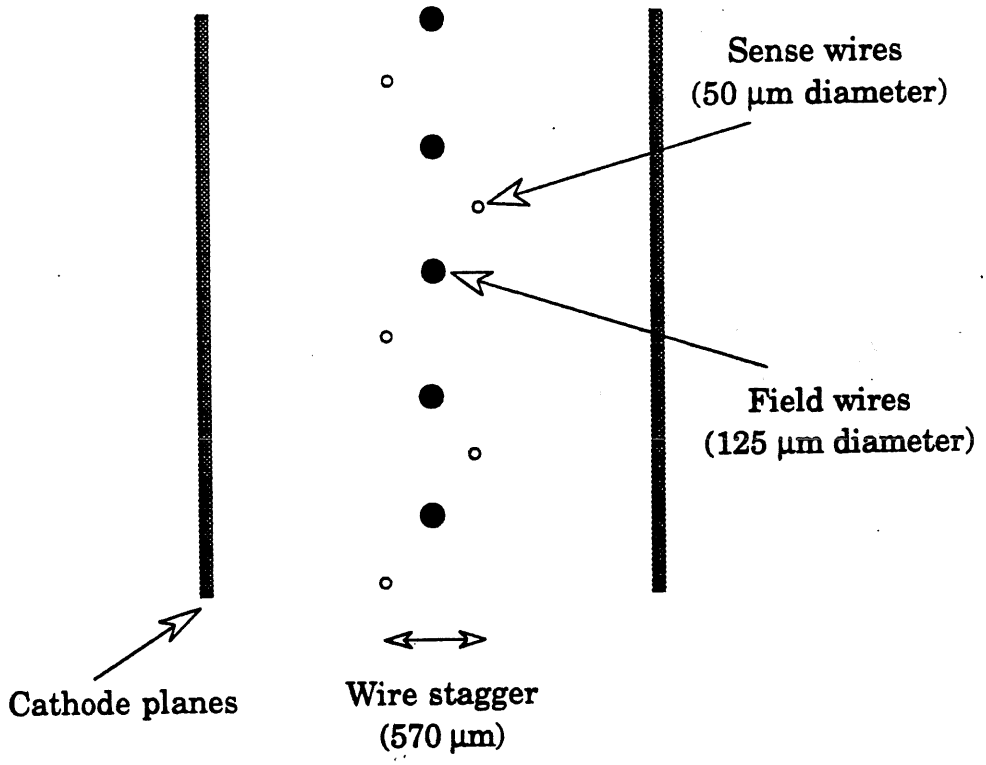

Figure 2.2.4 Looking down the wire plane of an RWDC wedge, showing the positions of the wires.

(6) Field wires.

These are also strung radially out from the hub alternately between the 12 sense wires, such that the outer two wires are sense wires (in total there are 11 field wires). They are made from a beryllium/copper alloy with a diameter of 125 μm, and are tensioned to 280 g.wt. They are electrically grounded.

(7) Gas tight window.

This produces a gas seal around the open face of the RWDC, whilst keeping the X-ray absorption to a minimum. It is made from 50 μm thick mylar, which is bonded to an inner ring of Noryl and an outer ring of resin-impregnated wood [4]. Slotted strips are bonded to the window to act as upstream locators for the cathode planes (Figure 2.2.5).

(8) Front field formers.

The electric field immediately in front of the window is maintained by field formers, held 5 mm upstream of the window (10 mm away from the first sense wire). They consist of 12 μm thick aluminium strip electrodes (2 mm wide, separated by 3 mm) mounted on a 25 μm thick polyester film [6], which is held away from the window by a 5 mm thick layer of rohacell foam [7]. The electrodes would produce regions near to the strips where deposited ionisation would not drift to the first sense wire if they were inside the RWDC, and so are stepped back outside the active region (Figure 2.2.5).

The signals along the sense wires are first amplified close to the RWDC by a differential input preamplifier [8](see Appendix A), and then recorded by 104 MHz 8-bit monolithic flash analogue-to-digital convertors (FADC's)[9].

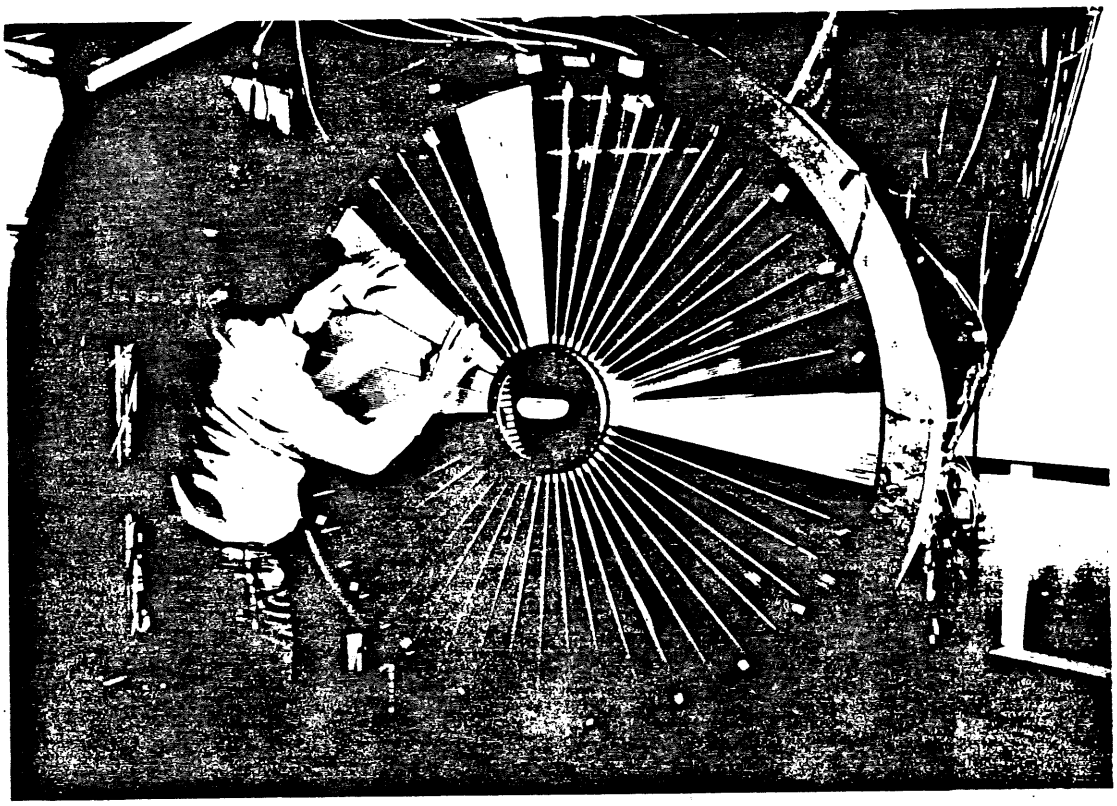

Figure 2.2.5 A completed RWDC with the front field formers being positioned on the mylar window.

The required precision needed for track reconstruction in the H1 experiment was met by the development of very precise construction techniques in the building of the RWDC's. Firstly, the Nomex shell was manufactured using a cold lay-up procedure on a precision

mould [10], and then laid horizontally on a jig plate. The supports for the wires were then positioned on the outer wall of the shell with feed-through holes drilled in the respective places. Following this the Noryl hub was positioned centrally in the shell (Figure 2.2.1), aligned with the outer wire supports. Noryl templates [11], with precisely drilled holes for the location of the wires, were lined up with the central hub and then bonded to the support frame. This was to ensure the true radial orientation of the wires. Once this stage was complete, the internal structure could be positioned and bonded (Figures 2.2.2 and 2.2.3). The RWDC was then ready for wiring. This was done with the RWDC held vertically on a wiring jig, such that the wires could be strung in the horizontal plane.

Tensioning the wires was achieved by hanging the correct weights on the ends of the wires, and then crimping the wires to pins in the hub and templates (Figure 2.2.6). An even distribution of force was maintained during wiring to avoid any warping of the RWDC. On completion, the tensions and resistances of all the wires were regularly noted. The gas window was then placed onto the front of the RWDC and bolted into position.

The RWDC's are supported in the gas tank of the FTD by the outer rim of the shell. This provides the gas seal, and allows the aligning of the RWDC's with respect to the other chambers in the FTD (Section 1.3).

Figure 2.2.6 The wires strung radially in each wedge, shown here at the central hub. Note the crimping pins, and the two types of wire used.

2.3 The electrostatics of the RWDC's

The electrostatics of the RWDC's were designed to ensure efficient ionisation collection at the sense wires. The basic geometry of a wedge shaped drift cell is shown in Figure 2.3.1.

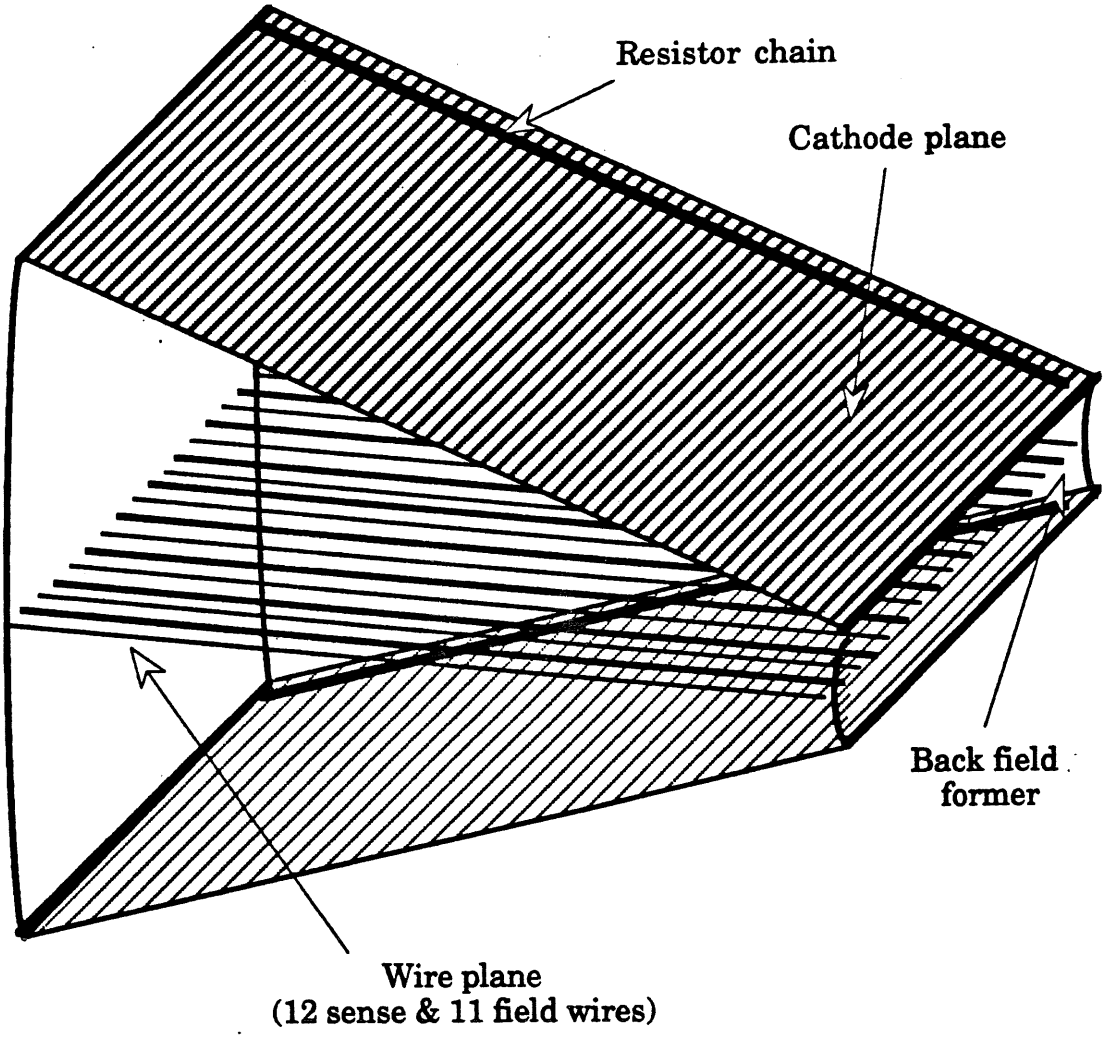

Figure 2.3.1 The basic geometry of a RWDC wedge.

We require a uniform drift field (E_{DRIFT}) that is perpendicular to the wire plane. The segmentation of the planes produces a cathode potential that is linearly dependent upon the radius, which creates an

E_{DRIFT} that is uniform and constant, even though the drift cell is wedge shaped. The drift field is maintained at the front, back, and outer radius of the RWDC's by field formers. The central electrode strips on each allow one to adjust finely the gas gain on the outermost sense wires. Gas gain will be discussed in detail in Section 3.3. The sense wires are held at a positive high voltage (HV) relative to the earthed field wires, to provide flexibility in the choice of both gas gain and E_{DRIFT} by permitting independent control of the strong electric field at the surface of the wire (the sense field, E_{SENSE}). A three dimensional sketch of the potential surface, that approximately exists within the RWDC wedge, is shown in Figure 2.3.2.

Beck [12] has established a set of simultaneous equations that define the electric fields inside the RWDC's. The equations involve only two field parameters, E_{DRIFT} and E_{SENSE}, and for the Ar {50%}/C_2H_6 {50%} gas mixture it is convenient to set E_{DRIFT} to 1.2 kV/cm. The equations now simplify into those given below [13](Equations 2.1 - 2.4). When a value of V_{SENSE}, the positive potential on the sense wire, is set, E_{SENSE} and the remaining voltages (cathode plane and field former) can then be evaluated. This sets up all the operating voltages needed for the correct electrostatics within the RWDC wedge.

Sense voltage (E_{DRIFT} = 1.2 kV/cm):

$$V_{SENSE} = AE_{SENSE} - BE_{DRIFT} \qquad \textbf{Equation 2.1}$$

Cathode plane outer voltage:

$$V_A = \alpha V_{SENSE} - (\beta + \varphi) E_{DRIFT} \qquad \textbf{Equation 2.2}$$

Cathode plane inner voltage:

$$V_B = \alpha V_{SENSE} - (\beta - \xi) E_{DRIFT} \qquad \textbf{Equation 2.3}$$

Back field former voltage:

$$V_C = \alpha V_{SENSE} - (\beta - \mu) E_{DRIFT} \qquad \textbf{Equation 2.4}$$

where A = 0.02194, B = 1.2511, α = 0.4478, β = 0.4702, φ = 4.872, ξ = 0.740, and μ = 0.440.

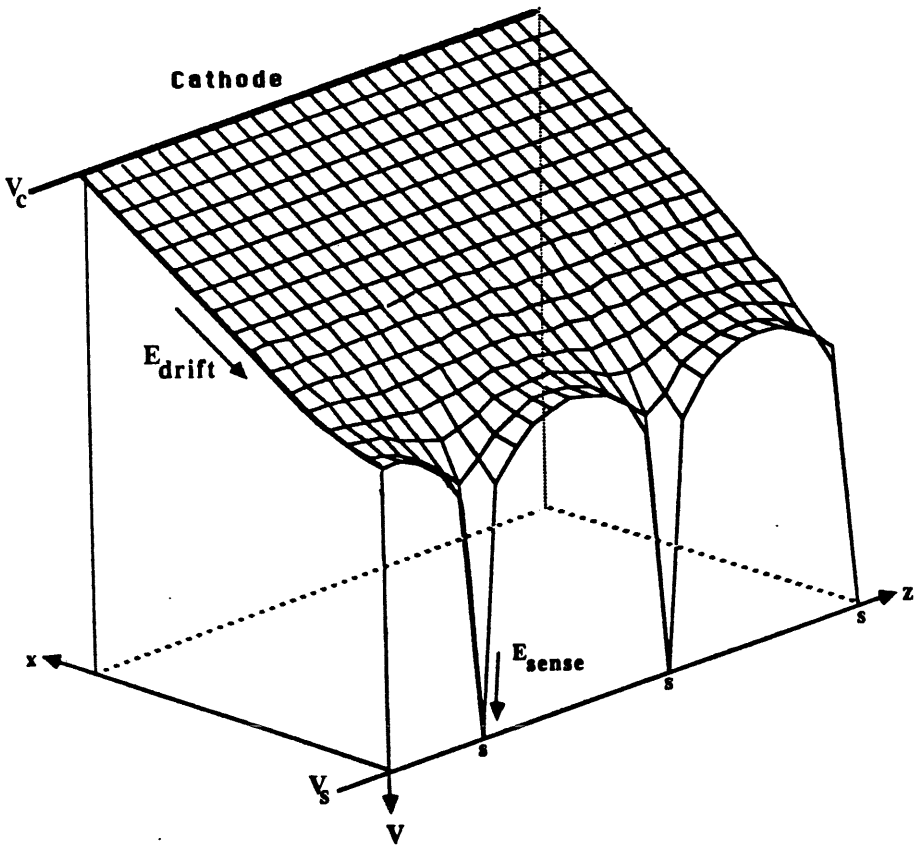

Figure 2.3.2 A three dimensional sketch of the sense and drift fields in the RWDC wedge (the sense wires are labelled **s**, V_S is the sense wire potential, and V_C is the cathode potential relative to the earthed field wires)

Figure 2.3.3 shows the basic structure of the fields produced in a drift cell. A dummy earth plane is included in the simulation to test the hypothesis that the front field forming strips close the electrostatic cage efficiently. The sense field is perfectly radial close up to the sense wire, with the drift fields being unaffected by the existence of the wires at distances of the order of a centimetre away. However, the sense wire stagger (which is not included in the simulation) produces a non-uniform surface field around each sense wire.

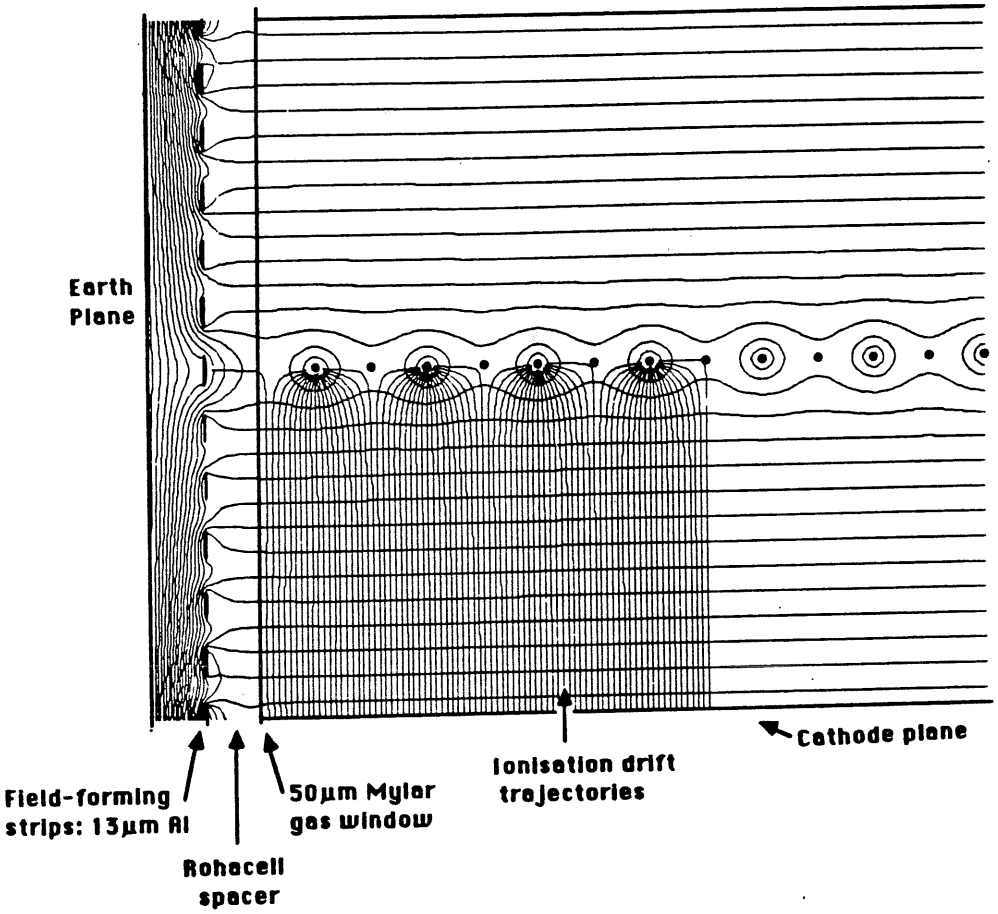

Figure 2.3.3 A simulation of the fields produced within a RWDC drift cell.

Chapter 3

Gas gain and proportional chambers

3.1 Introduction

It is essential to detect and locate the particles produced in a high energy physics experiment so that the energy and momentum transfer in a collision can be obtained. This allows us to work out interesting features that will help us in our understanding of the physics. The detection is often achieved by the collection of ionisation that may be left when a high energy particle, whether it is a photon, or a charged particle, interacts with gas atoms within a drift chamber. Both types of particle can liberate electrons by the electromagnetic interaction, but the obvious difference between them results in very different deposits being left.

When a photon, with an energy of the order of a few keV, interacts with a gas atom, it transfers its energy by exciting or ionising the atom. The dominant process by which the photon energy is absorbed is known as photo-electric absorption. In this process an atomic electron uses the incident photon energy to break free of the binding force of the atom. This produces an ion pair where the photo-electron carries away the remaining energy in the form of kinetic

energy, producing a delta-ray. But because of the large cross-section for inelastic electron-atom collisions, the delta-ray quickly dissipates its initial kinetic energy by ionising further atoms, and so produces a spatially localised packet of ionisation.

A relativistic charged particle will lose energy in a very similar way to the delta-ray, as described above. It will lose small fractions of its energy in multiple atomic collisions, many of which produce an ion pair. As the particle has such a high initial energy, the multiple collisions absorb only a small fraction of the incident energy, and so the particle will not come to rest in the gas. This produces a track of ionisation along its path, which is referred to as dE/dx deposition (Section 1.3).

So we find that a photon produces localised ionisation, and a charged particle produces a track of ionisation. The liberated electrons, in both cases, can be detected to give information on the high energy particle. We now go on to discuss the basic methods of detection.

3.2 The basic operation of a simple drift chamber

We must now ask how we can detect efficiently the electrons liberated by a high energy particle. This can be done by using a very simple cell which consists of two electrodes, a cathode and an anode, separated by a volume containing gas atoms. This gas must exhibit a high probability of producing ion pairs relative to the total cross section.

For the gas gain measurements Ar {50%} / C_2H_6 {50%} was used, the reasons for using this mixture are discussed in Section 3.5. We shall explain the following details with reference to this gas mixture.

Sauli [14] suggests that the optimum geometry for a simple drift chamber is a cylindrical coaxial arrangement, where the anode is a thin sense wire of radius **a**, strung centrally through a cylindrical cathode of internal radius **b** (Figure 3.2.1). If an X-ray, emitted from an Fe^{55} source (with an energy of 5.9 keV), enters this volume and ionises an argon atom by photo-ionisation, it is shown in Section 4.2 that on average a total of 230 ion pairs will be produced within the Ar {50%}/C_2H_6 {50%} gas mixture. If we collect the 230 electrons at the sense wire, a potential difference will be produced between the electrodes, which is given by Equation 3.1.

$$v = \frac{Q}{C} \qquad \textbf{Equation 3.1}$$

where:

v is the potential difference produced between the electrodes,

Q is the charge collected at the sense wire, and

C is the capacitance of the system.

The capacitance of such a system is approximately 10 pF, and Q is simply the charge of all 230 electrons (= 230 x 1.602 x 10^{-19} C = 3.7 x 10^{-17} C). The potential difference, v, is therefore 3.7 μV, which is far too small for any possible detection. We therefore require a process that will amplify the initial ionisation signal to a level that may be detected.

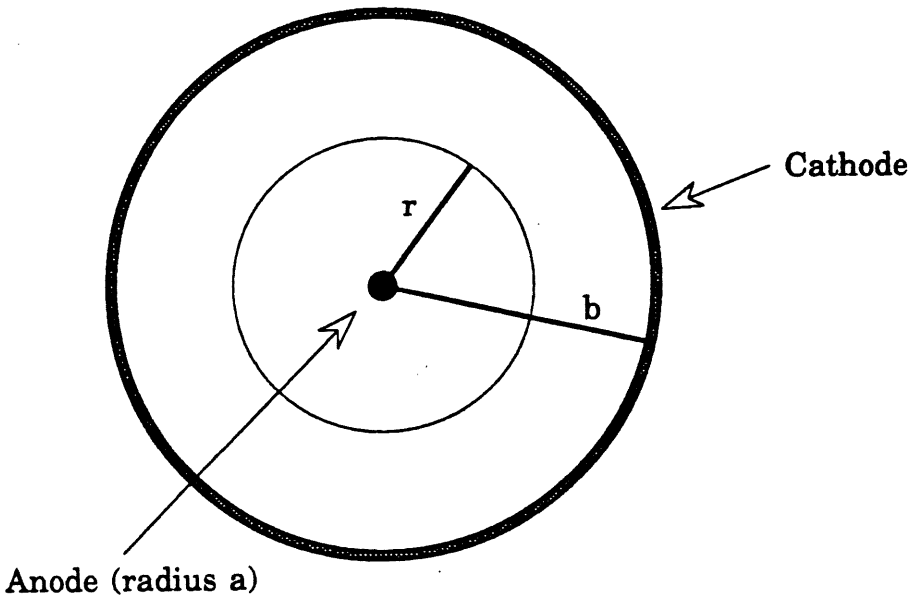

Figure 3.2.1 The optimum geometry for a single wire drift chamber (cross-section).

If we apply a potential difference, V, across the electrodes, such that the sense wire is positive with respect to the electrically grounded cathode, a uniform radial electric field can be produced that attracts the electrons to the sense wire. The electric field in the cylindrical system can be written as a function of the radial distance, **r** (Equation 3.2), using Gauss' Theorem,

$$E(r) = \frac{V}{\ln(b/a)\, r} \qquad \textbf{Equation 3.2}$$

where $r > a$. Equation 3.2 leads to Equation 3.3.

$$E_{SENSE} = E(a) \qquad \textbf{Equation 3.3}$$

This arrangement produces a very intense electric field at the surface of the sense wire (E_{SENSE} ~ 170 kV/cm), in comparison with the fields nearer the cathode (~ 1 kV/cm) which are suitable for drift chamber operation.

3.3 Gas gain

The field in the majority of the chamber acts as a drift field for both electrons and ions, drifting the electrons to the sense wire and the ions to the cathode. However, within 50 μm of the sense wire surface [14], the sense field is strong enough to initiate avalanche multiplication. This is where the drifting electrons gain enough energy from the strong electric field to ionise further argon atoms, resulting in an electron avalanche. The avalanche provides a gain in signal (commonly referred to as 'gas gain') which enables the signal to be measured.

For every electron that approaches the sense wire, the gas gain will produce G electrons, where G is the gas gain multiplication factor. G will clearly increase with V. This is because, at higher values of V, the acceleration of the electrons between atomic collisions is greater due to the greater value of E_{SENSE}. This allows the electron to gain more energy between collisions, and so increases the probability of subsequent ionisations occurring. The gas gain is seen to depend exponentially upon E_{SENSE}, and can be generalised by Equation 3.4 [15].

$$\frac{G_2(E_2)}{G_1(E_1)} = \exp\left[k\,(E_2 - E_1)\right] \qquad \textbf{Equation 3.4}$$

where: G_2 is the gas gain at sense field E_2,

G_1 is the gas gain at sense field E_1, and

k is a constant.

This is only true whilst the drift chamber is operating in the proportional mode (Section 3.4). From Equation 3.4 it is easy to see that:

$$k = \frac{d(\ln G)}{d(E_{SENSE})} \qquad \textbf{Equation 3.5}$$

which is simply the gradient of the graph of ln(G) verses E_{SENSE}. In Chapter 4 we discuss how we obtain the data for this graph using various proportional drift chambers, and in Chapter 5 we compare our results to those of Hessing and Kadel [16] and Salmon [17].

G is well known to be dependent upon the pressure p, and temperature T of the chamber gas [14]. The approximate relationship is given by Equation 3.6.

$$G = f(E_{SENSE}, p, T) = f\left(\frac{E_{SENSE}\,T}{p}\right) \qquad \textbf{Equation 3.6}$$

This general relationship was observed during the irradiation exposure study discussed in Chapter 7.

With reference to Figure 3.3.1 we can summarise the development of the avalanche as follows.

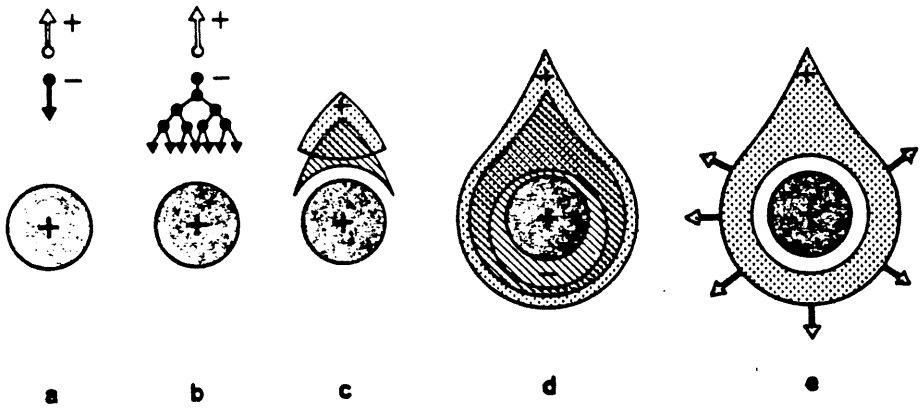

Figure 3.3.1 The time development of an avalanche in a proportional drift chamber at the sense wire [14].

(a) A single gas atom is ionised and creates a single electron and positively charged ion. The electron drifts towards the sense wire whilst the ion slowly drifts towards the cathode. The electron has a larger drift velocity than the ion due to its much smaller mass.

(b) The single electron gains enough energy from the increasingly high electric fields to liberate further electrons, which then go onto liberate more, resulting in an avalanche.

(c) The avalanche produces a cloud of ions which slowly migrates to the cathode. The lateral diffusion of the electrons produces a drop-like avalanche which begins to surround the wire. The electrons continue to avalanche.

(d) The avalanche of electrons then completely surrounds the wire.

(e) All the electrons are collected at the sense wire within 1 ns of the initial ionisation, while the cloud of ions is still slowly migrating to the cathode.

(f) The ions continue to drift slowly to the cathode; they are all collected within about 1 ms [18](see Appendix B).

3.4 The proportional mode of operation

As the potential difference, V, between the sense wire and cathode is increased, the conditions in the chamber will vary accordingly. Figure 3.4.1 shows how the chamber response varies with the applied potential difference between the electrodes.

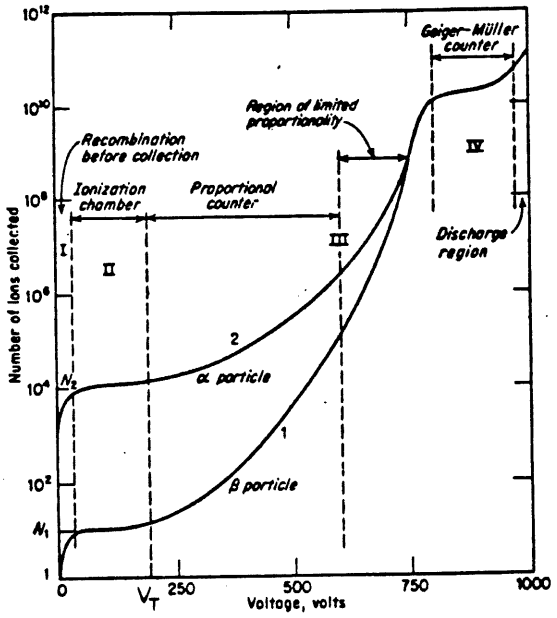

Figure 3.4.1 A schematic representation, showing the relationship between the gas gained signal and the potential difference applied between the two electrodes of the simple drift chamber [14].

At low voltages, the liberated electrons begin to be collected at the sense wire, but recombination of the ions and electrons before collection is the dominant process. As the voltage is increased, so does the drift and sense fields, which allows the full collection of ionisation but without significant gain. However, above a certain voltage, known as the threshold voltage V_T, the sense field becomes large enough to start the process of gas gain. In this region the chamber is said to be operating in the proportional mode, where the detected signal is related to the initial ionisation signal by a multiplication factor, G, which increases with potential difference. Gas gains in excess of $G = 10^4$ can

be achieved in this region. Unfortunately this proportional response breaks down at much higher voltages due to distortions in the fields caused by space-charge build up around the sense wire. The chamber at this point is said to be in the Geiger-Muller mode. We shall operate the RWDC's in the proportional mode with adequate gain for the sensitivity of the read-out electronics, and such that we can relate the detected signal to the initial ionisation signal by the factor G.

3.5 The choice of chamber gas

All gases are capable of producing gas gain. However, the experimental requirements for the operation of a proportional drift chamber restricts the choice to only a few groups. Noble gases are by far the best main component of a gas fill, as the atoms have a symmetrical electronic configuration. They allow reasonable gains ($G = 10^3 - 10^4$) to be achieved at much lower fields than for complex molecules. The choice of which noble gas to be used depends upon the specific detection requirements and the cost. The RWDC's in the H1 experiment will be operated with a Xe {30%}/He {40%}/C_2H_6 {30%} gas mixture, although Ar {50%}/ C_2H_6 {50%} was used in the tests that were completed at Liverpool.

A chamber that is operated with just pure argon suffers from the fact that it does not allow gains in excess of $G = 10^4$ to exist without entering a permanent discharge mode. This is because argon can only return to the ground state, after excitation, by a radiative process. The

emitted photons have a minimum energy of 11.6 eV, which is well above the ionisation energy of copper (7.7 eV), of which the cathodes of the drift chambers used in the experiments to determine G were composed. These photons can therefore liberate electrons from the cathode, and so produce an avalanche soon after the main signal. A quencher is therefore required to absorb this photon energy in such a way that no extra electrons are liberated. Polyatomic molecules, particularly organic compounds, can absorb the photons and use the energy to vibrate or rotate the molecules, or even dissociate them into simpler radicals. With small amounts of organic gas added to the noble gas filling, the operation of the drift chamber changes dramatically. The good absorption qualities of the quencher in the energy range of the photons emitted by argon, and the subsequent suppression of the secondary emissions, allows gas gains of the order of $G = 10^6$ to be obtained without discharge. For these reasons ethane is added to the RWDC gas mixture.

Chapter 4

The methods and equipment used to determine gas gain

4.1 Introduction

In this chapter we discuss the methods and equipment used in determining the gas gain in a proportional drift chamber as a function of E_{SENSE}. The results were taken firstly using a single wire drift chamber (SWDC), and secondly with the prototype radial wire drift chamber (RWDC) and a production RWDC.

Gas gain is simply the process of amplifying an initial ionisation signal whilst the drift chamber is operating in the proportional mode. Let us assume the initial ionisation, caused by a high energy particle, produces a number of ion pairs N_{ip}, the ions and free electrons of which are attracted to their respective electrodes (as described in Section 3.3). The number of free electrons that are initially produced, N_e, have a total charge $Q_{INITIAL}$. Avalanching of the electrons increases this charge to $Q_{COLLECTED}$ near the surface of the sense wire. The gas gain multiplication factor, G, is given in terms of $Q_{INITIAL}$ and $Q_{COLLECTED}$ by Equation 4.1.

$$G = \frac{Q_{COLLECTED}}{Q_{INITIAL}} = \frac{Q_{COLLECTED} / \Delta t}{Q_{INITIAL} / \Delta t} = \frac{I_{COLLECTED}}{I_{INITIAL}} \qquad \textbf{Equation 4.1}$$

where Δt is a period of time common to both $Q_{COLLECTED}$ and $Q_{INITIAL}$. We hence have to determine the following parameters to find G as a function of E_{SENSE}.

(i) Initial signal -
$Q_{INITIAL}$ - the charge produced in the initial ionisation, or
$I_{INITIAL}$ - the current due to the flow of $Q_{INITIAL}$

(ii) Collected signal -
$Q_{COLLECTED}$ - the charge collected at the sense wire after gas gain, or
$I_{COLLECTED}$ - the current due to the flow of $Q_{COLLECTED}$

(iii) Sense field -
E_{SENSE} - the electric field at the surface of the sense wire

We now go on to discuss how the above parameters were measured and used to determine G as a function of E_{SENSE}.

4.2 The determination of the initial number of electrons, N_e

A charged particle produces a random number of ion pairs along its track, resulting in a Landau distribution [19] of the number of ion pairs for a large number of incident particles (Figure 7.1). Incident X-rays produce a Gaussian distribution when they ionise (Figure 4.5.6).

Sauli [14] gives values for the energy required to produce single ion pairs in various gases (Table 4.2.1). However, he warns that "the values of W_{ip} correspond just to a reasonable average over results of

different experimenters, and the values can differ up to as much as 20-30% from the average". With the knowledge of W_{ip}, and the energy of the incident X-ray, E_X, one can evaluate the number of ion pairs, N_{ip}, produced per X-ray event (Equation 4.2).

$$N_{ip} = \frac{E_x}{W_{ip}} \qquad \textbf{Equation 4.2}$$

Gas	W_{ip} (eV)
Ar	26
CH_4	28
C_4H_{10}	23

Table 4.2.1 The relevant values of W_{ip} [14].

Sauli states, that for a gas mixture, W_{ip} can be evaluated by a simple composition law (Equation 4.3).

$$W_{ip}^{MIX} = [(W_{ip}^{A})x] + [(W_{ip}^{B})y] \qquad \textbf{Equation 4.3}$$

where gases **A** and **B** are mixed in the proportions **x** and **y** respectively, W_{ip}^{A} being the value of W_{ip} for gas **A**, and W_{ip}^{B} for gas **B**. This allows us to work out W_{ip} for argon/methane (50%/50%), and argon/iso-butane (50%/50%), using Equation 4.3 and the values given in Table 4.2.1.

$$W_{ip} (Ar\ \{50\%\}/CH_4\ \{50\%\}) = 27\ eV$$
$$W_{ip} (Ar\ \{50\%\}/C_4H_{10}\ \{50\%\}) = 25\ eV$$

These give the following values for N_{ip} with an Fe^{55} X-ray source, using Equation 4.2 (E_X for an Fe^{55} X-ray is 5.9 keV).

$$N_{ip} (Ar\ \{50\%\}/CH_4\ \{50\%\}) = 219$$
$$N_{ip} (Ar\ \{50\%\}/C_4H_{10}\ \{50\%\}) = 241$$

We shall take the value of N_{ip} for Ar {50%}/C_2H_6 {50%} to be the mean of N_{ip} (Ar {50%}/CH_4 {50%}) and N_{ip} (Ar {50%}/C_4H_{10} {50%}), and include a systematic error taken to be the difference between them. Therefore:

$$N_{ip} \text{ (Ar \{50\%\}/}C_2H_6 \text{ \{50\%\})} = 230 \pm 11$$

This is the mean number of ion pairs produced per Fe^{55} X-ray interaction with an argon atom in the Ar {50%} / C_2H_6 {50%} mix. It is simply the number of free electrons, N_e, and ions, N_i, produced before drifting to the anode and cathode commences.

4.3 The proportional drift chambers

Various proportional drift chambers were used to determine the gas gain factor, G, at different values of E_{SENSE}. We now go on to discuss these chambers.

4.3.1 The radial wire drift chambers (RWDC's)

Stable operation of the RWDC's depends upon the magnitude of the gas gain at the sense wires. With very high gains, the lifetime of the sense wires is greatly reduced, and so it is necessary to know how G varies with E_{SENSE}. The RWDC's were operated with the Ar {50%}/C_2H_6 {50%} chamber gas during the tests.

The RWDC's are wired in such a way that the sense wires of two separate wedges, 105° apart in Φ, are connected together at the central hub, producing a "wedge pair". Therefore only one "wedge pair" need be connected to the data acquisition electronics (which will be discussed

in detail in Section 4.5.1), and the computer controlled CAEN high voltage (HV) supply, to create a fully operational unit. Figure 4.3.1 shows where the Fe^{55} X-ray source was held in front of the operational "wedge pair" of (a) the prototype RWDC, and (b) the production RWDC, during the gas gain experiments. The source was positioned using a magnetic arm attached to the test rig (Figure 2.2.5). Only one of the 12 sense wires in the "wedge pair" was read-out by the electronics during the experiment.

The central hub connection made it possible for charge division measurements to be calculated along the complete length of the "wedge pair", and from this we could reconstruct the radial distance of the event along the sense wire. The data acquisition system allowed us to analyse the left and right channels from the left and right ends of the single sense wire separately (Section 4.5.1). With the prototype RWDC (Figure 4.3.1a), the X-ray events occurred within the left wedge of the "wedge pair", and so the charge division would result in more charge to flow through the left channel than the right. The source was in fact positioned half way along the active region of the left wedge, and so we would expect the left channel pulses to be about three times larger than the right at the ends of the sense wire. However, this factor is modified to about two due to the input impedances of the H1 preamplifiers [8] (see Appendix A). This can be seen in Figure 4.3.2, which is a non-linear digitised picture of an actual X-ray pulse from the prototype RWDC, showing the left and right components separately.

In the case of the production RWDC (Figure 4.3.1b), the source was held at the same radial distance, but in front of the right wedge.

We would therefore expect the opposite to be true; the right channel pulse to be about twice as large as the left. This can be seen in Figure 4.3.3.

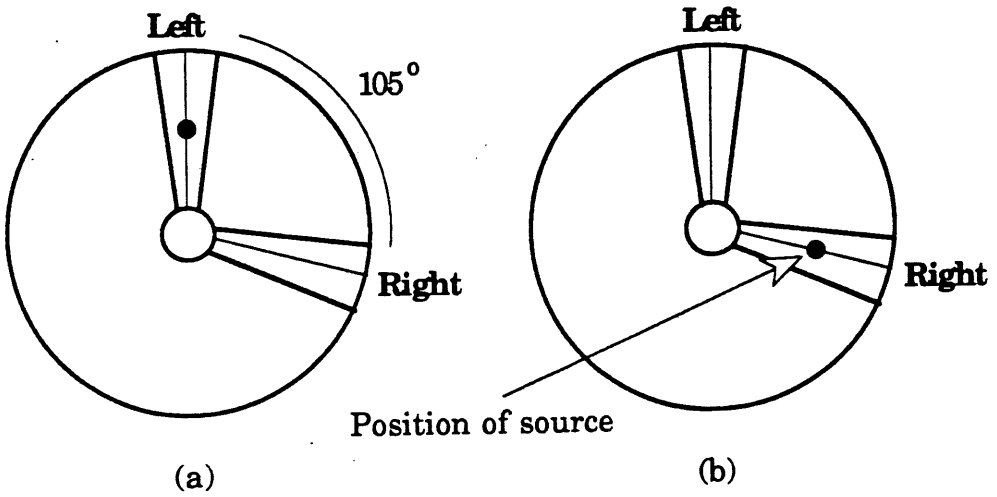

Figure 4.3.1 The position of the Fe^{55} X-ray source during the tests on (a) the prototype, and (b) the production RWDC. The operational "wedge pair" in each case, is shown with the left/right channel orientation.

In both Figures 4.3.2 and 4.3.3, the very sharp rising edge, characteristic of X-rays, can be seen. The localisation of the ionisation from an X-ray event produces a cloud of electrons with very similar drift times, and therefore they arrive at the sense wire and undergo gas gain within a few nano-seconds (ns). The charge on the sense wire then decays exponentially, and produces a long tail, which is caused by the resistive-capacitive (RC) properties of the chamber and the read-out electronics (Section 4.5.1).

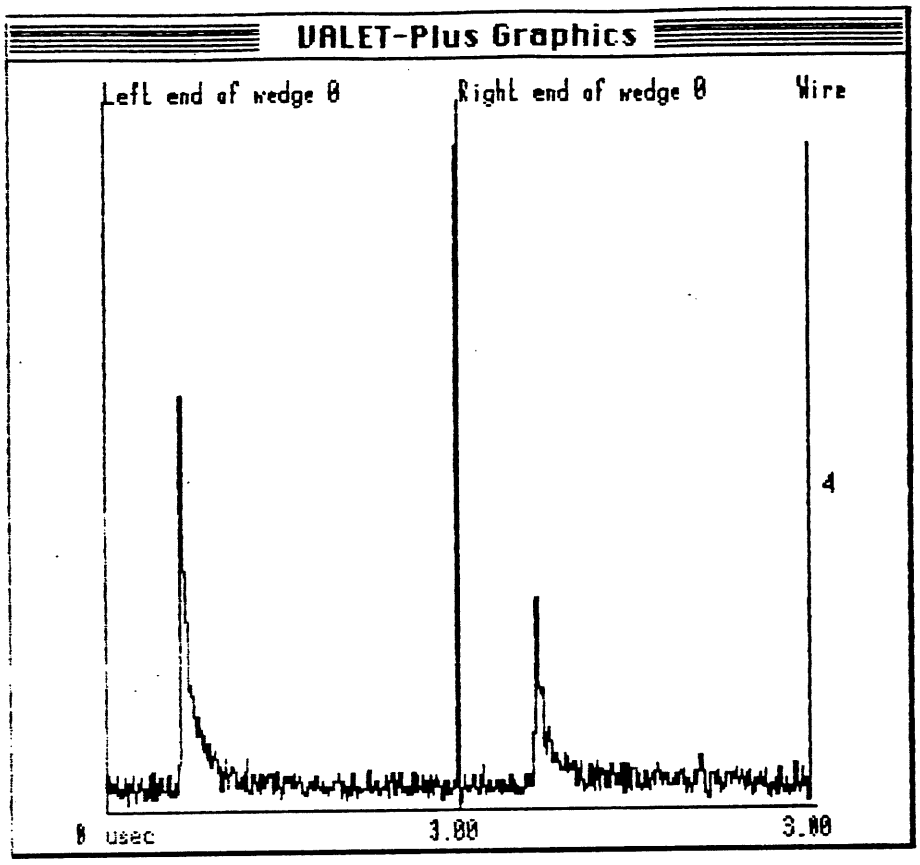

Figure 4.3.2 A non-linear digitised Fe^{55} X-ray pulse from the prototype RWDC, showing the left and right components of the pulse. This particular event was recorded with a sense field of 174 kV/cm.

The set of simultaneous equations that were used to determine E_{SENSE} [13] were for a gas mixture of Ar {50%}/C_2H_6 {50%}, and an E_{DRIFT} of 1.2 kV/cm. Certain restrictions on E_{SENSE}, nevertheless, had to be adhered to for safe and practical operation. The upper limit of E_{SENSE} for the RWDC's was set at 175 kV/cm, and was established to protect the RWDC's from being permanently damaged by the effects of the very high gains at the higher values of E_{SENSE}. The lower limit was determined by the signal to noise ratio, and it was found that below 160 kV/cm the

pulses were hidden by noise, most likely attributable to a strong nearby r.f. source.

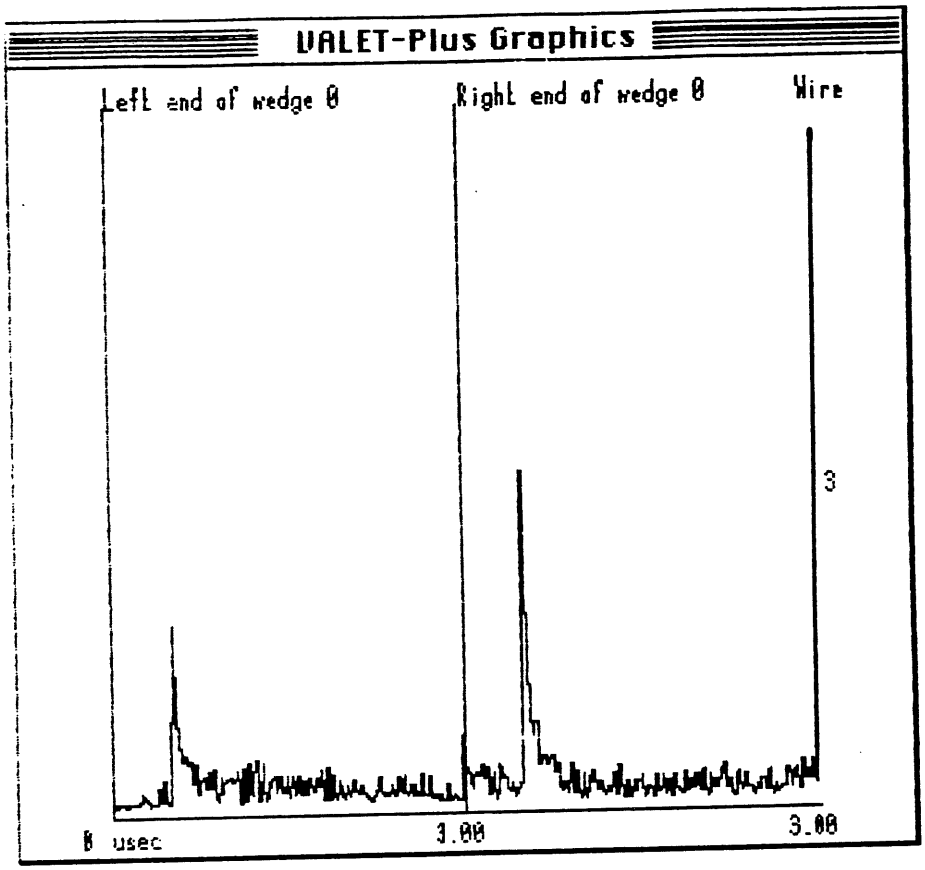

Figure 4.3.3 A non-linear digitised Fe^{55} X-ray pulse from the production RWDC, showing the left and right components of the pulse. This particular event was recorded with a sense field of 166 kV/cm.

4.3.2 The single wire drift chamber (SWDC)

This chamber was designed to reconstruct the electrostatics of the RWDC around the sense wire, but with a much simpler method for determining E_{SENSE}. In Section 3.2 we discussed the determination of

E_{SENSE} in a cylindrical chamber with a coaxial sense wire, this being the optimum geometry for a simple proportional drift chamber as suggested by Sauli. The SWDC was based upon this very simple geometry (Figure 4.3.4).

The SWDC consisted of a Stablohm-800 [5] sense wire, with radius $a = 24.7 \pm 0.3$ μm, strung coaxially through a 31 cm long copper cathode, with an internal radius of $b = 13.16 \pm 0.04$ mm. The sense wire was tensioned to 170 g.wt., like the sense wires in the RWDC. An aluminium window, positioned centrally in the cathode wall of the SWDC, allowed the entry of the Fe^{55} X-rays into the active volume which was filled with the Ar {50%}/C_2H_6 {50%} gas mix. The SWDC was sealed with Noryl end caps, and gas flow pipes at each end allowed the continuous flow of the chamber gas.

Both ends of the sense wire were connected to the data acquisition system, as with the RWDC, and a positive HV (V_{SENSE}) was applied to the wire with a computer controlled CAEN HV supply. Using Equation 3.3, E_{SENSE} could be evaluated.

Restrictions also existed on the values of E_{SENSE} that could be used with the SWDC. The data acquisition system was unable to register pulses that were produced in the SWDC with $E_{SENSE} > 190.3$ kV/cm ($V_{SENSE} > 2.95$ kV), as they were too large for the dynamic range of the electronics. This determined the upper limit. The lower limit was again ascertained by the signal to noise ratio at the lower values of

E_{SENSE}, and with E_{SENSE} < 164.5 kV/cm (V_{SENSE} < 2.55 kV), the pulses were obscured by noise.

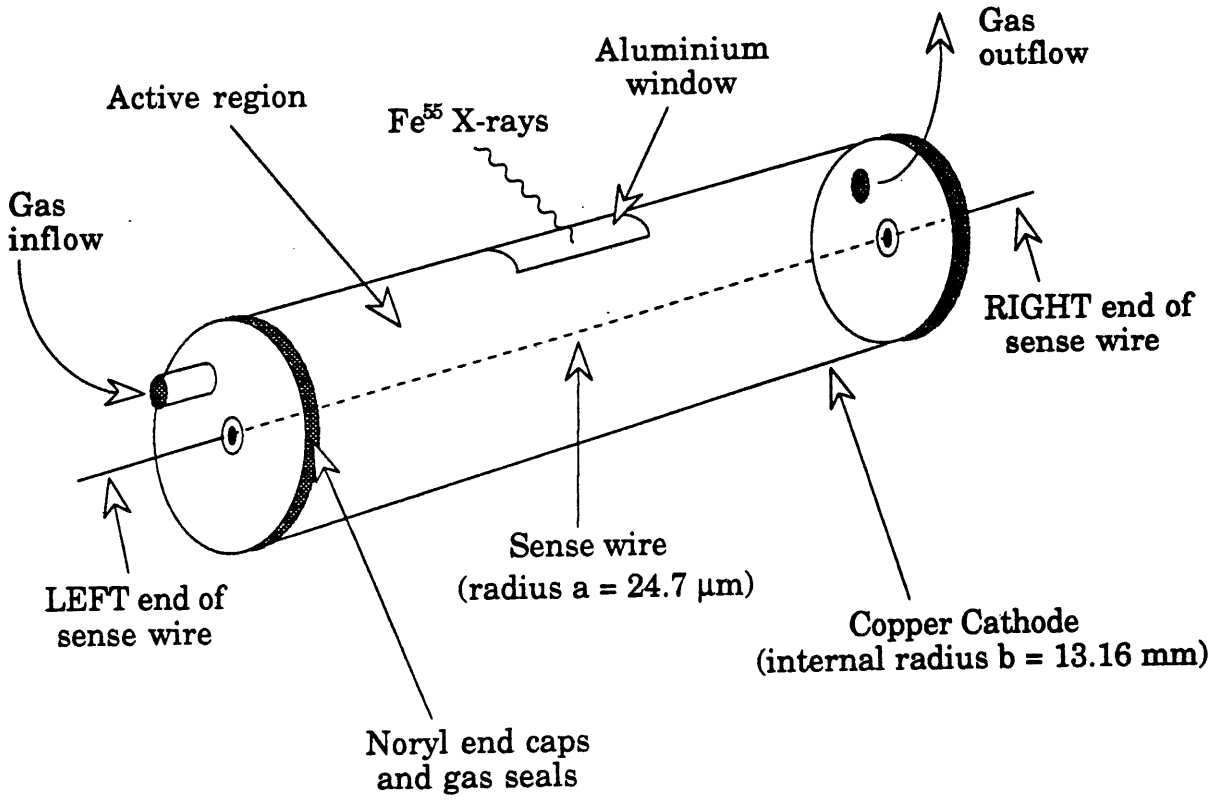

Figure 4.3.4 The SWDC.

The Fe^{55} X-ray source was placed on the aluminium window of the SWDC, centrally above the sense wire, and equi-distant from both ends of the SWDC (Figure 4.3.5).

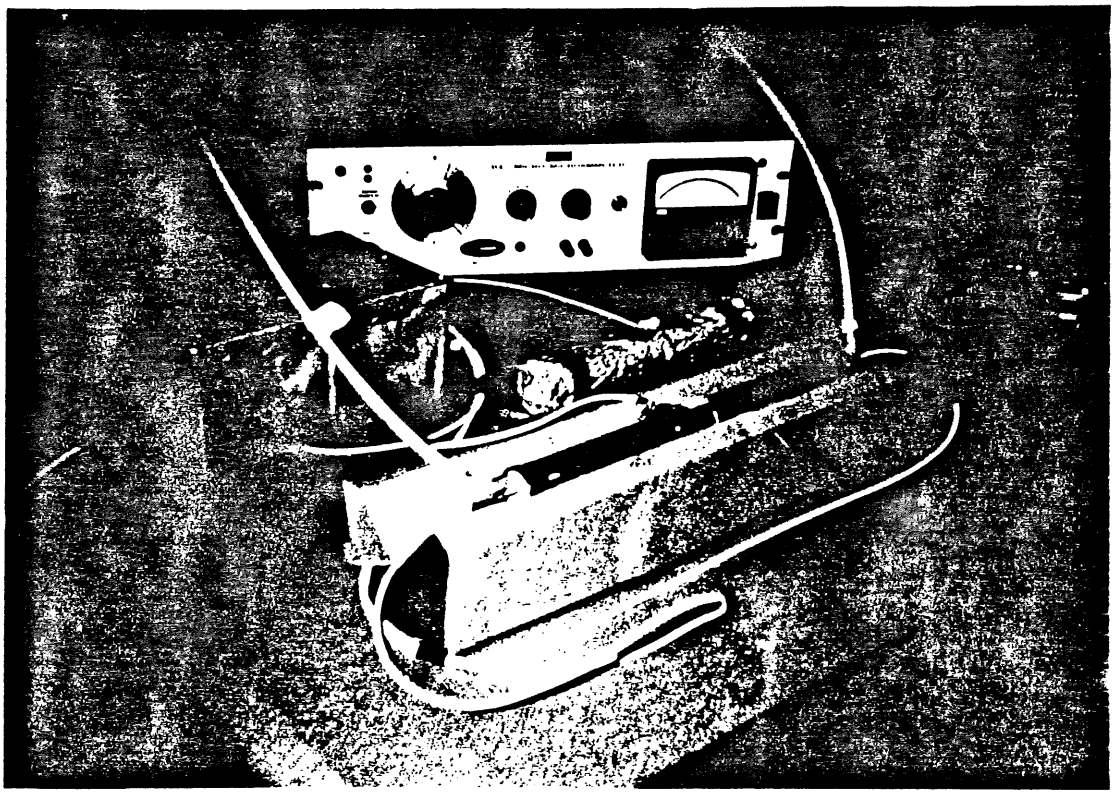

Figure 4.3.5 The SWDC and the data acquisition system.

The charge division, due to the central positioning of the source, would result in half the signal leaving the SWDC via the left channel, and half via the right. We would therefore expect the left and right pulses to be roughly equal in size (Figure 4.3.6).

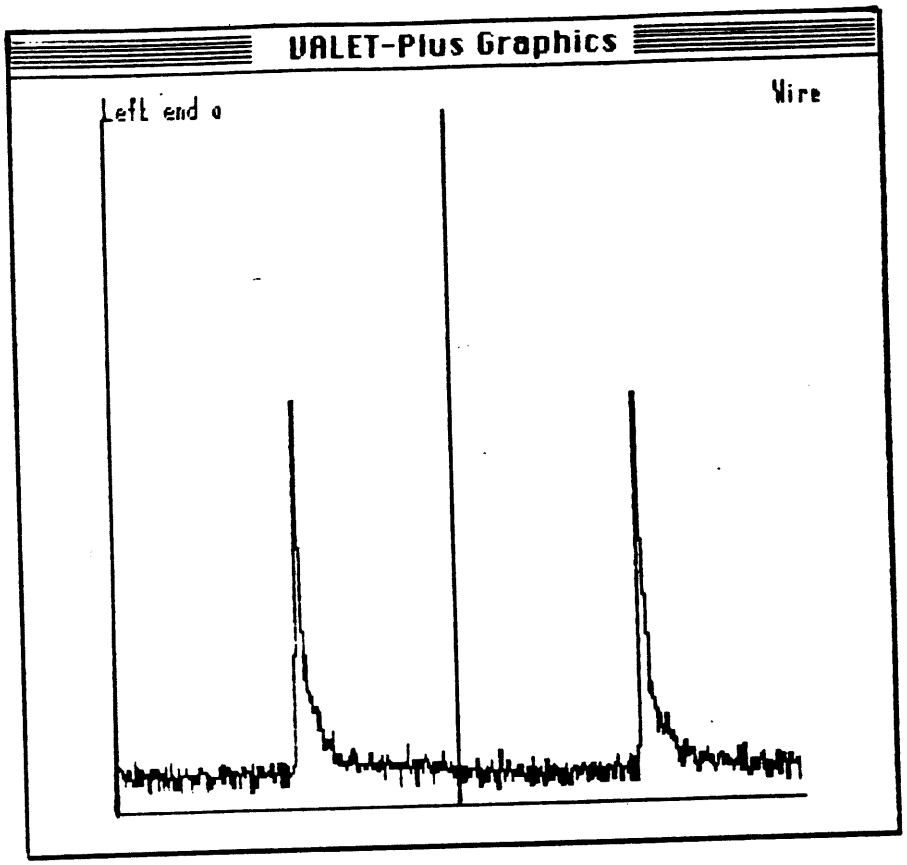

Figure 4.3.6 A non-linear digitised Fe^{55} X-ray pulse from the SWDC, showing the equi-sized left and right components of the pulse. This particular event was recorded with a sense field of 174 kV/cm.

A similar trace, as obtained with an ionising β-particle emitted from a ruthenium source, shows the characteristics of charged particle dE/dx deposition (Figure 4.3.7). The shallower rising edge of the β-particle pulse is caused by the large ranges of both the energies deposited, and the drift distances of the ionisation along the particles track to the sense wire.

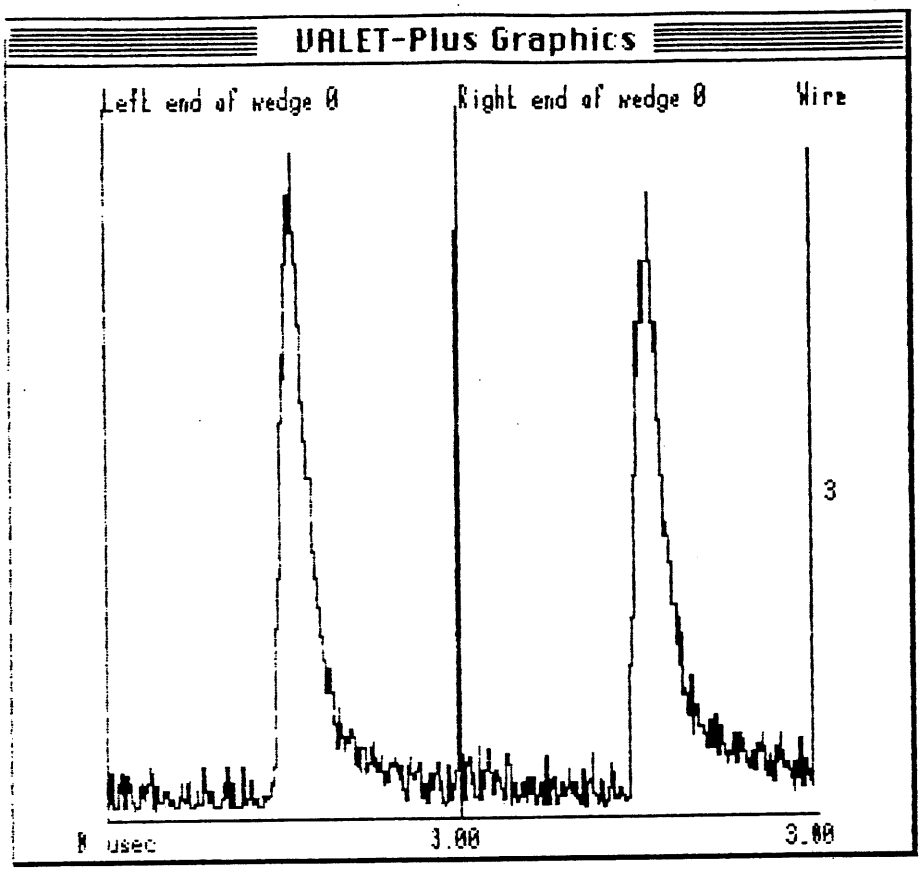

Figure 4.3.7 A non-linear digitised ruthenium β-particle pulse from the SWDC. This particular event was recorded with a sense field of 170.9 kV/cm.

4.4 The determination of $Q_{INITIAL}$

$Q_{INITIAL}$ is the total charge of the electrons produced in the initial Fe^{55} X-ray interaction. In Section 4.2 we concluded that the number of free electrons, N_e, produced in the above interaction with an argon atom, within the Ar {50%}/C_2H_6 {50%} mix, was:

$$N_e \text{ (Ar \{50\%\}/}C_2H_6 \text{ \{50\%\})} = 230 \pm 11$$

If each electron has a charge **e** (= 1.602×10^{-19} C), then $Q_{INITIAL}$ is given by Equation 4.4.

$$Q_{INITIAL} = N_e \cdot e \qquad \text{Equation 4.4}$$

which yields $Q_{INITIAL} = (230 \pm 11)\, e = (3.69 \pm 0.18) \times 10^{-17}$ C

4.5 The measurement of $Q_{COLLECTED}$

The measurement of $Q_{COLLECTED}$ was accomplished by analysing both the left and right channel outputs from the left and right ends of the sense wire respectively, with the equipment shown in Figure 4.5.1.

4.5.1 The data acquisition system

This section is described with reference to Figure 4.5.1. The signals from both ends of the sense wire were first amplified (x 30) by a set of H1 RWDC differential input preamplifiers (see Appendix A), which were powered by a low tension (LT) voltage supply. The signals were then attenuated by a factor of 10 to ensure that the input pulses were not too large for the DL300 data acquisition system [20].

The preamplifiers, attenuators, and connecting cables, were sufficiently shielded to minimise any noise pick-up. After travelling through long cables connecting the attenuators to the DL300 system, both signals were fed into a 6-bit monolithic FADC (DL305) via a delinearisation circuit.

The delinearisation of the input signals had the effect of increasing the resolution of the smaller signals to that of 8-bit, and decreasing the resolution for the larger signals to that of 4-bit.

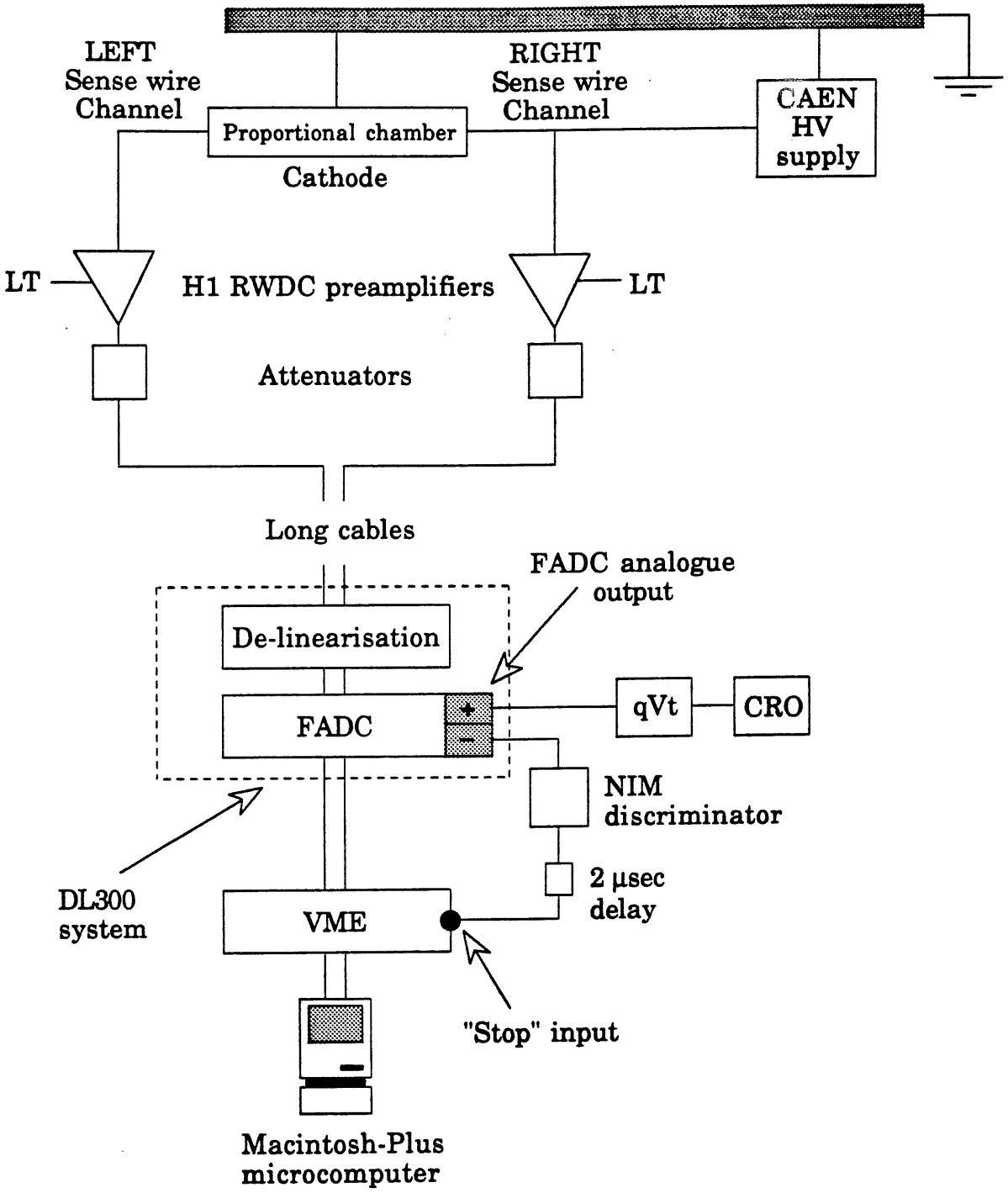

Figure 4.5.1 The data acquisition equipment used to obtain information for the measurement of $Q_{COLLECTED}$. This equipment was used with both the SWDC and the RWDC's.

The signals were then digitised, in their non-linear form, by the FADC into 256 x 10 ns time bins. The contents of each FADC 10 ns time bin were related to the H1 preamplifier output voltage, caused by the discharge of the gas gained charge through the preamplifier input resistance to ground during the time of each bin opening. Let us call the contents of time bin **i**, F_i.

The VME data acquisition system stored the 256 F_i values chronologically (the VME "window"), and then cyclically returned to the beginning to store another set, by overwriting the previous set. To preserve a pulse of interest that was stored in the VME, the overwriting had to be halted, and this was achieved by sending a "stop" pulse to the VME. The "stop" signal was provided by a LeCroy NIM octal discriminator, which produced a standard NIM output pulse when the input to it was above a set threshold. The input to the discriminator came from the negative analogue output from the FADC, and so ensured that when a pulse of interest was received, the NIM discriminator with a suitably set threshold, would produce a "stop" signal. However, it would take 2.56 μs for the VME to store all of the 256 F_i values, and so the NIM output had to be delayed by about 2 μs to ensure the storage of a complete pulse.

The data from both the left and right channels were then down-loaded to a Macintosh-plus microcomputer, where they were stored on a hard-disk. A pedestal level was then added to the stored data by the Valet-plus package [21] to ensure that no negatively filled time bins would go on to be analysed by the analysis program (Section 4.5.2). The Valet-plus package also allowed one to observe the individual pulses that

were received, printouts of which can be seen in Figures 4.3.2, 4.3.3, 4.3.6 and 4.3.7. The data was then transferred to the mainframe IBM for full analysis. The complete data acquisition system is shown in Figure 4.5.2.

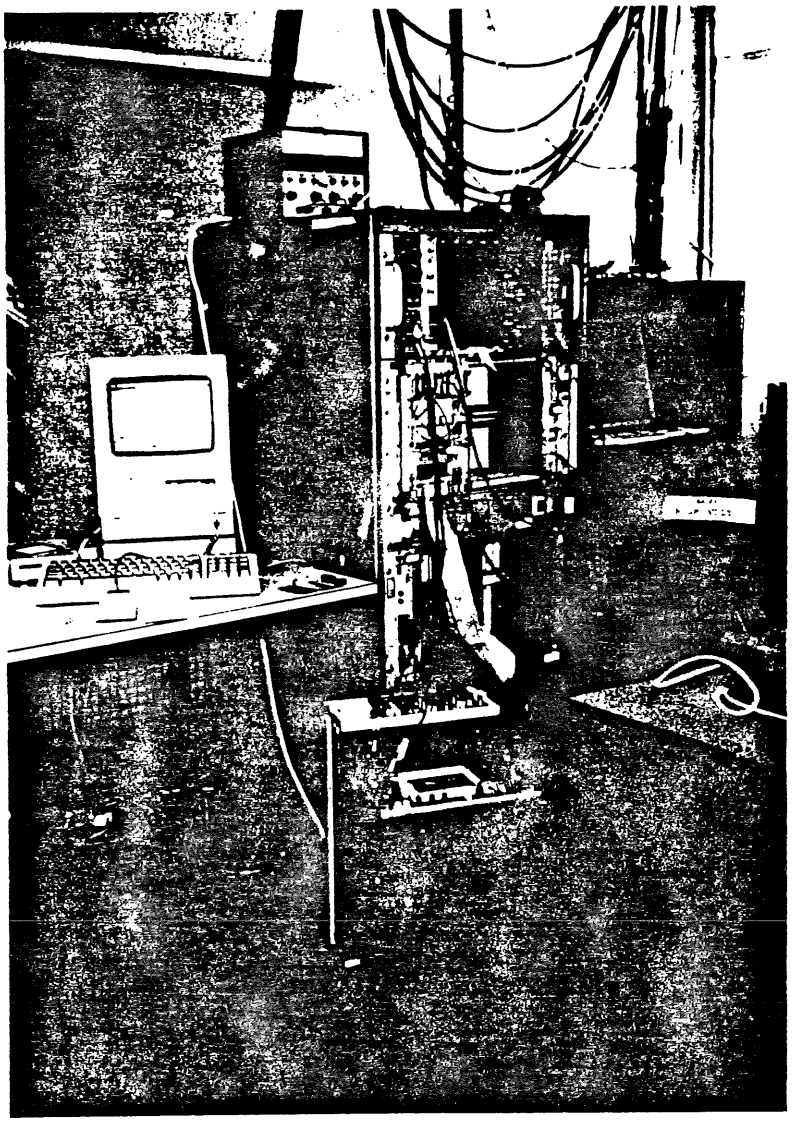

Figure 4.5.2 The data acquisition system, the DL300 crate, and the computer controlled CAEN HV supply.

4.5.2 The data analysis

The data recorded with the SWDC, and the RWDC's, consisted of runs of 1000 individual events, each run being completed at the various values of E_{SENSE}.

Each of the 1000 events within a particular run were composed of 256 F_i values in their non-linear form, for the left and right channels, and the following stages of analysis were applied separately to both. The analysis program first searched the data for pulses using a two stage hit finding technique [22], which can be summarised as follows:

(i) The non-linear data was first searched for possible areas where pulses of interest may exist. This was achieved by tagging the regions of data, within each set of 256 F_i values, where two consecutive F_i values were greater than a threshold set in the software (Figure 4.5.3). In Figure 4.5.3, which is a typical section of the total 2.56 μs VME "window", region **B** would be tagged. This may tag spuriously high levels of noise (region **A** shows typical levels of noise) as well as the actual pulses (region **B**), and so a more sophisticated hit finding method is required to discriminate between the noise and pulse tags. The data was re-linearised, and the pedestal level evaluated and subtracted before the next stage of data analysis. The main disadvantage with the DL300 system is that it sets the contents of a time bin that overflows to zero. This is, however, easily recognisable within a pulse, and the analysis software had an efficient recovery technique where it set the contents of any such bin to the maximum possible [22].

(ii) The discrimination between the noise tags and the actual pulse tag from (i), within each set of 256 F_i values, was accomplished with a

weighted difference of samples method (WDOS) [22]. This involves multiplying the contents of each time bin, F_i, by the difference between the contents of itself and the previous bin, F_{i-1}, such that WDOS is given by Equation 4.5.

$$WDOS = F_i (F_i - F_{i-1}) \qquad \textbf{Equation 4.5}$$

The WDOS plot for Figure 4.5.3 is shown in Figure 4.5.4, in which we can see that WDOS for region **A** is negligible compared to the WDOS for region **B**. The rising edge of the pulse in region **B** has the maximum value of WDOS, and with a suitably set threshold we were able to identify the bin with the maximum WDOS. This bin was labeled as bin 0.

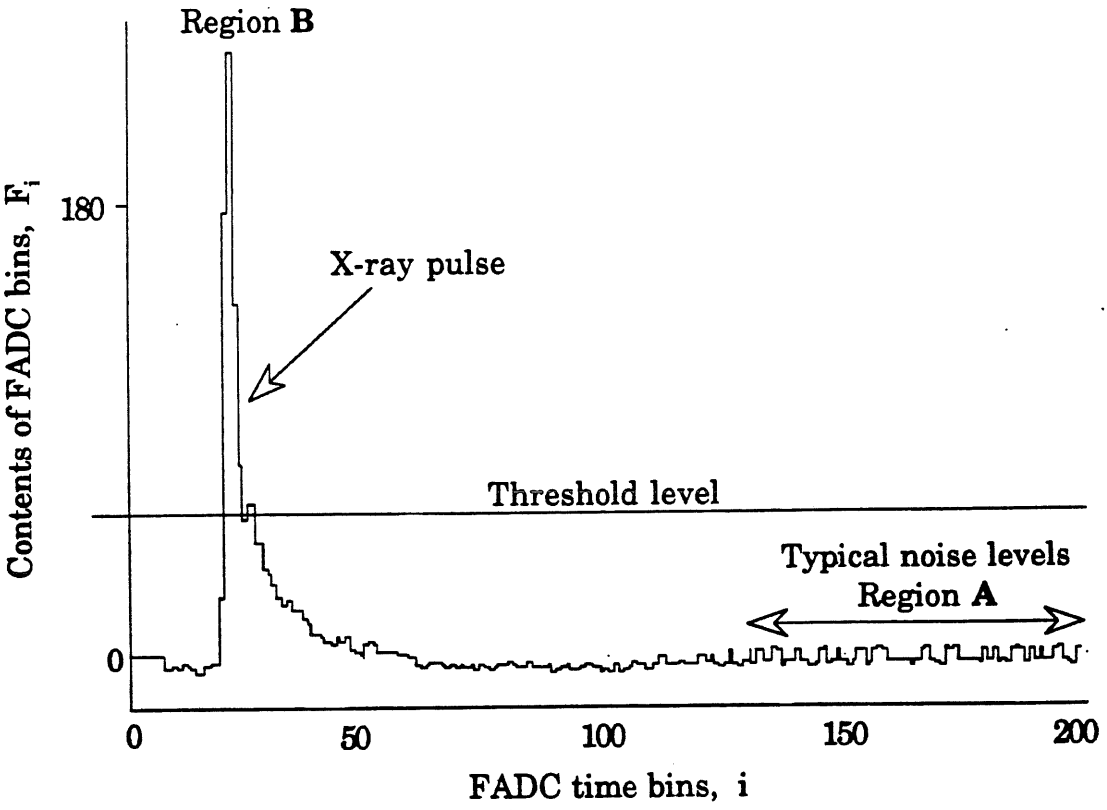

Figure 4.5.3 An expanded section of the non-linear digitised VME "window". The software set threshold is shown.

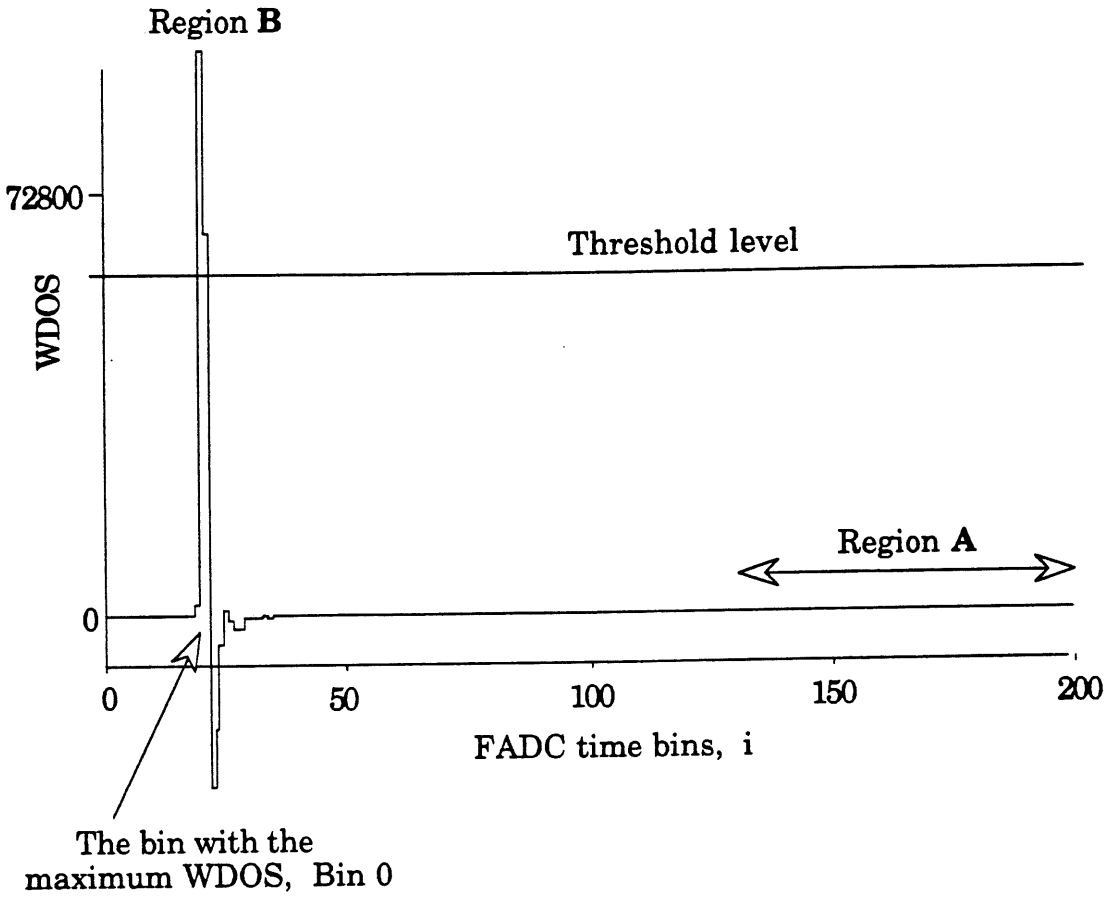

Figure 4.5.4 The WDOS plot for Figure 4.5.3. Regions **A** and **B** are again shown, with the WDOS threshold.

At this stage we have successfully found the regions within each set of 256 F_i values where there are pulses of interest, and labeled the first bin of the pulses as bin 0. The software can now integrate the contents of all the bins within some specified boundary by a bin by bin summation method. A typical X-ray pulse, that has passed through the hit finding system and had bin 0 specified, is shown in Figure 4.5.5.

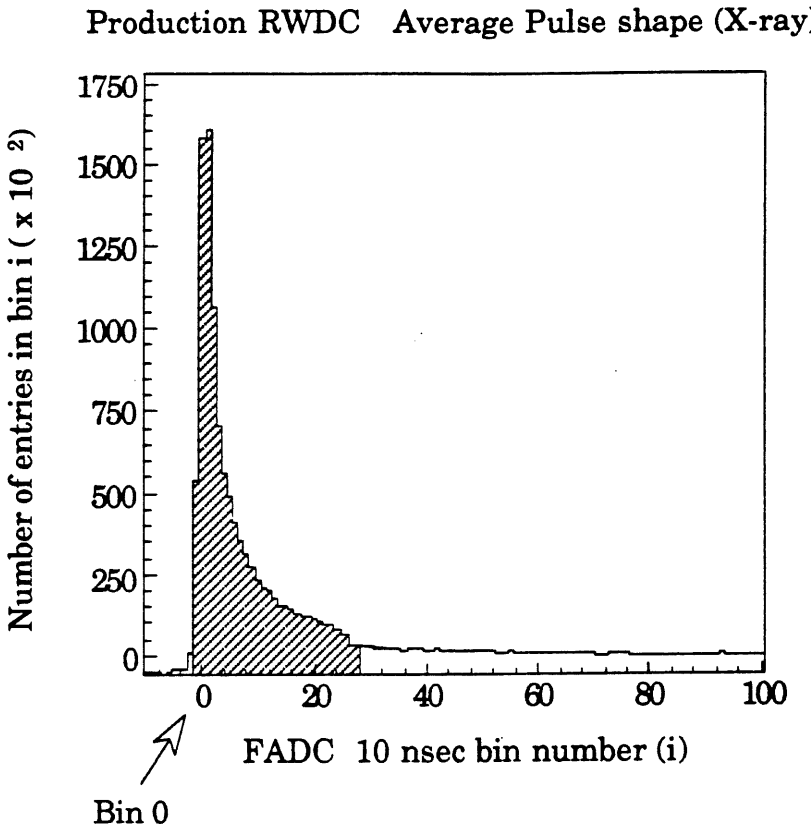

Figure 4.5.5 A typical Fe^{55} X-ray pulse, in its re-linearised digitised form, with bin 0 specified. The pulse integral was calculated for the shaded region only.

Through careful investigation, it was concluded that the best results for the determination of $Q_{COLLECTED}$ from the Fe^{55} X-ray pulses, would be obtained by summing together the contents of 30 bins, starting from bin -1 (shown as the shaded region in Figure 4.5.5). Integrating over less bins would cut out too much of the pulse, and integrating over more bins only increased the answer by about 1% as it only included more of the low level RC tail, which extended far beyond 30 time bins. This is discussed in more detail in Appendix B. So for each of the 1000

events, which had a pulse identified, the following summations were calculated by the software (Equations 4.6 and 4.7).

$$F^{L}_{TOTAL} = \sum_{i=-1}^{28} F^{L}_{i} \qquad \textbf{Equation 4.6}$$

$$F^{R}_{TOTAL} = \sum_{i=-1}^{28} F^{R}_{i} \qquad \textbf{Equation 4.7}$$

Where F^{L}_{i} and F^{R}_{i} are the contents of bin i under the left and right channel X-ray pulses respectively, and F^{L}_{TOTAL} and F^{R}_{TOTAL} are the summations over 30 bins for these channels.

The software then histogrammed the values of F^{L}_{TOTAL} and F^{R}_{TOTAL} for each of the identified pulses in each particular run. Typical Fe^{55} X-ray histograms (Gaussian distributions) are shown in Figure 4.5.6, for the left and right channels of (a) the SWDC, (b) the production RWDC, and (c) the prototype RWDC. The expected charge division effects can be seen on the left and right channel histograms for each proportional chamber as explained in Section 4.3.

The mean values of these histograms yielded average values for F^{L}_{TOTAL} and F^{R}_{TOTAL}, $\overline{F}^{L}_{TOTAL}$ and $\overline{F}^{R}_{TOTAL}$ respectively, at each value of E_{SENSE}. By calibrating the system it was possible to relate $\overline{F}^{L}_{TOTAL}$ and $\overline{F}^{R}_{TOTAL}$ to the actual charge that left the proportional chamber via the left and right channels respectively (Section 4.5.3).

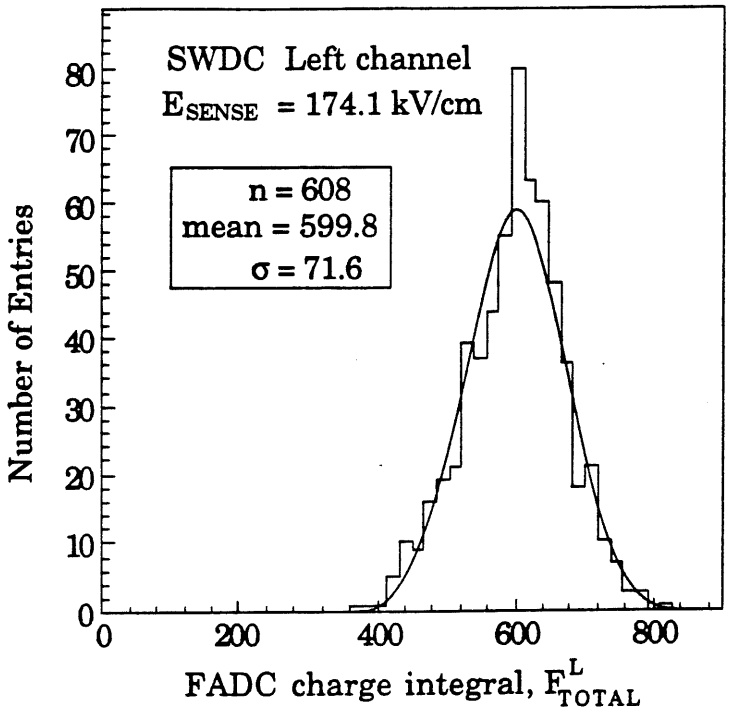

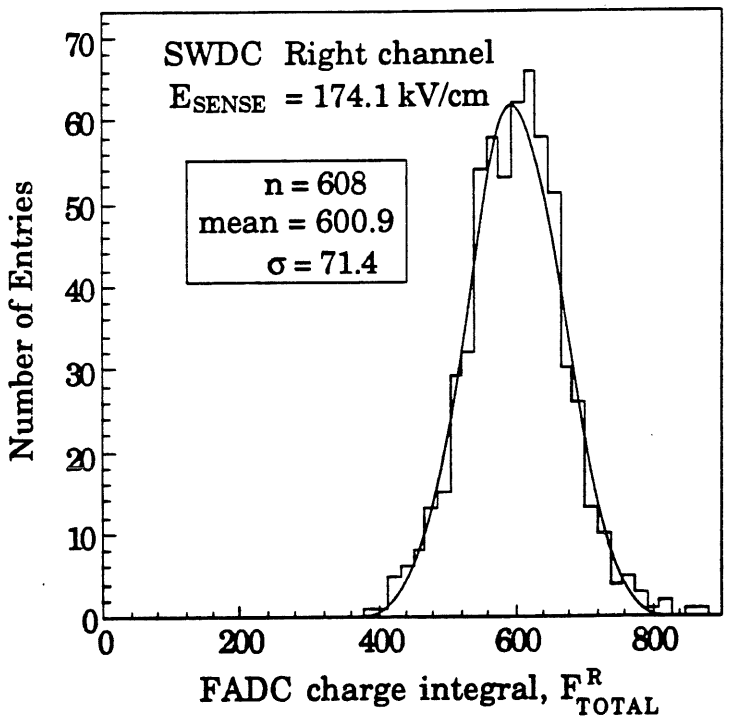

Figure 4.5.6a Histograms of F^{L}_{TOTAL} and F^{R}_{TOTAL} for the SWDC. Gaussian best fits are shown. The parameters in the box are taken from the fits.

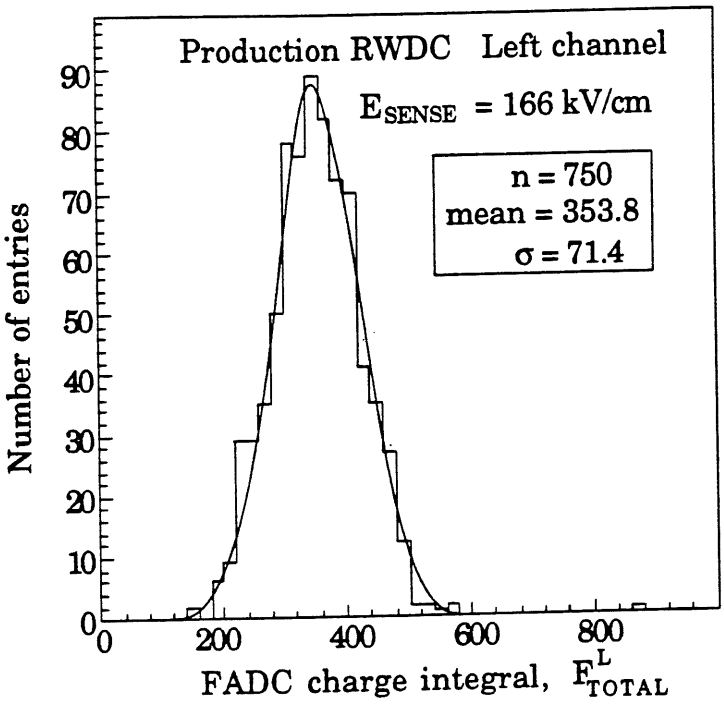

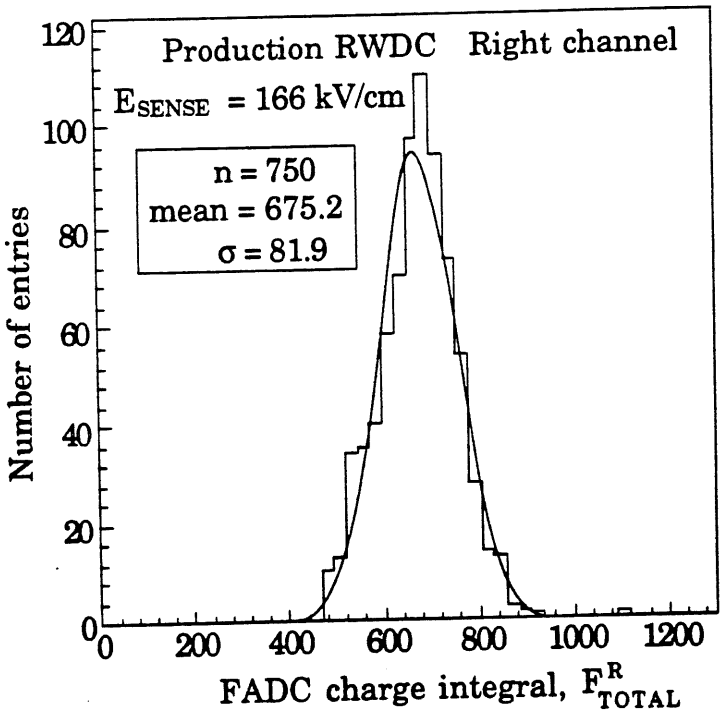

Figure 4.5.6b Histograms of F^L_{TOTAL} and F^R_{TOTAL} for the production RWDC. Gaussian best fits are shown. The parameters in the box are taken from the fits.

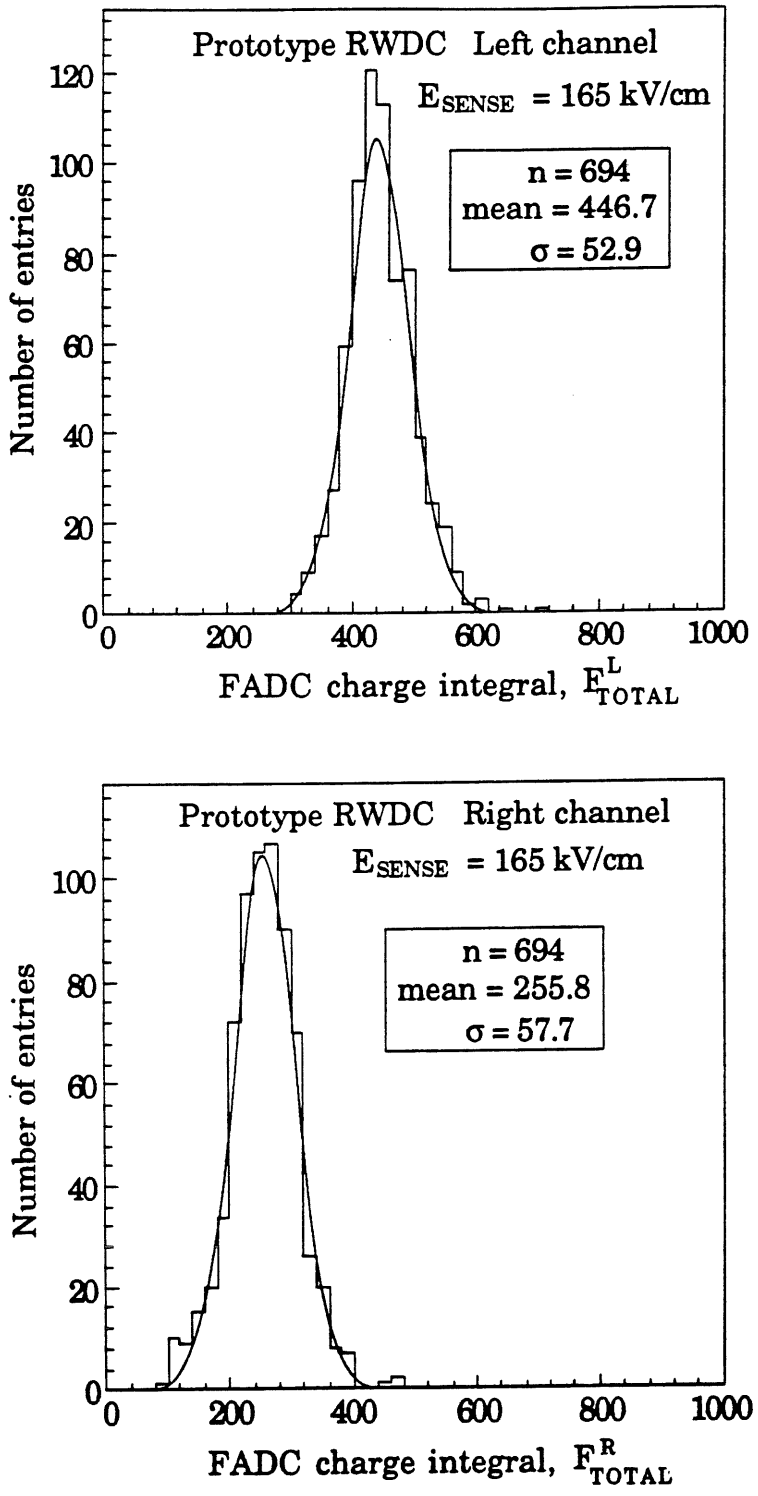

Figure 4.5.6c Histograms of F^{L}_{TOTAL} and F^{R}_{TOTAL} for the prototype RWDC. Gaussian best fits are shown. The parameters in the box are taken from the fits.

4.5.3 The calibration

We must now find a way of relating the contents of each FADC time bin, F_i^L and F_i^R, to the actual charge that discharged through the left and right channels from the sense wire during the 10 ns of time that each time bin was open. This was done by calibrating the complete data acquisition system with a standard square wave test pulse from a Tektronix PG502 signal generator (Figure 4.5.7).

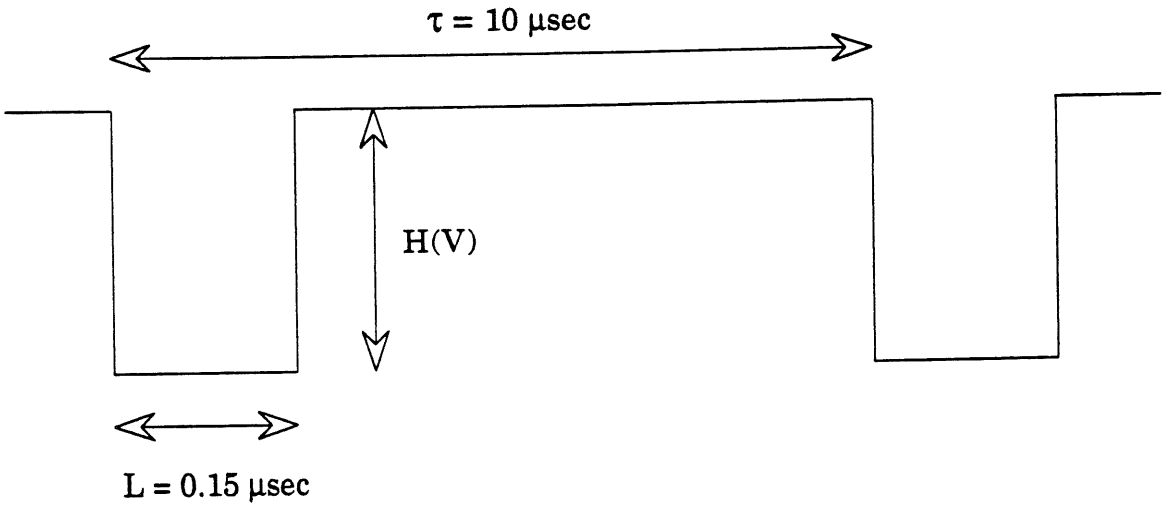

Figure 4.5.7 The standard square wave test pulse used to calibrate the system.

The test pulse was sent into the test pulse inputs of the H1 RWDC preamplifiers (Appendix A), and then through the electronics and storage system, exactly as for the X-ray pulses (Section 4.5.1). The left and right channels were calibrated separately (Figure 4.5.8), and the data was analysed in the same way as explained in Section 4.5.2.

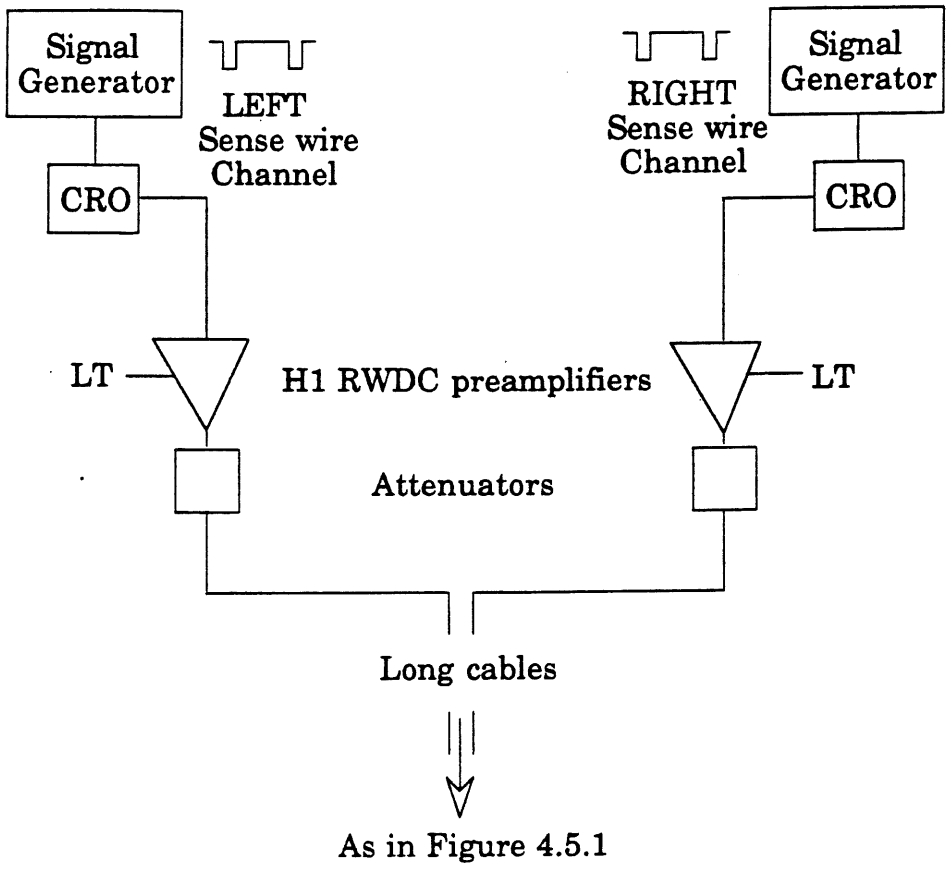

Figure 4.5.8 The equipment used to calibrate the left and right channels of the data acquisition system.

The period, τ (s), of the test pulse was set at 10 μs to ensure that not more than one pulse would be received per 2.56 μs VME "window". The width, L(s), was varied whilst keeping the height, H(V), constant at 1.5 V, to see if the electronics responded linearly. A linear response was observed, and from this analysis it was concluded that a width of L = 0.15 μs was the optimum value to use. This width resembled the approximate width of the main part of the Fe^{55} X-ray pulses received with the SWDC and the RWDC's. The parameters of the input test pulse, τ (s), L(s), and H(V), were measured with a cathode ray

oscilloscope (CRO) across the input of the FADC. A high impedance probe was used to ensure that the values read from the CRO corresponded correctly to those analysed by the FADC.

Using the test pulse with τ = 10 μs and L = 0.15 μs, results were taken at various values of H(V) ranging from 0.2 V to 1.5 V, the upper limit being the maximum possible pulse height without overflow. The calibration runs consisted of 200 individual pulses being sent into the left and right channels of the data acquisition system. Preamplifiers 1 and 2 were used on the right and left channels of the production RWDC respectively, and preamplifiers 001 and 002 were used on the right and left channels of the prototype RWDC and the SWDC respectively, and so these four preamplifier channels had to be calibrated separately.

The analysis program yielded pulses with a width of 15 time bins (15 x 10 ns = 0.15 μs), and a typical digitised square pulse, with bin 0 assigned (Section 4.5.2), can be seen in Figure 4.5.9.

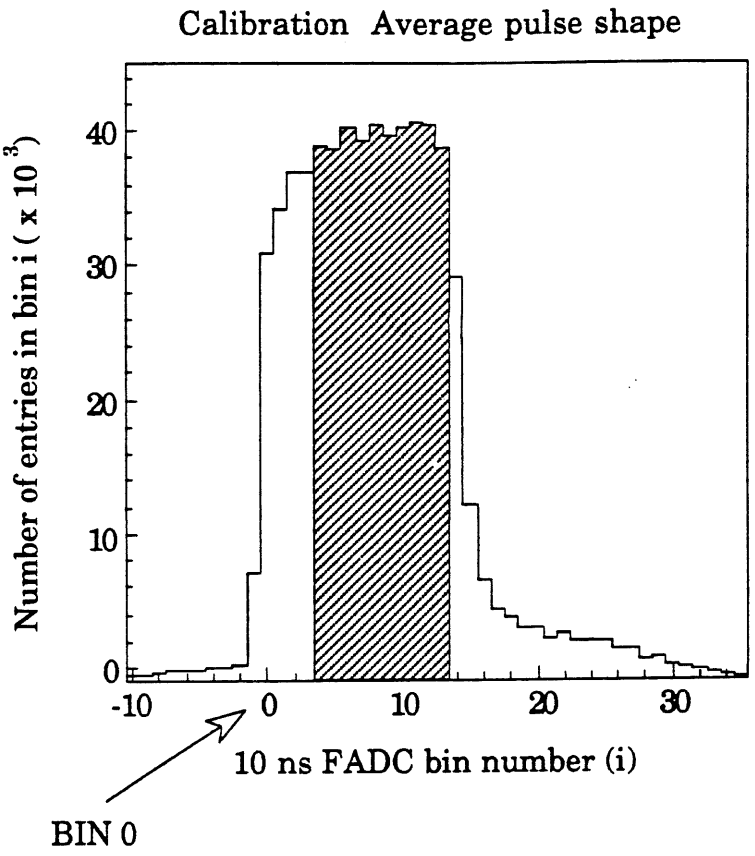

Figure 4.5.9 A typical digitised calibration square pulse from the analysis program, with bin 0 assigned. The calibration pulse integral was calculated for the shaded region only.

The rising and falling edges of the calibration pulse showed equal degrees of smoothing (integration) caused by the RC properties of the electronics (Figure 4.5.9). The bins in these areas could not be used in the calibration and so had to be removed from the analysis. Therefore only 10, out of the total 15 time bins under the calibration pulses were summed together to give the calibration pulse integral (the shaded region in Figure 4.5.9), starting from bin 3 (bin 0 was again the bin with

the maximum WDOS). For the 200 events the following summations were calculated (Equations 4.8 and 4.9).

$$F_{10}^{L} = \sum_{i=3}^{12} F_i^{L} \qquad \textbf{Equation 4.8}$$

$$F_{10}^{R} = \sum_{i=3}^{12} F_i^{R} \qquad \textbf{Equation 4.9}$$

Where F_i^L and F_i^R are the contents of bin i under the left and right channel calibration pulses respectively, and F_{10}^L and F_{10}^R are the summations over the 10 bins for these channels.

The software histogrammed the values of F_{10}^L and F_{10}^R for the 200 events in each run at the various values of H(V) (Figure 4.5.10). The means of the left and right histograms yielded $\overline{F}_{10}^L$ and $\overline{F}_{10}^R$, which are simply the average contents of 10 FADC time bins under the left and right calibration pulses respectively with a height H(V). Therefore, the average contents of just one FADC bin, under a pulse of height H(V), for the left and right channels, would be $\overline{F}_1^L$ and $\overline{F}_1^R$ respectively, where:

$$\overline{F}_1^L = \frac{\overline{F}_{10}^L}{10} \qquad \textbf{Equation 4.10}$$

$$\overline{F}_1^R = \frac{\overline{F}_{10}^R}{10} \qquad \textbf{Equation 4.11}$$

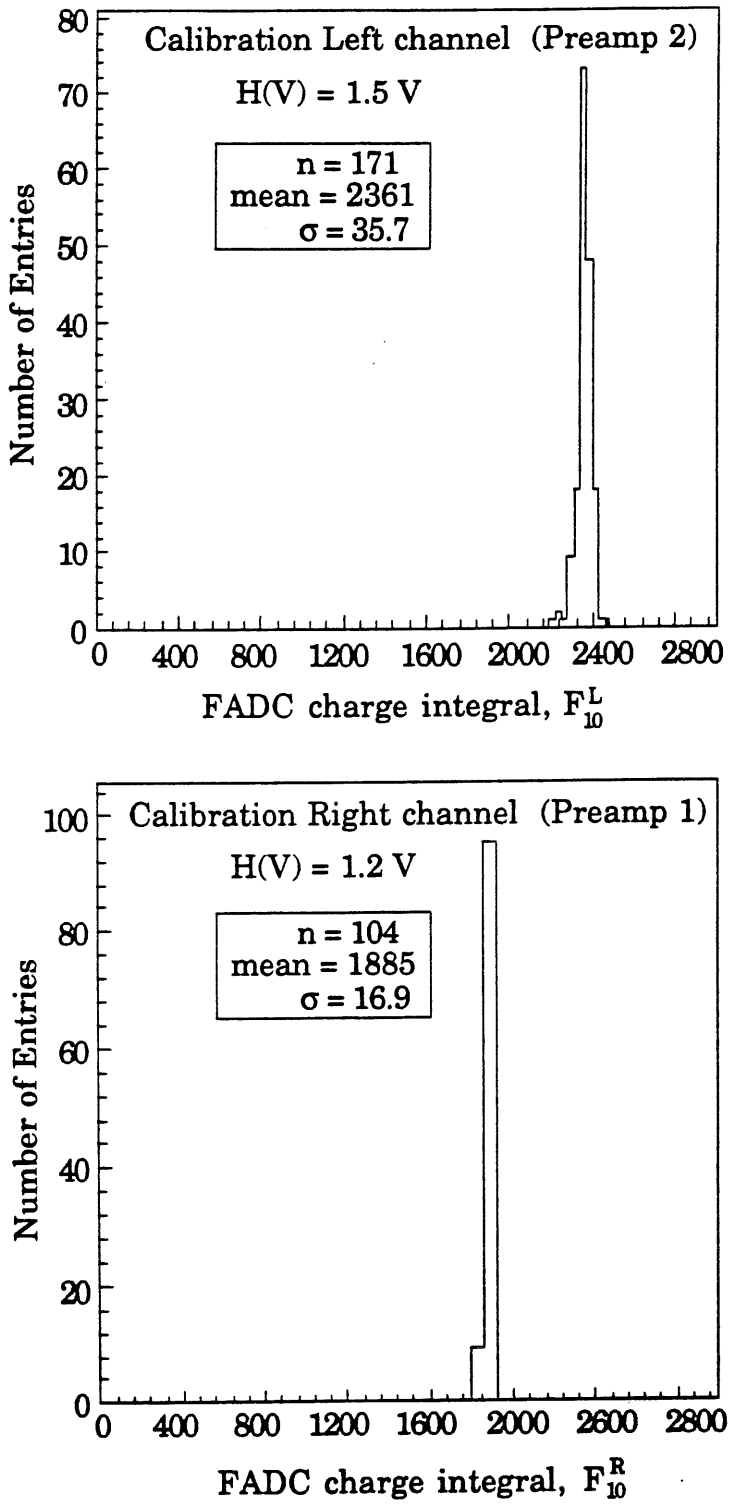

Figure 4.5.10 Typical calibration histograms of F_{10}^{L} and F_{10}^{R} for the channels with preamplifiers 1 and 2.

4.5.4 The final calculation of $Q_{COLLECTED}$

We can now plot a graph of $\overline{F}_1^L$ and $\overline{F}_1^R$ versus H(V) for the four preamplifier channels (Figure 4.5.11). The equation for the straight line plotted for the right channel is:

$$\overline{F}_1^R = (m^R)\,H(V) + \Lambda^R \qquad \textbf{Equation 4.12}$$

where

$\overline{F}_1^R$ is the average contents of one FADC bin for the right channel,

m^R is the gradient of the line plotted for the right channel (Figure 4.5.11),

H(V) is the height of the input calibration pulse from the signal generator, and,

Λ^R is the intercept on the y-axis of the line plotted for the right channel (Figure 4.5.11).

And similarly for the left channel (Equation 4.13).

$$\overline{F}_1^L = (m^L)\,H(V) + \Lambda^L \qquad \textbf{Equation 4.13}$$

The manufacturers specifications of the H1 RWDC preamplifiers [8] states that:

(i) for a test pulse input of 1 V, an output of 0.83 V is produced, and

(ii) for a chamber pulse input of 1 μA, an output of 0.105 V is produced.

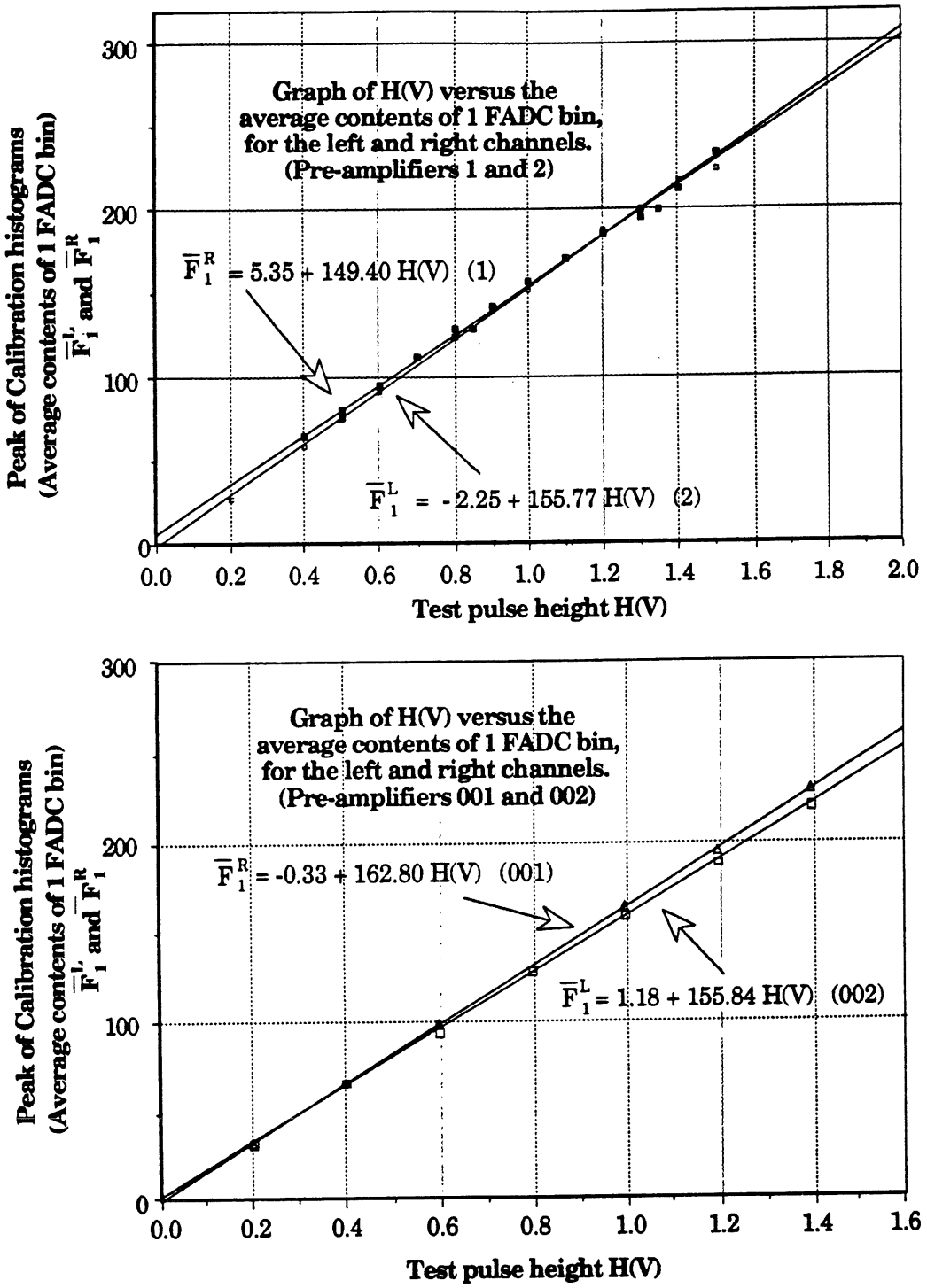

Figure 4.5.11 Calibration graphs for the four preamplifier channels (1/2, 001/002), showing $\overline{F}_1^L$ and $\overline{F}_1^R$ versus H(V).

From (i) we can show that with a test pulse input of 1.2 V, the output would be 1.0 V. And hence with a test pulse input of H(V), the preamplifier output, V_{OUTPUT}, would be:

$$V_{OUTPUT} = \frac{H(V)}{1.2} \qquad \textbf{Equation 4.14}$$

An output of 1.0 V would also be produced when 9.5 μA flows through the preamplifier input resistance to ground (from ii). And therefore, in the case when the input to the preamplifier is the output current, I(A), from the sense wire of a proportional chamber, the same output, V_{OUTPUT}, would be produced when:

$$I(A) = (9.5 \times 10^{-6})\, V_{OUTPUT} = \frac{(9.5 \times 10^{-6})\, H(V)}{1.2} \qquad \textbf{Equation 4.15}$$

As both a test pulse input of H(V), and a chamber pulse input of I(A), would produce the same output, V_{OUTPUT}, the pulse analysis of this output would yield the same results for both. We can therefore relate H(V) to an equivalent input current of I(A):

$$H(V) = (1.27 \times 10^{5})\, I(A) \qquad \textbf{Equation 4.16}$$

But we know that:

$$I(A) = \frac{Q(C)}{\Delta t} \qquad \textbf{Equation 4.17}$$

where Q(C) is the charge that flowed, in a time Δt, to produce the current I(A). The calibration results relate the average contents of one FADC time bin (Δt = 10 ns), $\overline{F}_1^L$ and $\overline{F}_1^R$, for the left and right channels, to H(V) respectively. Using Equation 4.17 we can show that:

$$I(A) = (1 \times 10^{8})\, Q(C) \qquad \textbf{Equation 4.18}$$

and using Equation 4.16 we can relate H(V) to an equivalent charge input, Q(C), during the time of one FADC bin:

$$H(V) = (1.27 \times 10^{13})\, Q(C) \qquad \textbf{Equation 4.19}$$

We can now derive two general equations, from Equations 4.12, 4.13, and 4.19, relating the contents of one FADC time bin (bin i), $\overline{F}_i^L$ and $\overline{F}_i^R$, to the charge, $Q_i^L(C)$ and $Q_i^R(C)$, that flowed from the proportional chamber during the time span of bin i, via the left and right channels, respectively:

$$\overline{F}_i^L = (m^L)(1.27 \times 10^{13})\, Q_i^L(C) + \Lambda^L \qquad \textbf{Equation 4.20}$$

$$\overline{F}_i^R = (m^R)(1.27 \times 10^{13})\, Q_i^R(C) + \Lambda^R \qquad \textbf{Equation 4.21}$$

However, the integration of the X-ray pulses was over 30 FADC bins, where the contents of the bins were summed together and then histogrammed to give $\overline{F}_{TOTAL}^L$ and $\overline{F}_{TOTAL}^R$ (Section 4.5.2). Therefore from Equations 4.6, 4.7, 4.20, and 4.21, we can relate the means of the X-ray histograms for the left and right channels, at the various values of E_{SENSE}, to the actual charge, $Q_{TOTAL}^L(C)$ and $Q_{TOTAL}^R(C)$, that was collected during the time span of the 30 bins from the left and right ends of the sense wire respectively:

$$\overline{F}_{TOTAL}^L = \sum_{i=-1}^{28} \{(m^L)(1.27 \times 10^{13})\, Q_i^L(C) + \Lambda^L\}$$
$$= (m^L)(1.27 \times 10^{13})\, Q_{TOTAL}^L(C) + 30\Lambda^L \qquad \textbf{Equation 4.22}$$

$$\overline{F}_{TOTAL}^R = \sum_{i=-1}^{28} \{(m^R)(1.27 \times 10^{13})\, Q_i^R(C) + \Lambda^R\}$$
$$= (m^R)(1.27 \times 10^{13})\, Q_{TOTAL}^R(C) + 30\Lambda^R \qquad \textbf{Equation 4.23}$$

$Q_{COLLECTED}$ is simply the total charge that left the proportional chamber via both channels, and so:

$$Q_{COLLECTED}(C) = Q^{L}_{TOTAL}(C) + Q^{R}_{TOTAL}(C) \qquad \textbf{Equation 4.24}$$

which becomes:

$$Q_{COLLECTED}(C) = \left(\frac{\overline{F}^{L}_{TOTAL} - 30\Lambda^{L}}{(1.27 \times 10^{13})\, m^{L}} + \frac{\overline{F}^{R}_{TOTAL} - 30\Lambda^{R}}{(1.27 \times 10^{13})\, m^{R}} \right) \qquad \textbf{Equation 4.25}$$

We have now related $Q_{COLLECTED}(C)$ to the means of both the left and right channel histograms using the calibration data. In Section 4.4 we discussed how $Q_{INITIAL}$ was calculated, and from this (Equation 4.4) we can evaluate the gas gain factor, G, using Equations 4.1 and 4.25:

$$G = \frac{Q_{COLLECTED}}{Q_{INITIAL}} = \frac{\left(\frac{\overline{F}^{L}_{TOTAL} - 30\Lambda^{L}}{(1.27 \times 10^{13})\, m^{L}} + \frac{\overline{F}^{R}_{TOTAL} - 30\Lambda^{R}}{(1.27 \times 10^{13})\, m^{R}} \right)}{(3.69 \times 10^{-17})} \qquad \textbf{Equation 4.26}$$

The results from this analysis can be found in Chapter 5.

4.6 The measurement of $I_{INITIAL}$

$I_{INITIAL}$ is the current that is caused by the flow of the free electrons produced in the initial Fe^{55} X-ray interaction. If $Q_{INITIAL}$ is the charge produced per X-ray event, then:

$$I_{INITIAL}(A) = Q_{INITIAL}(C) \,.\, \kappa \qquad \textbf{Equation 4.27}$$

where κ is the rate at which Fe^{55} X-ray interactions occur within the chamber. Using the value of $Q_{INITIAL}$ obtained in Section 4.4, Equation 4.27 becomes:

$$I_{INITIAL}(A) = (\{3.69 \pm 0.18\} \times 10^{-17}) \,.\, \kappa \qquad \textbf{Equation 4.28}$$

And so to determine $I_{INITIAL}$ we must evaluate κ (in s^{-1}). This method of determining the gas gain factor, G, could only be used with

the SWDC, and so the following methods for determining κ were used solely with the SWDC.

4.6.1 The LeCroy qVt multichannel analyser method

The LeCroy qVt multichannel analyser is a charge, voltage, time analyser. Used as a voltage analyser, the qVt histogrammed pulses according to their maximum height. Using the positive analogue output from the FADC to activate the qVt (Figure 4.5.1), we could obtain a pulse height distribution of the chamber output. This distribution could then be used to determine κ.

Each bin of the qVt filled up in respect of the height of the pulses received. If we set the qVt running for a time T, and then summed the contents of each qVt bin under the X-ray distribution, we could evaluate the number of X-ray pulses that occurred within the time T. A typical qVt trace is shown in Figure 4.6.1, which was obtained with the SWDC, with E_{SENSE} = 170 kV/cm, and using the Fe^{55} X-ray source. The boundaries of the X-ray Gaussian are α and β.

The x-axis corresponds to the qVt bins, and the y-axis to the number of entries within each bin, which could be calibrated using the various "counts full scale" settings on the qVt.

The X-ray Gaussian distribution can be seen to the right of, and totally separate from, the noise. We could therefore sum the contents of the bins which were under the X-ray Gaussian (within the boundaries α and β), ignoring the noise. And hence κ could be evaluated from Equation 4.29.

$$\kappa = \sum_{i=\beta}^{\alpha} \frac{n_i}{T} \qquad \text{Equation 4.29}$$

Where n_i is the number of entries in bin i, T is the time of analysis, and α and β are the boundaries of the summation, as in Figure 4.6.1.

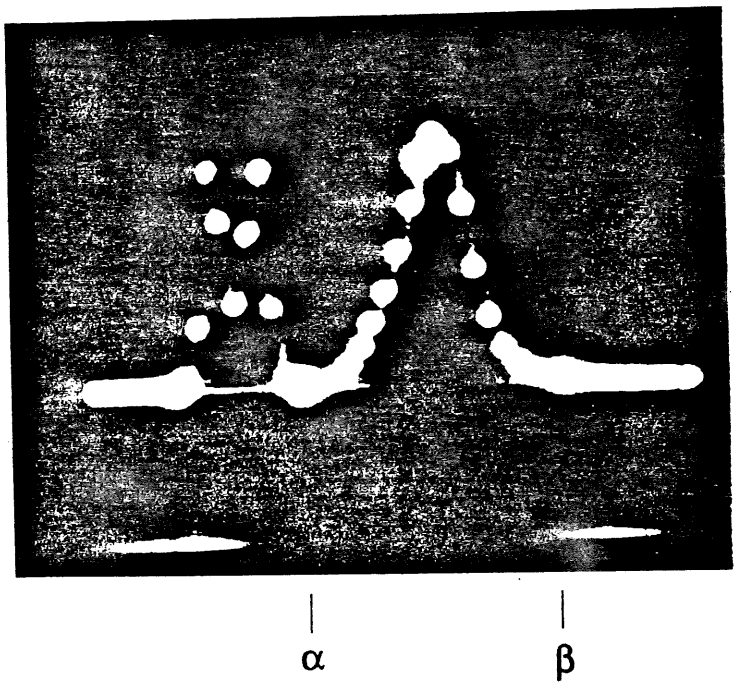

Figure 4.6.1 A typical qVt trace of an Fe^{55} X-ray distribution as displayed on a CRO, from the SWDC with E_{SENSE} = 170 kV/cm. The boundaries α, and β, of the X-ray Gaussian are shown.

A similar qVt distribution was obtained, but without the Fe^{55} X-ray source placed on the SWDC, and only the noise to the left of Figure 4.6.1 could be seen. This showed that the qVt was in fact responding correctly to the X-ray pulses. We repeated the analysis at various values of E_{SENSE}, and the expected variation of the peaks of the

qVt distributions with G was observed, however no significant effect on the rate was noticed.

This method was checked by sending a pulse of known frequency into the qVt, and it was found that κ could be determined to within 10%. However, due to the high levels of noise saturating the input to the qVt, not all of the X-rays that occurred were registered. Hence we could only establish a lower limit on κ:

$$\kappa_{LOWER} = (3700 \pm 1000)\ s^{-1}$$

This method clearly discriminates between the Fe^{55} X-ray pulses, and any background level that may exist.

4.6.2 The NIM discriminator threshold method

The input to the discriminator was provided by the negative analogue output from the FADC (Section 4.5.1). The number of pulses that left the negative output of the FADC was simply the number of pulses that left the chamber. And hence by counting the number of pulses that left the FADC, we could evaluate κ. This method was tested by using a pulse of known frequency to trigger the NIM discriminator, and it was concluded that κ could be determined to within 10%.

By varying the threshold of the NIM discriminator, and counting the number of standard NIM pulses produced with the source on and off the SWDC with a Borer scalar, a graph of counts per second versus threshold voltage (V_T) was plotted (Figure 4.6.2). This showed that at the various values of V_T, the counts with the source on were consistently higher than with the source off. This difference was due to

the X-ray events. The difference between the sets of data with the source on and off is shown in Figure 4.6.3, with error bars originating from both counts on and off. Here we see a step function, with the sharp decrease in ΔCounts occurring at 1.5 V, caused by the X-ray events being rejected when $V_T > 1.5$ V. The region where $V_T < 1.5$ V, ΔCounts gives the rate of the X-ray events, again which is independent of any background. A value of $\kappa = (3800 \pm 700)\ s^{-1}$ can be obtained from Figure 4.6.3.

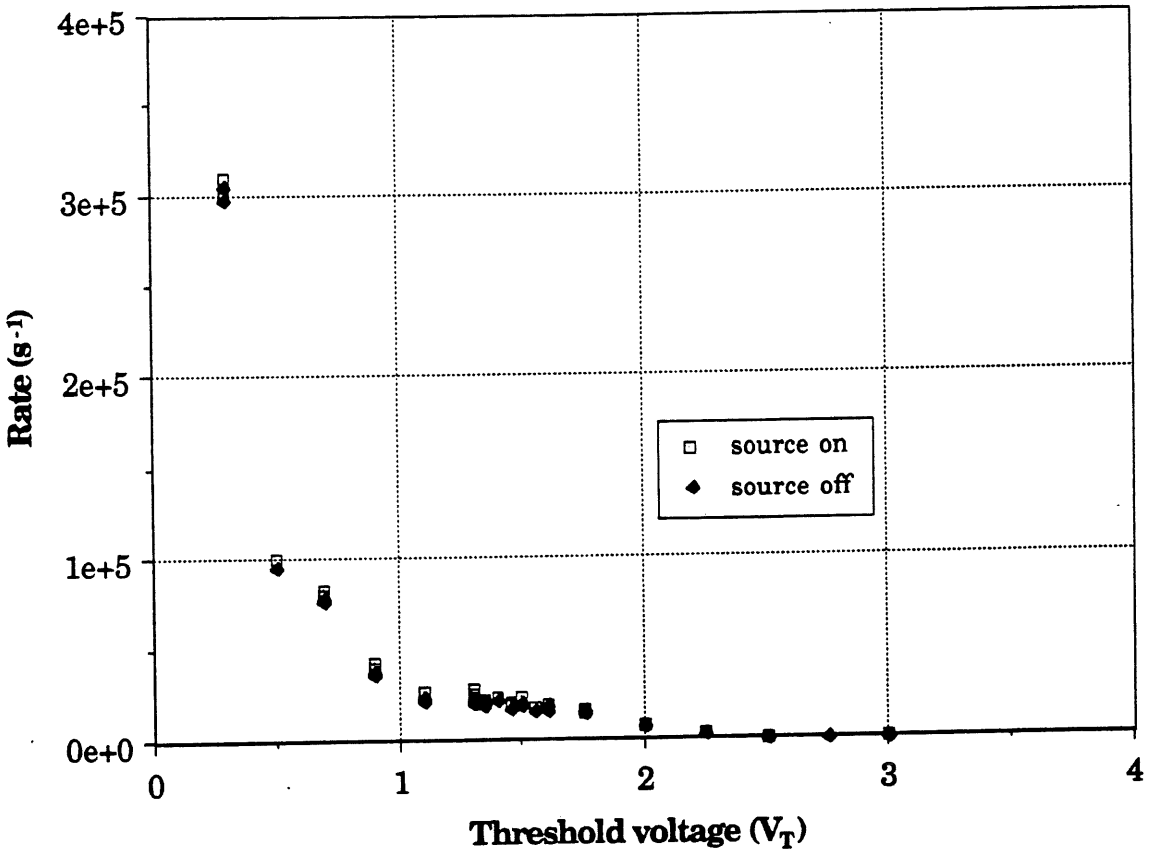

Figure 4.6.2 Counts per second, with the source on and off of the SWDC, versus the discriminator threshold voltage.

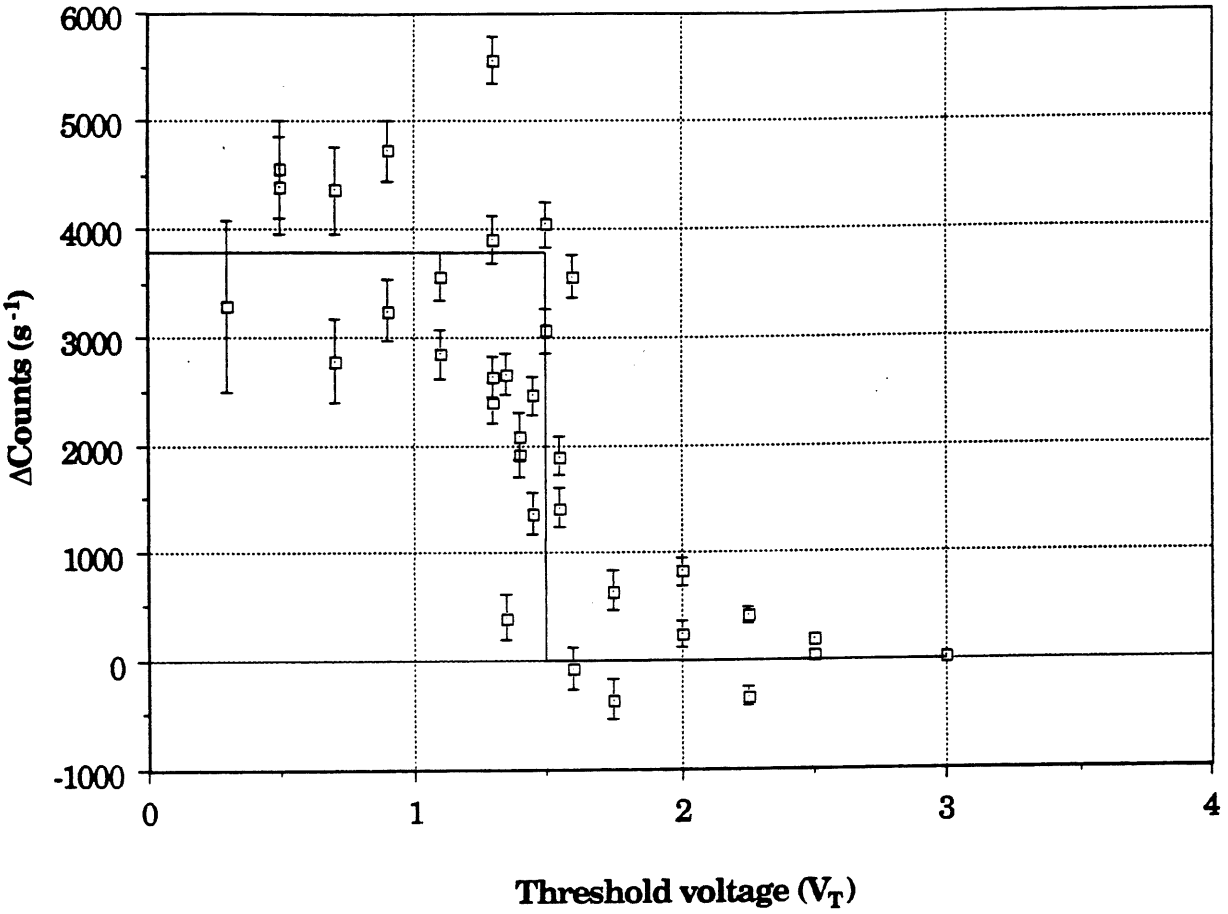

Figure 4.6.3 ΔCounts versus threshold voltage. The line plotted is to indicate where the step function lies.

4.6.3 The "random VME window" method

In this method, the input to the NIM discriminator, the negative analogue output pulse from the FADC, was replaced with a signal from a Tektronix PG502 signal generator, the height of which was set above the threshold of the NIM discriminator. This triggered the NIM discriminator to produce standard output pulses at a rate determined by

the frequency of the signal generator output. This provided the "stop" signal to the VME, and essentially opened the VME storage "window" at the frequency of the signal from the signal generator, which had the effect of looking randomly at the signal from the sense wire of the SWDC, for intervals of 2.56 μs.

By counting the number of actual X-rays recorded by the VME in a certain number of "window" openings, with a correction for the number of pulses just inside or outside the window, the value of κ could be determined from Equation 4.30.

$$\kappa = \frac{\eta}{(2.56 \times 10^{-6})\,P} \qquad \textbf{Equation 4.30}$$

where P is the number of random "window" openings, and η is the number of "windows" with definite X-rays visible. From this analysis, which was repeated several times over various values of P, the value of κ was determined to be:

$$\kappa = (3000 \pm 500)\ s^{-1}$$

which is automatically independent of any background secondary processes.

4.6.4 The final evaluation of $I_{INITIAL}$

The value of κ must be a measure of the rate of the large energy depositions from the Fe^{55} X-ray interactions, and not be in any way related to background emissions, such as secondary processes. It is shown that each method used to determine κ measures only the pulses produced by the Fe^{55} X-ray interactions.

Taking the weighted mean of κ from the three methods explained above, $\overline{\kappa} = 3330 \pm 380\ s^{-1}$, we can determine $I_{INITIAL}$ from Equation 4.28:

$$I_{INITIAL}(A) = (\{3.69 \pm 0.18\} \times 10^{-17})(3330 \pm 380)$$
$$= (1.29 \pm 0.15) \times 10^{-13}\ A \qquad \textbf{Equation 4.31}$$

4.7 The measurement of $I_{COLLECTED}$

The positive ions produced in the initial interaction and subsequent gas gain (total charge = $Q_{COLLECTED}$), are attracted to the cathode of the drift chamber. This produces a current $I_{COLLECTED}$ at the cathode which is easier to measure than the current from the sense wire, because the cathode is earthed, whereas the sense wire is held at positive HV.

The Keithley instruments pico-ammeter (pA) was connected to a common earth with the CAEN HV supply, creating a closed circuit (Figure 4.7.1). Instead of the cathode being connected directly to earth, a pA and resistance chain, R, were connected in series. The resistance chain was included to protect the pA from possible current surges. We varied the value of R from 47 MΩ to 282 MΩ, in steps of 47 MΩ, to examine the effects of R upon $I_{COLLECTED}$. We observed that $I_{COLLECTED}$ was independent of R, and for satisfactory protection at the more sensitive settings of the pA, R was set at 282 MΩ.

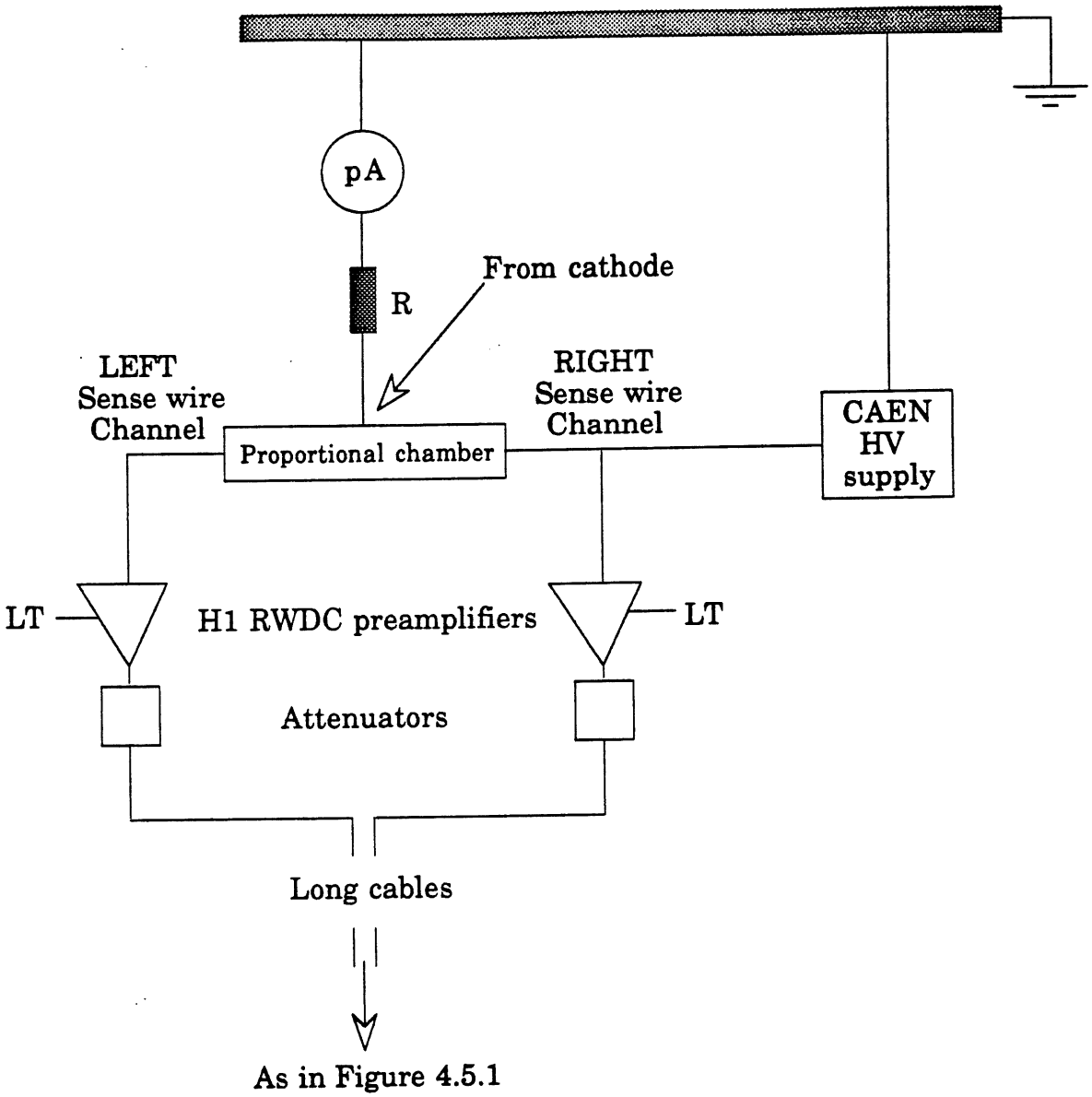

Figure 4.7.1 The equipment used to measure $I_{COLLECTED}$.

The inclusion of R in series with the cathode and ground would raise the potential of the cathode, and so reduce E_{SENSE} and consequently G. At the nominal value of E_{SENSE} = 170 kV/cm the average current from the cathode, caused by the Fe^{55} X-ray source, was measured to be

$I_{COLLECTED}$ = 25 nA (from the irradiation exposure studies, Chapter 7), and with R = 282 MΩ the corresponding change in the cathode potential would be:

$$\Delta V_c = I_{COLLECTED} . R = (25 \times 10^{-9})(282 \times 10^{6}) = +7\,V \qquad \textbf{Equation 4.32}$$

This would decrease E_{SENSE} by ΔE_{SENSE}, and from Equation 3.3,

$$\Delta E_{SENSE} = 64.49\ \Delta V$$

where ΔV is the change in the potential difference between the sense wire and the cathode ($\Delta V = -\Delta V_C = -7$ V). Therefore:

$$\Delta E_{SENSE} = -\ 0.5\ kV/cm$$

This is a 3% decrease in E_{SENSE}. Hessing and Kadel [16] suggest that the value of k in Equation 3.4 is +0.13 (with E_{SENSE} measured in kV/cm). And so Equation 3.5 becomes:

$$\Delta(\ln[G]) = 0.13\,(\Delta E_{SENSE}) \qquad \textbf{Equation 4.33}$$

Assuming that our results will resemble the results of Hessing and Kadel, and with ΔE_{SENSE} = - 0.5 kV/cm, Equation 4.33 becomes:

$$\ln[G_2] - \ln[G_1] = 0.13 \times (-0.5) = -\ 0.065 \qquad \textbf{Equation 4.34}$$

where G_1 and G_2 are the same as in Equation 3.4. It follows that:

$$G_2 = (0.94)\,G_1 \qquad \textbf{Equation 4.35}$$

which corresponds to a 6% drop in gas gain. Therefore, with the introduction of the 282 MΩ protection resistance, the gas gain would drop by 6%. The average pulse height would correspondingly be 6%

smaller. A reduction roughly of this magnitude was observed with the qVt.

To check whether the pA functioned correctly at the frequencies we were working with ($\overline{\kappa}$ = 3330 ± 380 s^{-1}), a square wave of known frequency, width, and height was sent into the pA via a 47 MΩ resistor. A value for I_{RMS} could be calculated, and then compared with the measured $I_{COLLECTED}$. Repeating this at various values of frequency, we were able to conclude that the pA responded correctly to the frequencies of $I_{COLLECTED}$.

Readings for $I_{COLLECTED}$ were taken at various values of E_{SENSE}, ranging from 97 kV/cm to 258 kV/cm, with the source on and off. The background current was subtracted from the current with the source on, and with this corrected value of $I_{COLLECTED}$, and the knowledge of $I_{INITIAL}$ (Section 4.6), we can work out G, using Equations 4.1 and 4.31:

$$G = \frac{I_{COLLECTED}}{I_{INITIAL}} = \frac{I_{COLLECTED}}{(1.29 \times 10^{-13})} \qquad \textbf{Equation 4.36}$$

The results from this analysis are tabulated in Table 5.2.4, and are shown graphically in Figure 5.2.4, for the SWDC only.

The measurements of $I_{COLLECTED}$, and the background current with the pA, were checked with the readings from the CAEN HV fan-out connected to the sense wire, at the various values of E_{SENSE}. The CAEN fan-out was able to monitor the currents drawn from the sense wire whilst the source was on and off. We found that there was very good agreement between the CAEN monitored $I_{COLLECTED}$ from the sense wire, and the pA measured $I_{COLLECTED}$ from the cathode.

Chapter 5

Results for the gas gain measurements

5.1 Introduction

In this chapter we present our results for the variation of gas gain, G, with surface field E_{SENSE} (in kV/cm), for the SWDC and the two RWDC's. Figures 5.2.1, 5.2.2, and 5.2.3 show the results for the SWDC, the prototype RWDC, and the production RWDC respectively, using the FADC method. Figure 5.2.4 shows the same relationship obtained using the pA method with the SWDC. All graphs are plotted alongside the corrected results of Hessing and Kadel [16] for a sense wire radius of a = 26 μm, with an error on G of 15% [17]. The correction factor of +2.4 comes about because they did not adjust their results for the "tail correction" as discussed below, and that they used N_e = 200, instead of the more accurate value of N_e = 230. These corrections are confirmed by Salmon [17]. We have also plotted the parameterisation of G for the Zeus experiment (Equation 6.1) as quoted by Salmon for a sense wire radius of 25 μm. All the results are tabulated in Tables 5.2.1 to 5.2.4, and are obtained using the Ar {50%}/C_2H_6 {50%} chamber gas mixture.

The graphs are plotted with the best-fit lines shown, the data points that show signs of saturation are ignored in the fits. The error on E_{SENSE} for the SWDC originates from the uncertainty in the cathode and sense wire radius measurements. It was impossible to determine a similar error on E_{SENSE} for the RWDC's due to the complex nature of the electric fields. However, an estimate of this error yielded a value equal to 1% of the magnitude of E_{SENSE} [13].

The FADC method of determining G contained errors originating from the calibration of the data acquisition system (calculated by applying a least squares method to the calibration graphs), the error on the mean of the Fe^{55} X-ray Gaussian histograms, and the error in the determination of N_e. The pA method contained errors from the rate determination, the error on N_e, and from the actual reading of $I_{COLLECTED}$ with the pA.

Beck [18] has shown that for the SWDC, the evaluation of $Q_{COLLECTED}$ by the FADC method (and hence G) must include a correction factor. We reproduce his analysis in Appendix B.

The FADC method is based upon evaluating $Q_{COLLECTED}$ by integrating the contents of the first 30 time bins (= 300 ns) of each Fe^{55} X-ray pulse. This cuts out any charge that may be collected during the larger times of the "tail", and Beck shows that "66% of the electrons generated in the avalanche are still sitting on the anode after 300 ns". This is primarily caused by the slow migrational movement of the positive ions towards the cathode, which produces very slight changes

in the electric fields within the SWDC. This consequently allows the electrons to leave the SWDC via the sense wire, at a rate determined by the rate at which the ions arrive at the cathode. In effect this creates X-ray pulses with very long "tails" extending much further than 300 ns, and it would take about 1.12 ms for all of the avalanche electrons to leave the sense wire.

Beck has concluded that for the nominal conditions of operation for the SWDC (E_{SENSE} = 170 kV/cm, and an ion mobility of 1.7 (cm/s)/(V/cm) for argon ions in argon), "a correction factor of $1/(0.34 \pm 0.03)$ is appropriate for the SWDC FADC charge measurements".

By doubling the nominal values he was also able to show that the correction factor increased to only $1/(0.39 \pm 0.03)$. He then went on to suggest that a similar correction factor would exist with the RWDC FADC charge measurements, that would be much more difficult to determine due to the complex electrostatics within the RWDC's. However it seems likely that its value would not be too different from the previous figure for the SWDC, and so we assumed that the correction factor was the same. The following gas gain results for the SWDC and RWDC FADC charge measurements are given with the relevant correction factors included.

5.2 Results

E_{SENSE} (kV/cm)	Gas gain (G)
164.5 ± 1.5	(1.31 ± 0.18) x 10^4
167.7 ± 1.4	(2.22 ± 0.20) x 10^4
170.9 ± 1.5	(3.06 ± 0.22) x 10^4
174.1 ± 1.5	(5.07 ± 0.28) x 10^4
177.4 ± 1.5	(6.52 ± 0.34) x 10^4
180.6 ± 1.5	(8.48 ± 0.42) x 10^4
183.8 ± 1.6	(10.23 ± 0.49) x 10^4
187.0 ± 1.6	(10.85 ± 0.52) x 10^4
190.3 ± 1.6	(11.59 ± 0.55) x 10^4

Table 5.2.1 Results obtained with the SWDC using the FADC method.

E_{SENSE} (kV/cm)	Gas gain (G)
160 ± 1.6	(1.67 ± 0.18) x 10^4
162 ± 1.6	(2.06 ± 0.09) x 10^4
164 ± 1.6	(2.48 ± 0.20) x 10^4
165 ± 1.7	(2.82 ± 0.13) x 10^4
166 ± 1.7	(2.91 ± 0.21) x 10^4
168 ± 1.7	(3.88 ± 0.18) x 10^4
170 ± 1.7	(4.79 ± 0.22) x 10^4
172 ± 1.7	(5.22 ± 0.29) x 10^4
173 ± 1.7	(6.24 ± 0.33) x 10^4
174 ± 1.7	(6.43 ± 0.34) x 10^4
175 ± 1.8	(7.04 ± 0.36) x 10^4

Table 5.2.2 Results obtained with the prototype RWDC using the FADC method.

E_{SENSE} (kV/cm)	Gas gain (G)
162 ± 1.6	(2.27 ± 0.49) x 10^4
164 ± 1.6	(3.06 ± 0.51) x 10^4
166 ± 1.7	(3.97 ± 0.52) x 10^4
168 ± 1.7	(5.04 ± 0.54) x 10^4
170 ± 1.7	(5.74 ± 0.55) x 10^4
172 ± 1.7	(6.81± 0.58) x 10^4
173 ± 1.7	(6.77 ± 0.59) x 10^4
174 ± 1.7	(7.04 ± 0.58) x 10^4
175 ± 1.8	(7.24 ± 0.60) x 10^4

Table 5.2.3 Results obtained with the production RWDC using the FADC method.

E_{SENSE} (kV/cm)	Gas gain (G)
141.9 ± 1.4	(0.60 ± 0.12) x 10^4
145.1 ± 1.5	(0.93 ± 0.41) x 10^4
148.3 ± 1.6	(1.32 ± 0.44) x 10^4
151.6 ± 1.6	(1.90 ± 0.49) x 10^4
154.8 ± 1.6	(2.86 ± 0.89) x 10^4
158.0 ± 1.5	(4.10 ± 1.68) x 10^4
161.2 ± 1.6	(5.64 ± 1.78) x 10^4
164.5 ± 1.5	(8.31 ± 2.33) x 10^4
167.7 ± 1.4	(11.40 ± 2.62) x 10^4
170.9 ± 1.5	(15.07 ± 4.53) x 10^4
174.1 ± 1.5	(19.71 ± 4.94) x 10^4
177.4 ± 1.5	(23.95 ± 8.60) x 10^4
180.6 ± 1.5	(29.38 ± 8.99) x 10^4
183.8 ± 1.6	(37.09 ± 9.65) x 10^4
187.0 ± 1.6	(5.33 ± 1.13) x 10^5
190.3 ± 1.6	(8.10 ± 4.07) x 10^5
193.5 ± 1.5	(11.59 ± 4.27) x 10^5
196.7 ± 1.5	(15.04 ± 4.52) x 10^5
199.9 ± 1.6	(18.99 ± 4.87) x 10^5

Table 5.2.4 Results obtained with the SWDC using the pA method.

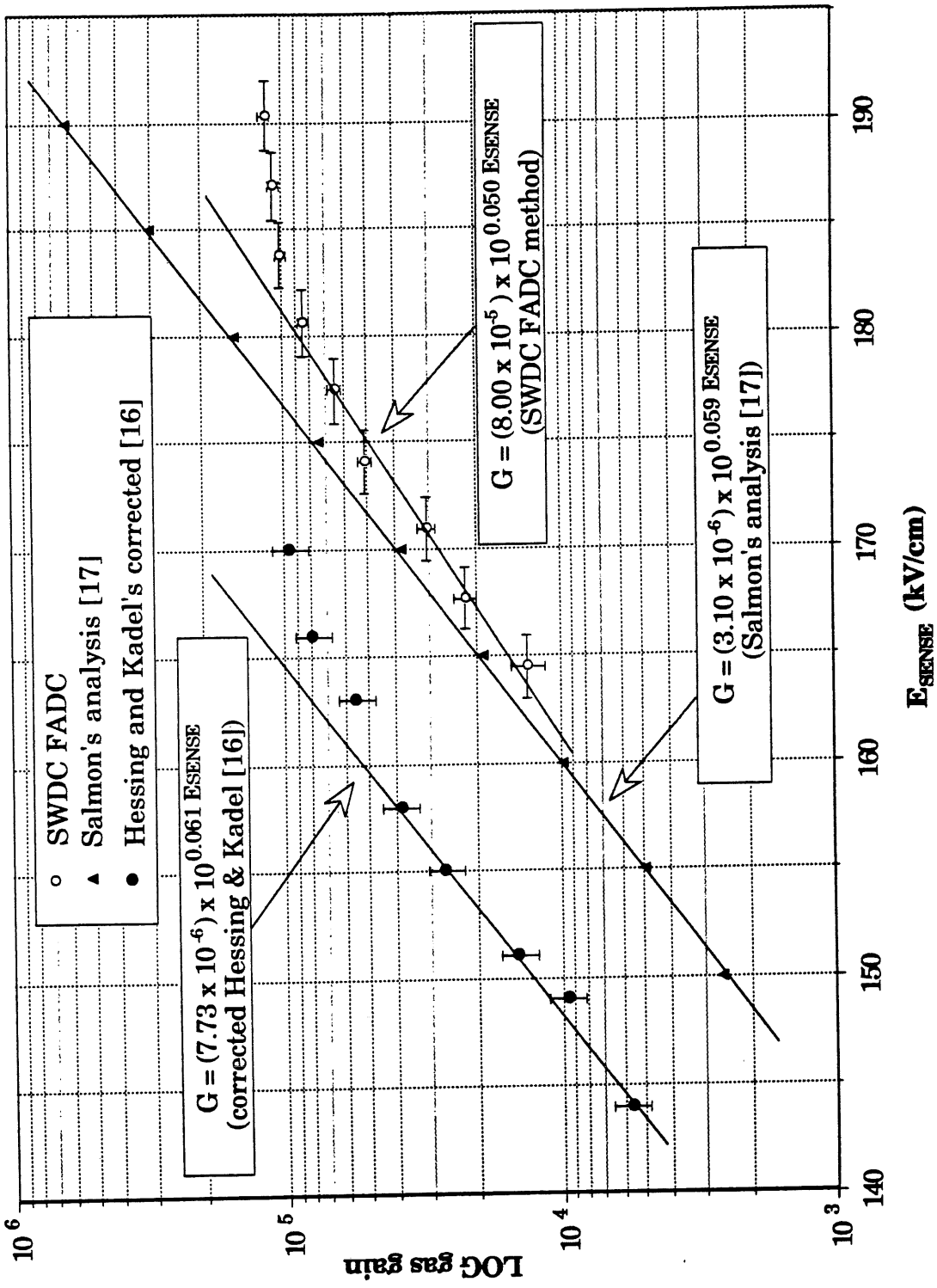

Figure 5.2.1 Relationship between $\log_{10}G$ and E_{SENSE} for the SWDC using the FADC method.

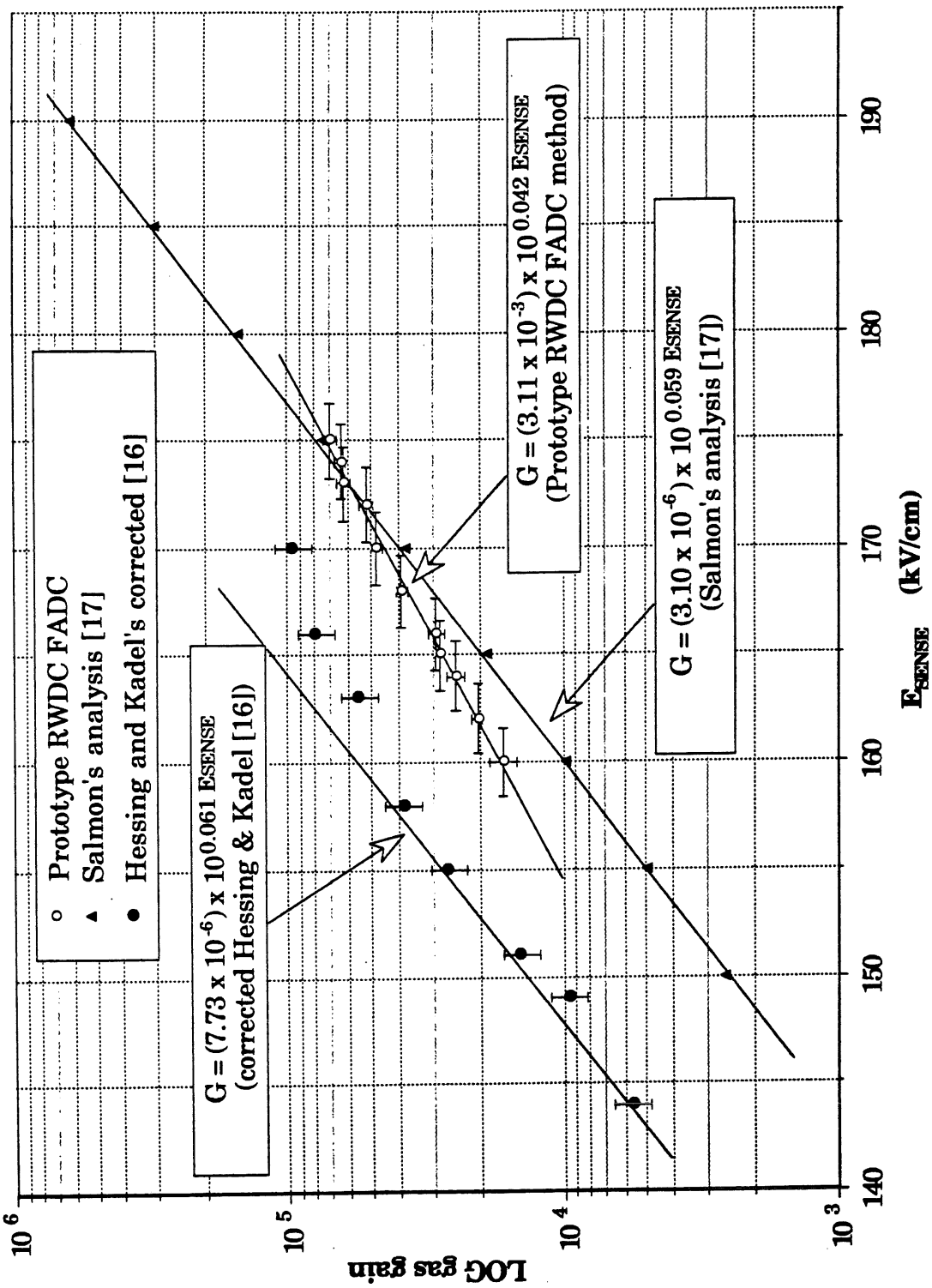

Figure 5.2.2 Relationship between $\log_{10}G$ and E_{SENSE} for the prototype RWDC using the FADC method.

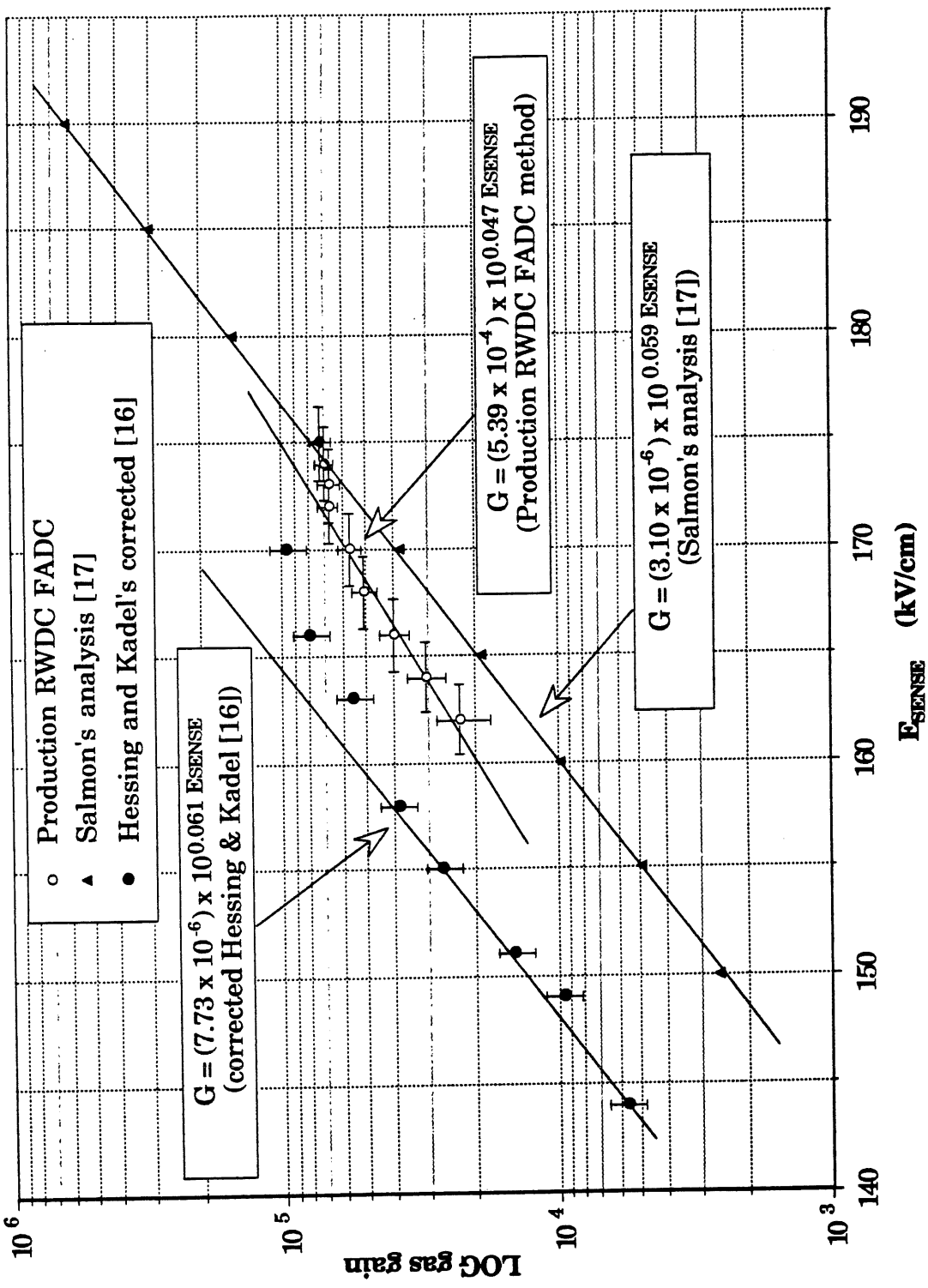

Figure 5.2.3 Relationship between $\log_{10}G$ and E_{SENSE} for the production RWDC using the FADC method.

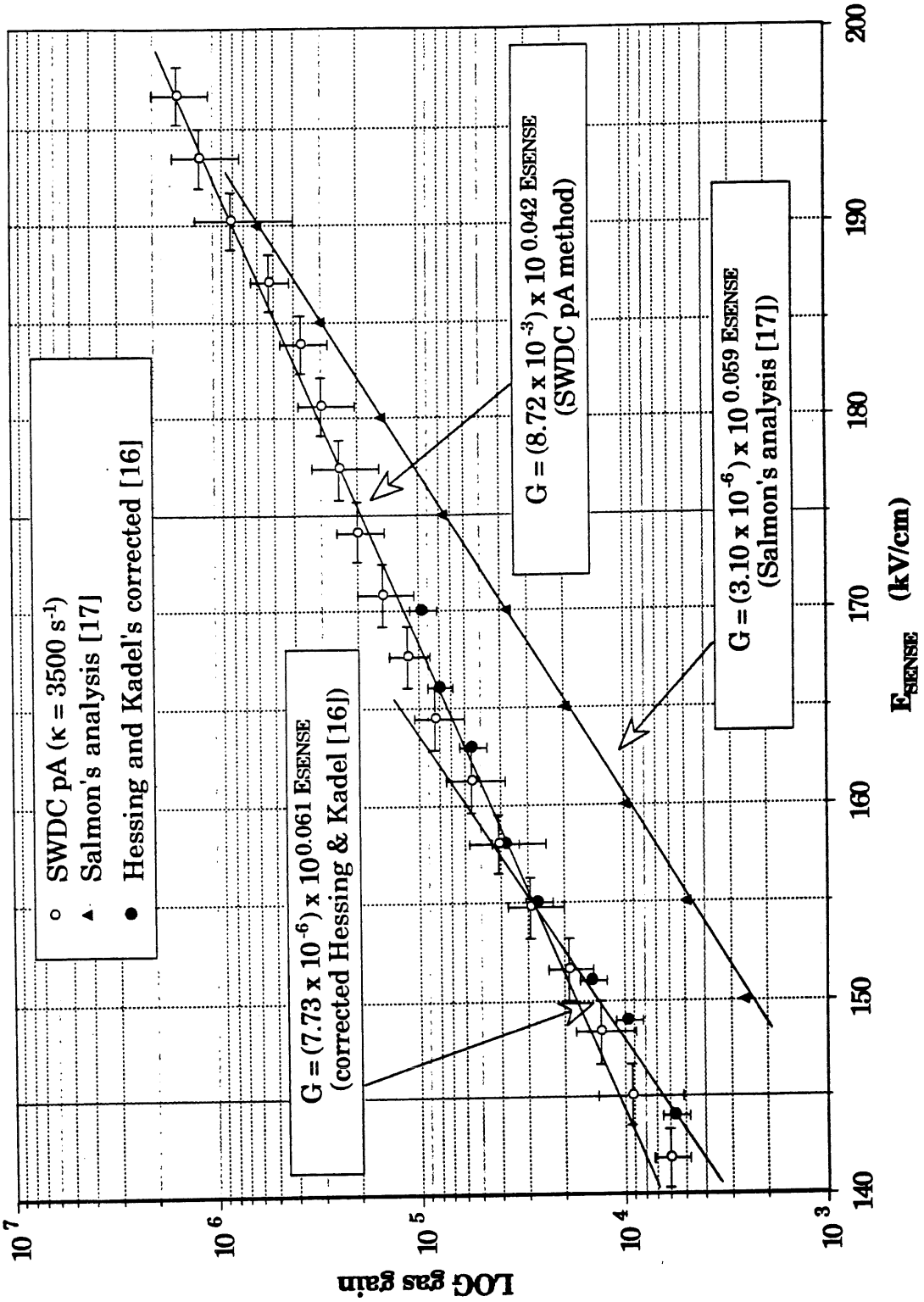

Figure 5.2.4 Relationship between $\log_{10}G$ and E_{SENSE} for the SWDC using the pA method.

Chapter 6

Discussion of results

6.1 Introduction

In Chapter 5 our results are compared to the corrected results of Hessing and Kadel [16], and Salmon's analysis measurements made for the Zeus experiment [17], obtained from an equation derived from the Rose and Korff model [15](Equation 6.1).

$$G = \exp\left[246.8a\sqrt{E_{SENSE}}\left(\sqrt{\frac{E_{SENSE}}{8.5 \times 10^6}} - 1\right)\right] \qquad \textbf{Equation 6.1}$$

Where a is the sense wire radius (we used a = 25 μm), E_{SENSE} is the sense field (measured in V/cm), and G is the gas gain multiplication factor.

Salmon [17] and Beck [18] agree that a "tail correction" factor is required to adjust the gas gain measurements of Hessing and Kadel, such that the complete pulse is analysed. A similar correction factor, as calculated by Beck, is used with the FADC gas gain results. Hessing and Kadel's results are also corrected for the discrepancy in the value of N_e. It is encouraging that our measurements agree to within ~ 1.4 with the theoretical extrapolation by Salmon of his measurements.

6.2 The SWDC pA and FADC results

The pA results for the SWDC are consistently a factor of about 4.5 higher than the FADC results for the same proportional chamber. However, good agreement is observed between the gradients of the two sets of data. The discrepancy between the pA and the FADC results, using the SWDC, is assumed to be due to an unmeasured background caused by some form of secondary interactions. This background would be measured in addition to the current produced by the Fe^{55} X-ray photo-ionisation interactions. The value of $I_{INITIAL}$, which is governed by the rate measurement, has been shown to be independent of these secondary processes, and so the calculation of G by the pA method would lead to a higher value than expected. The pA was found to be reading the currents correctly of the magnitude and frequency of $I_{COLLECTED}$.

In comparison, the FADC method, with the "tail correction" included, only integrated the actual X-ray pulses, and so automatically ignored any background that may exist. It can be shown that a very low, but constant, background would produce an effective DC pedestal level, on top of the base level of the signal. This would not, however, effect the size of the X-ray pulse, as integrated with the FADC method. Furthermore, the FADC's are AC coupled, and so any DC background present would not be seen. Several tests were carried out to try and measure any change in the pedestal level whilst the X-ray source was on and off of the SWDC. If a difference was observed it would have confirmed the existence of a background, however no such change was observed. Although there is no evidence for the existence of this

background, we suspect that the discrepancy between the pA and FADC gas gain results, as measured with the SWDC, is caused by these unobserved secondary processes. Further work is clearly required to observe and measure this background.

Nevertheless, a definite secondary pulse, that did not contribute to the DC background, was observed with the SWDC FADC method. It appeared as a shoulder on the RC tail of the main X-ray pulse shape (Figure 6.2.1), about 200 ns after the start of the main pulse, and only occurred with $E_{SENSE} \geq 185$ kV/cm. It was concluded that this shoulder was caused by the emission of ultra-violet radiation during the gas gain at the high values of E_{SENSE}. The UV light almost instantaneously liberated electrons from the copper cathode of the SWDC, which is a constant distance of 12 mm away from the sense wire. The liberated electrons would then drift to the wire with an average drift time of 20 ns/mm (for argon) and avalanche all at the same instant, producing a pulse delayed by about 200 ns from the main pulse. This effect was not seen whilst using the RWDC's as the copper cathodes do not have the simple geometry of the SWDC. The extra signal produced by these particular UV emissions was clearly included in the FADC technique and the pA technique, and so does not explain the discrepancy between the two sets of results.

A test was completed to check whether the proximity of the Fe^{55} X-ray source on the SWDC caused the chamber to enter a permanent discharge mode, thereby increasing the measured current. This was done by moving the source to and from the aluminium window, whilst measuring $I_{COLLECTED}$ with the pA at the various heights. If such

discharges were produced by the high rate of X-ray events whilst the source was closest to the window, one would expect the readings of $I_{COLLECTED}$ to be different for the upward and downward motion. As the source was moved away, the expected inverse square law relationship was seen, but as the source was returned, the same inverse square law relationship was observed, with no hysteresis. From this we could conclude that the chamber was not permanently discharging due to a high rate of X-rays.

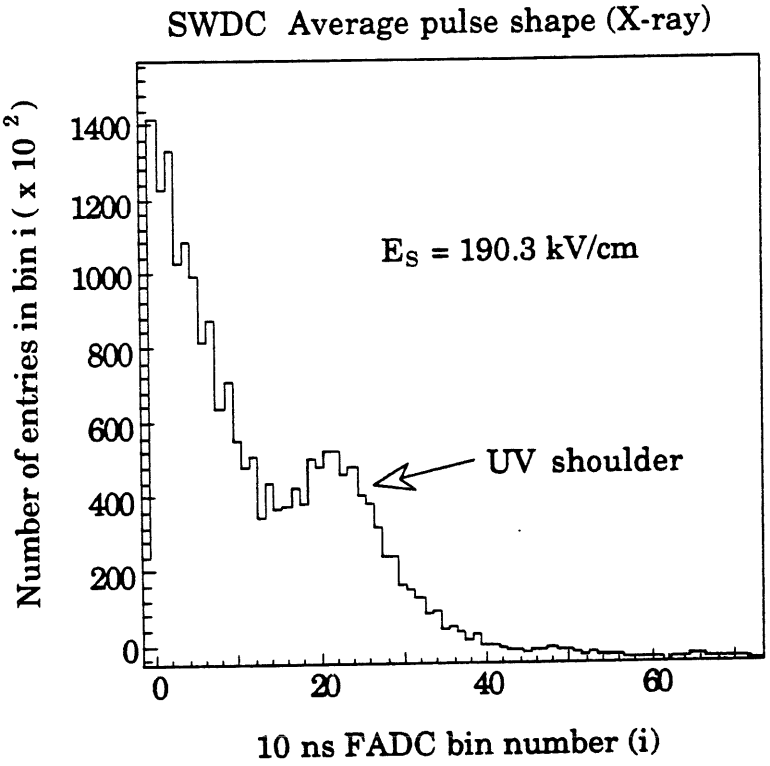

Figure 6.2.1 A typical Fe^{55} X-ray pulse, as obtained with the SWDC FADC method, showing the UV shoulder on the RC tail.

Bateman [23] has experienced similar problems with measuring the current from a proportional chamber, compared to analysing the

individual pulses. He finds that the current measurement is consistently about a factor 3 greater than expected from initial ionisation deposition in gaseous proportional counters. He suggests that this discrepancy is hardly surprising given that in the avalanche the electron temperature is of the order of 1 x 10^5 K, at which much complex chemistry must be possible, which in turn generates additional initial ionisation. Thus the factor by which the current measurements are higher than expectation would depend on the gas mixture used within the chamber.

6.3 The SWDC and RWDC FADC results

The above points, however, do not explain why the RWDC FADC results are on average a factor 1.8 higher than the SWDC FADC results. The oxygen contamination within the SWDC was much lower than that within the RWDC, and as Sauli [14] states that "a 1% pollution of air would remove about 33% of the migrating electrons, per cm of drift", this does not aid in explaining the anomaly.

It is known that the sense field within the SWDC is much better understood than that within the RWDC's, as the determination of E_{SENSE} in the RWDC's is based upon a simple model which has many assumptions included in its working (for example, infinite sense wire length, zero stagger, and non-segmented cathode planes)[13]. It is also clear that E_{SENSE} in the SWDC is much closer to being radial and uniform, whereas in the RWDC's it is radial, but non-uniform due to

the sense wire stagger (which is 200 μm in the prototype RWDC and 285 μm in the production RWDC). It is not known how this would effect the value of G, but it would make the level of G vary around the surface of the sense wire. Therefore, the SWDC FADC results appear to be the more reliable. They will be very helpful in estimating the level of gas gain inside the RWDC's, and hence will aid in the operation of them within the H1 experiment.

6.4 The prototype and production RWDC FADC results

The agreement of the magnitude and gradient of the prototype and production RWDC results, within errors, is very encouraging. The slight difference between the two results can be explained by the fact that there were slight differences in the construction of the two chambers (e.g. the sense wire stagger was slightly smaller, and the sense wire diameter was fractionally larger in the prototype RWDC). The prototype data was recorded in conditions of slightly higher atmospheric pressure than the production data, and in Chapter 7 it can be seen that G is inversely proportional to pressure. These points would result in the prototype RWDC data yielding smaller values of G than the production RWDC data, and this is what is observed.

6.5 Comparison with other results

The SWDC FADC results agree reasonably with Salmon's analysis of gas gain, being only a factor of 1.4 lower. However, upon

inspection of Salmon's experimental data for a sense wire radius of 15 μm, it can be seen that a similar difference exists between his analytical data and his experimental results, for this wire radius. This is very encouraging. The discrepancy between the results of Hessing and Kadel, with ours and Salmon's is not understood.

Chapter 7

Irradiation exposure studies

This chapter is concerned with the effects of cumulative irradiation by a ruthenium β-source on the sense wire of the SWDC, using the Ar {50%}/C_2H_6 {50%} gas mixture at a constant flow rate. The ruthenium source was placed on the aluminium window of the SWDC, and a sense field of 170 kV/cm was maintained. The analysis was carried out over a period of 1.5 months, and the magnitude of $I_{COLLECTED}$, and the peak of the qVt distribution produced by the presence of the source were periodically recorded. As an extra observation on the effects of the β-source, the Fe^{55} X-ray source was intermittently placed on the SWDC, and the same parameters measured. If effects occurred that would deteriorate the quality of the sense wire, the level of G would vary correspondingly. The value of the qVt peak is directly related to the magnitude of the gas gain. $I_{COLLECTED}$ is dependent upon both the gas gain and any background processes that may occur. Figure 7.1 shows a typical energy deposition distribution obtained with the qVt for the β-source.

Deteriorating effects that may exist include the polymerisation "whisker" effect [24], where conductive polyatomic whiskers grow on the sense wire. These could cause surges in $I_{COLLECTED}$ due to the whisker

acting as an extension to the sense wire. Dielectric deposits may also develop on the surface of the wire which would reduce E_{SENSE} and hence G. The greater activity and energy of the β-particles emitted from the ruthenium source, compared to the Fe^{55} X-rays, would speed up any such effects.

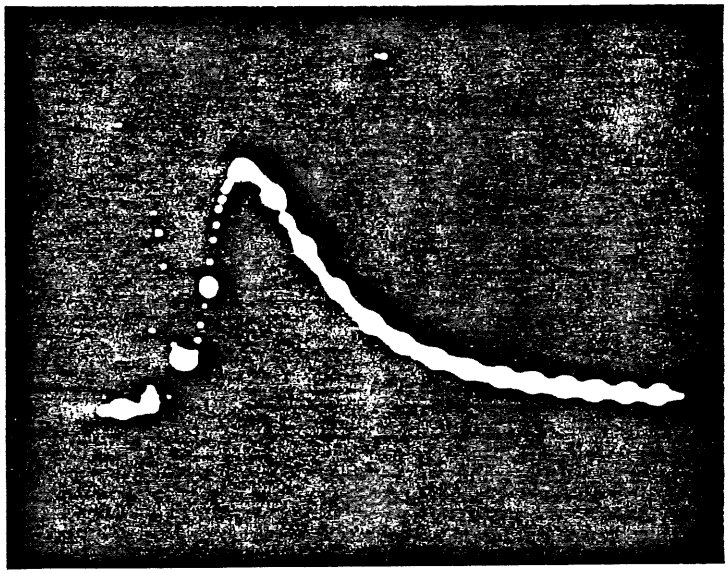

Figure 7.1 The qVt distribution obtained with the ruthenium β-source, with E_{SENSE} = 170 kV/cm.

The variations of $I_{COLLECTED}$, and qVt peak with time (measured in ksecs) are shown in Figures 7.2 and 7.3. The laboratory temperature, and atmospheric pressure (as quoted from the Proudman Oceanographic laboratories at Bidston), were also recorded, and are plotted in Figures 7.2 and 7.3 respectively (the pressure (in mB) is plotted as pressure - 1000 mB to amplify the variation). The current, as

measured with the pA, with no source on the SWDC is also plotted for comparison.

The variations of $I_{COLLECTED}$ and qVt peak for both the ruthenium, and Fe^{55} sources, are consistent with the variations in pressure and temperature. The total charge collected on the sense wire, calculated using the average value of $I_{COLLECTED}$ for the ruthenium source over the 1.5 months, was approximated as 0.26 C/cm, and after this amount of deposited charge no perceivable deterioration had occurred. This is an encouraging result. It is estimated that each sense wire inside the RWDC's will each have a maximum tolerable current flow of 0.1 μA during operation within the H1 experiment, otherwise the electrostatic operating conditions will be prohibitively distorted. With this current the sense wires will be exposed to 0.26 C/cm after approximately 10 years of continuous irradiation (taking 1 year = 3.1×10^7 s and the wedge pair sense wire length = 122 cm within the RWDC's). In practice HERA will deliver luminosity for a fraction of this time.

On inspection of the variations of $I_{COLLECTED}$ and qVt peak with pressure and temperature, for both the ruthenium and Fe^{55} sources, we were able to evaluate the systematic error on G. By choosing regions where no variation in pressure was apparent, we were able to calculate the variation in $I_{COLLECTED}$ caused by the variation of temperature alone, and vice-versa. This yielded a +6% change in G due to a +1 °C change in temperature, and a -7% change in G due to a 10 mB increase in pressure.

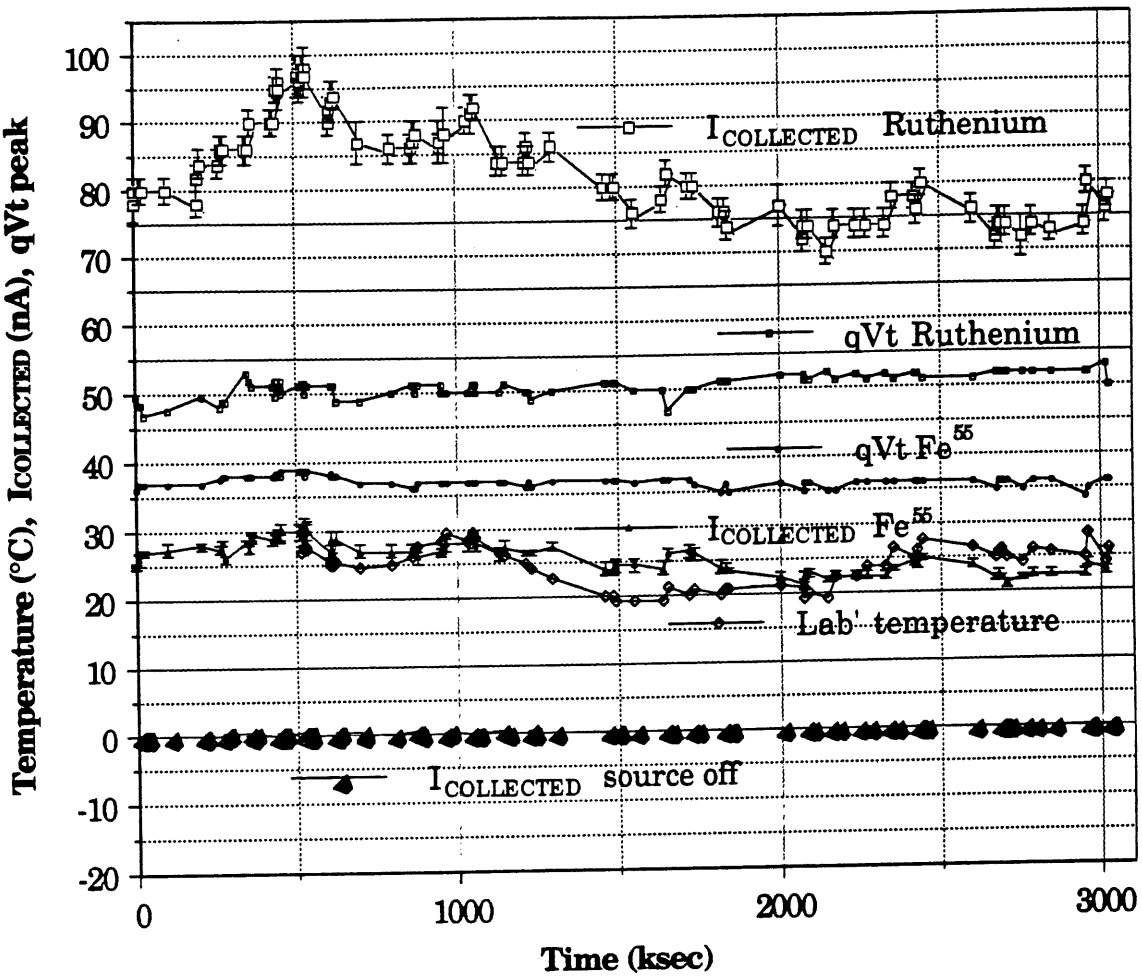

Figure 7.2 The plot of $I_{COLLECTED}$ (measured with the pA) and qVt peak for the Fe^{55} and ruthenium sources, the current with no source ($I_{COLLECTED\ SOURCE\ OFF}$) and temperature (in °C), with time (in ksecs).

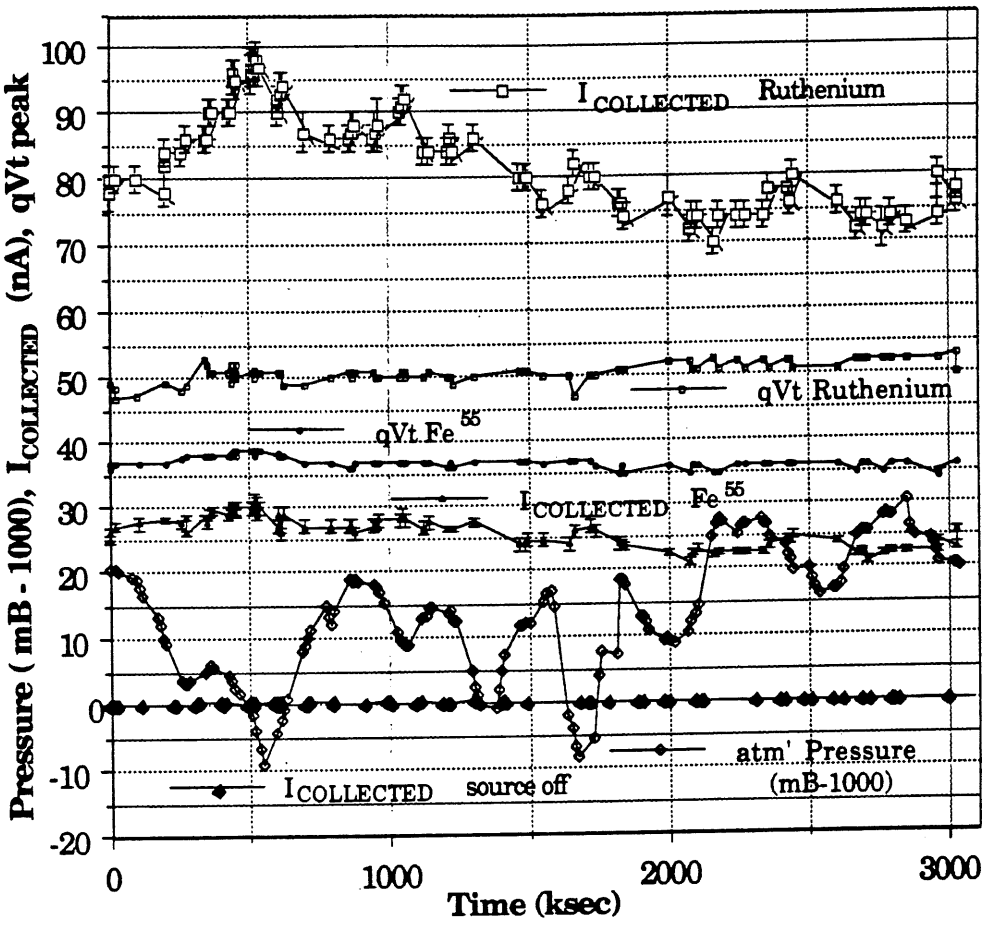

Figure 7.3 The plot of $I_{COLLECTED}$ (measured with the pA) and qVt peak for the Fe^{55} and ruthenium sources, the current with no source ($I_{COLLECTED\ SOURCE\ OFF}$) and pressure (in mB - 1000), with time (in ksecs).

Chapter 8

Conclusions

From our measurements of gas gain, using two H1 radial wire drift chambers (RWDC's), and a single wire drift chamber (SWDC), we are able to conclude that the RWDC's, with the presently established electrostatics, will operate in a stable proportional mode with the expected level of gas gain. At the nominal sense field of 170 kV/cm, with the Ar {50%}/C_2H_6 {50%} chamber gas mixture, the gas gain for a sense wire diameter of 50 μm, is:

$$G = (2.75 \pm 0.22 \pm 0.52\{syst\}) \times 10^4$$

as measured with the SWDC, and analysing the output pulses produced by an Fe^{55} X-ray source with a 6-bit monolithic FADC. The agreement between the SWDC FADC results, and the extrapolation of the results of Salmon [17] for our wire diameter is very encouraging.

A second method of measuring gas gain, using a pico-ammeter to measure the output current from the chamber cathode, appears to provide only an upper limit on G, which is possibly due to the existence of an unmeasured background of secondary processes. The FADC method has been shown to be the more reliable as it does not include this

background in the analysis. Bateman [23] also experiences the same discrepancy between measuring G from the cathode current from a proportional chamber, and by analysing the individual pulses. He suggests that small secondary interactions occurring within the chamber gas cause this difference.

Further measurements should be completed with other X-ray sources of various energies to supplement the results obtained with the Fe^{55} source. The RWDC's will operate with the Xe {30%}/He {40%}/C_2H_6 {30%} gas mixture within the H1 experiment, and so it would be useful to obtain similar results with this mixture.

The irradiation exposure study showed no discernible deterioration of the SWDC sense wire after 1.5 months of continuous exposure to a ruthenium β-source. It was estimated that during this study, 0.26 C was deposited on 1 cm of the sense wire. The RWDC's during operation within the H1 experiment will have a similar amount of charge deposited per cm of sense wire after approximately 10 years of continuous irradiation.

Appendix A

The H1 RWDC preamplifier circuit diagram

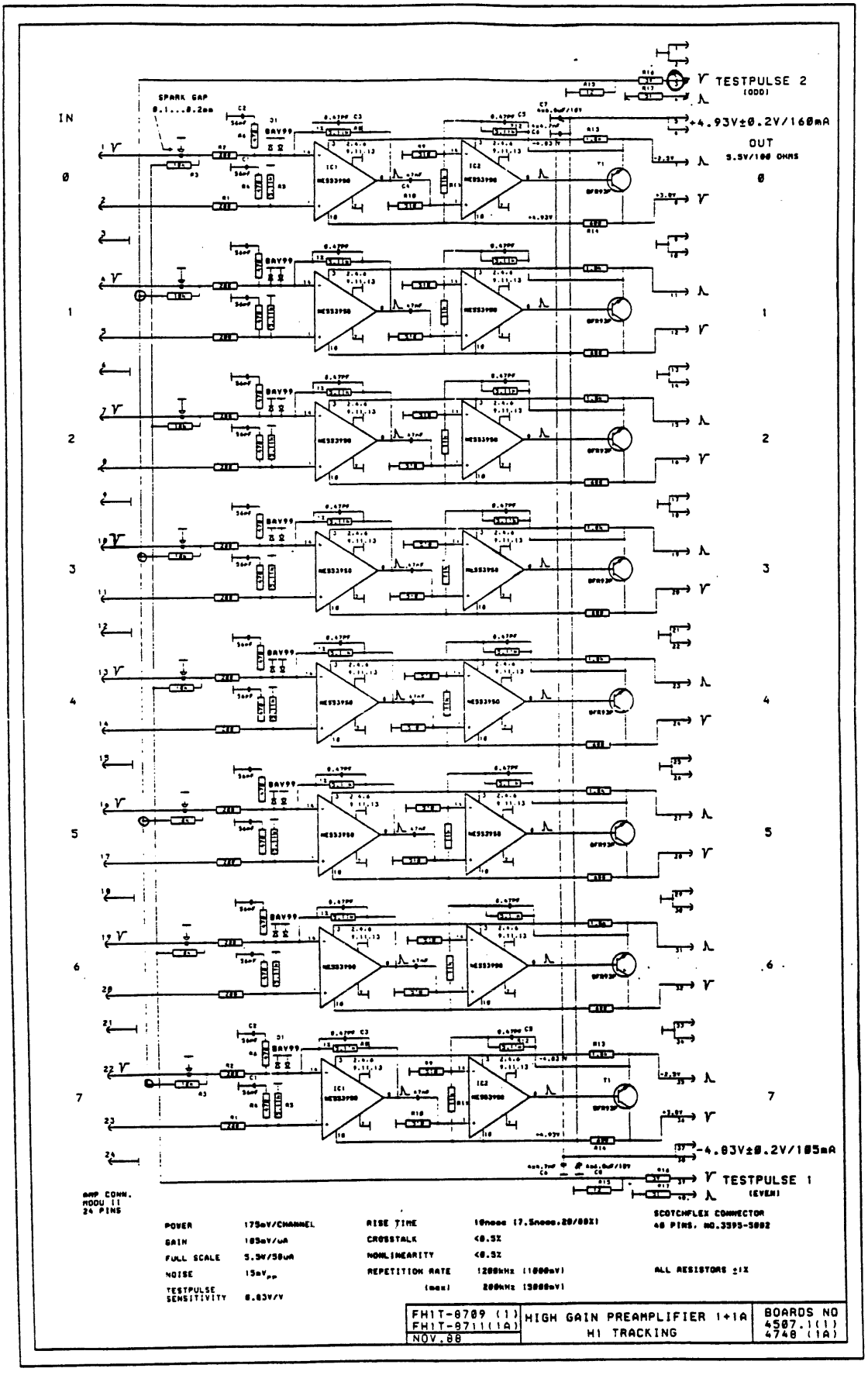
TESTPULSE 2
(ODD)
+4.93V±0.2V/160mA
OUT
SPARK GAP
IN
-4.83V±0.2V/185mA
TESTPULSE 1
(EVEN)
AMP CONN. MODU II 24 PINS
SCOTCHFLEX CONNECTOR 40 PINS, NO.3595-5002
ALL RESISTORS ±1%
POWER 175mV/CHANNEL
GAIN 185mV/uA
FULL SCALE 5.5V/50uA
NOISE 15nV
TESTPULSE SENSITIVITY 8.03V/V
RISE TIME 10nsec (7.5nsec,20/80%)
CROSSTALK <0.5%
NONLINEARITY <0.5%
REPETITION RATE 1200kHz (1000mV)
(max) 200kHz (3000mV)
FH1T-8709 (1)
FH1T-8711(1A)
NOV.88
HIGH GAIN PREAMPLIFIER 1+1A
H1 TRACKING
BOARDS NO
4507.1(1)
4748 (1A)

Appendix B

Pulse Shape from the SWDC

The immediate motivation for this note is to derive a correction to our gas gain measurements, made with the SWDC and FADC system. It will also help us to understand the behaviour of the RWDC and to design future wire chambers.

The following largely agrees with the description given in Sauli's yellow report [14] (pp 44-46), as far as that goes, and is an almost complete reproduction of an internal Liverpool note by Beck [18].

Figure B1 shows to first order (ignoring stray C, L, and R) the circuit used to charge and read out the SWDC. It is an essential feature of this device that it operates at high voltage with a large stored charge, and the passage of an ionising particle produces a very small perturbation on these. This motivates the following notation. The applied high voltage is denoted by capital V and the charge on the electrodes by Q (=CV). For most purposes (in particular the motion of free charges within the SWDC) these can be taken to be constants (Dainton [25] is computing the behaviour at high rate, where this assumption breaks down). For quantities which we can broadly call the signal we will use small letters: v, i, and q. These are the quantities we are most interested in, and we will try to write down the equations so that the 'steady state' V and Q eventually disappear as far as possible.

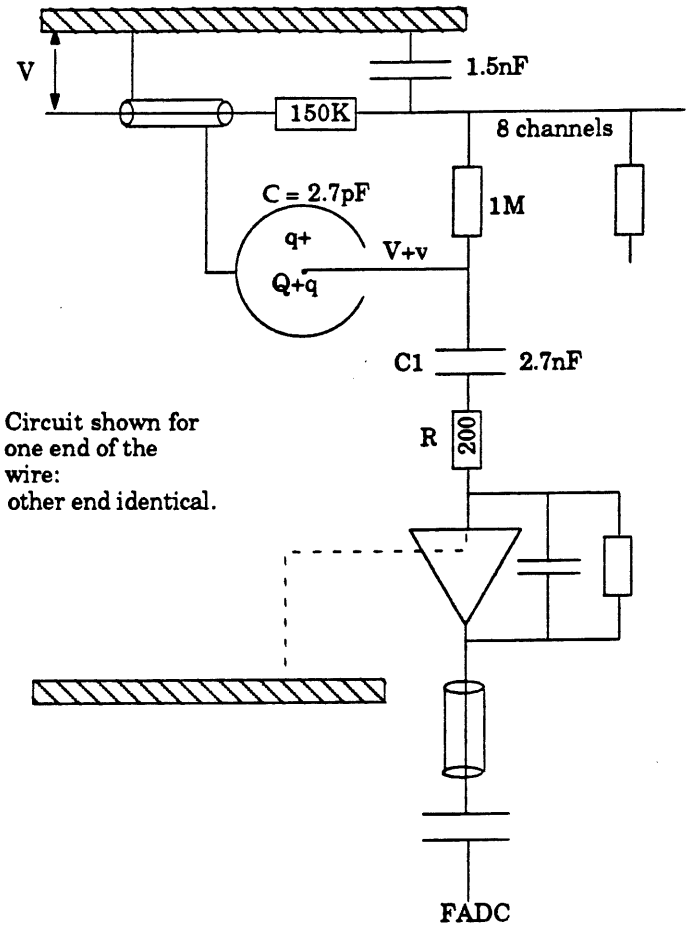

Figure B1 Basic SWDC circuit

In our circuit the SWDC cathode is earthed and high voltage V is applied to the sense wire via resistors and a smoothing capacitor. The steady state charge Q on the SWDC is given by:

$$Q = CV \qquad \textbf{Equation B.1}$$

where (ignoring end effects) $C = 2\pi\varepsilon_o l/\ln(b/a)$.

For the SWDC, length l=0.3m, anode radius a = 25μm, and cathode radius b = 12.7mm the computed capacitance is thus 2.7pF. The electric field inside the SWDC is given by:

$$E = - dV(r)/dr = V/[r.\ln(b/a)] \qquad \textbf{Equation B.2}$$

which is equivalent to Equation 3.2.

An incident charged particle or X-ray produces a number of primary ion pairs. The electrons drift to the anode where they avalanche to give ions with total charge q_+, and electrons, total charge $-q_+$. At this point it is useful to get a feel for the numbers involved. For the SWDC V is typically 2650V so that Q = 7 x 10^{-9} Coulomb. By comparison the ionisation charge is of the order of 100 primary ions x 10^4 gas gain x 1.6 x 10^{-19} electronic charge = 1.6 x 10^{-13} Coulomb. Thus the ionisation charge is only a small fraction (1/(4 x 10^4)) of the steady-state charge. Note that if the SWDC were isolated (e.g. by first allowing it to charge up from the power supply and then cutting all the leads), all the charge from the avalanche would eventually reach the electrodes and the SWDC would become slightly discharged, with a change in anode voltage v = - q^+/C = - 1.6 x 10^{-13}/2.7 x 10^{-12} = - 60 mV.

In order to compute the time development of the signal it is useful to make some approximations (which we can drop later). First we assume that all the primary ionisation arrives simultaneously at the anode (more true for X-rays than for tracks), and that the avalanche is highly localised. So at time t = 0 we start with a cloud of ionisation all at the anode surface (r=a). The electrons move onto the anode (producing a negligible signal in the process - see Sauli) and would sit there indefinitely if the ions were stationary. The ions however move away from the anode under the influence of the electrostatic field, i.e. independently of the external circuitry according to:

$$dr_+/dt = \mu E = \mu V/[r_+ \ln(b/a)] \qquad \textbf{Equation B.3}$$

where μ (the ion mobility) is 1.7 cm/s/(V/cm) for argon ions in argon. The magnitude of the signal is related to the displacement of the ions from a high potential to a lower potential (at larger radius) and the time development therefore depends on how r increases with time, which we now examine.

At the anode the ion drift velocity $dr_+/dt = \mu V/(a\ \ln(b/a)) = 3 \times 10^5$ cm/s (curiously this is slower than the electron drift velocity of 5×10^6 cm/s in a much lower field). Note that the time taken for argon ions to accelerate in free space to this speed is around 70 ps, which is negligible on our time scale.

To find $r_+(t)$ we integrate (Equation B3):

$$\int r_+ \, dr_+ = \mu V/\ln(b/a) \int dt$$

which gives (with the initial condition $r_+(0) = a$):

$$r_+^2 = a^2 + [2\,\mu V/\ln(b/a)]t \qquad \textbf{Equation B.4}$$

The time taken for the ions to reach the cathode at r = b is therefore:

$$t_b = (b^2 - a^2)\ln(b/a) / (2\,\mu V)$$

or to a very good approximation:

$$t_b = b^2 \ln(b/a) / (2\,\mu V) \qquad \textbf{Equation B.5}$$

For the above SWDC parameters this is 1.12 milliseconds. Up to this time the ions are moving towards the cathode and the SWDC is producing a signal.

The next step is to find an expression for the potential difference across the SWDC, which depends on the radial position of the ion cloud

and the charge on the anode. This requires care in defining our variables. Remember that:

q_+ = the positive ion charge generated in the avalanche,

and Q = the charge on the anode in the absence of ionisation.

Now define $q(t)$ = the additional charge on the anode at time t after the avalanche.

Immediately following the avalanche all the electrons are present on the anode so that $q(0) = - q_+$. After a time t the ions have reached $r_+(t)$ and the anode charge $q(t)$ is in general (depending on the external circuit) different from $q(0)$. To find the potential difference across the SWDC in this situation we first use Gauss' theorem to write down the electric field as a function of r. For a contour within the ion radius we see only the charge on the anode, and outside the ion radius we see the ion charge as well, so that:

for $a < r < r_+$: $2\pi\varepsilon l.E = (Q+q)/r$; for $r_+ < r < b$: $2\pi\varepsilon l.E = (q_+ + Q + q)/r$

The P.D. is given by $\int - E.dr$ from a to b:

$$2\pi\varepsilon l.V_{ab} = (Q+q)\ln(r_+/a) + (q_+ + Q + q)\ln(b/r_+)$$

$$= (Q+q)\ln(b/a) + q_+\ln(b/r_+)$$

This can be simplified slightly by substituting the SWDC capacitance from (B1):

$$C.V_{ab} = Q + q + q_+\ln(b/r_+)/\ln(b/a)$$

Now notice that Q/C is the quiescent voltage. The voltage signal, i.e. the additional p.d. across the SWDC, is given by:

$$v = q/C + q_+\ln(b/r_+) / C.\ln(b/a)$$ **Equation B.6**

This (together with the equation of motion (B4)) is as far as we can go without introducing the external circuit. We examine the following simple cases:

(a) Infinite resistance between the anode and cathode

If nothing were connected to the SWDC other than a very sensitive voltmeter no charge would flow from the anode, so $q(t) = - q_+$ and we would see a signal:

$$v = - q_+/C + q_+\ln(b/r_+) / C.\ln(b/a)$$

then substituting from (B4) for $r_+(t)$ and simplifying we find:

$$v = - q_+/2C\ln(b/a) . \ln\{ 1 + 2\mu Vt/(a^2\ln(b/a))\}$$ **Equation B.7**

....which is Sauli's Equation 35 (p45).

(b) A battery only (with no series resistance) across the SWDC

In this case the battery supplies current instantaneously to maintain v = 0. With this condition (B6) becomes:

$$q = - q_+\ln(b/r_+) / \ln(b/a)$$

or:

$$q = - q_+ /2\ln(b/a) . \ln \{b^2/ [a^2 + 2\mu Vt/\ln(b/a)\}$$ **Equation B.8**

This gives $q(0) = - q_+$, and $q(t_b) = 0$ as it should.

We now ask the burning question; what fraction of the total charge has flowed through the external circuit within the first 300 ns (the time for which we integrate our FADC pulses to estimate gas gain) ?

Note that the result will depend on the logarithm of (i.e. it is only a slow function of) V and μ. The values we used previously give:

$$q\,(300ns) = -\,0.66\,q_+$$

i.e. 66% of the electrons generated in the avalanche are still sitting on the anode after 300ns. So we only see 34% of the avalanche charge in this approximation. If μ or V are doubled this figure increases only to 39%. For completeness, the current is given by:

$$i = dq/dt = q_+/\ln(b/a)[a^2\ln(b/a) + 2\mu Vt] \qquad \textbf{Equation B.9}$$

i(0), when the current is a maximum, reduces to Sauli's expression.

(c) A simple approximation to the H1 circuit

Starting with the high voltage part of Figure B1, notice that the SWDC (capacitance C = 2.7 pF) is in parallel with C1 (= 2.7 nF) and both are charged through a 1 MΩ resistor. R(C+C1), the time taken to restore the potential on the SWDC after a discharge, is about 3 ms. This is long on our time scale so we can neglect this part of the circuit in computing the pulse shape. Now the capacitor C1 is 1000 times bigger than C (2000 times allowing for the circuit at both ends of the wire). This means that during a SWDC pulse the p.d. across C1 varies negligibly compared with that across the SWDC: C1 may be treated as a battery, i.e. a source of charge with a fixed p.d. across its plates.

Now we have to make some plausible, hand-waving approximations about the pre-amplifier. We assume that the bottom of the 200Ω load resistor is effectively grounded, and we ignore the pulse-shaping effect of the pre-amp feedback circuit(s) and cables etc downstream. We have some measure of the validity of this from

observing that a 150 ns square test pulse at the top of the load resistor appears at the FADC still with a flat top but with some smoothing (integration) of the front and back edges, with $\tau \sim 30$ns.

With the above approximations we have the circuit shown in Figure B2.

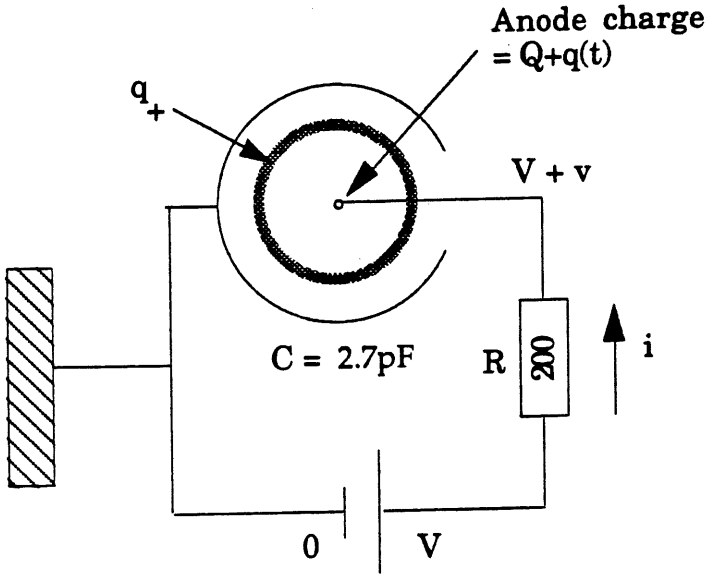

Figure B2 Simplified chamber circuit

Writing Ohm's law for the resistor we have:

$$i = dq/dt = -v/R$$

where (from (B6)) $$v = q/C + q_+ \ln(b/r) / C.\ln(b/a)$$

and the radial coordinate of the ion cloud is given (from (B4)) by:

$$r^2 = a^2 + [2\,\mu.V/\ln(b/a)]\,t$$

Eliminating v and r we have:

$$dq/dt = -q/RC - q_+ / RC.\ln(b/a)\ \ln\{b / \sqrt{[a^2 + 2\mu Vt/\ln(b/a)]}\}$$

Equation B.10

This is our differential equation for q(t), the extra charge on the anode due to the ionisation, in terms of the SWDC capacitance C, load resistor R, inner and outer radii a, b, anode high voltage V and ion charge q_+ and mobility μ.

Note that at t=0 (B10) reduces to: dq/dt = 0/(RC), which is reasonable since for finite RC the current should rise smoothly from zero. In the limit of R -> 0 the equation reverts to (B8)

We can formally integrate (B10) by recognising that:

$$d/dt\,[\, e^{t/RC}.\, q\,] = e^{t/RC}\,[dq/dt + q/RC] \quad \text{(thanks to Dainton [25] for that!)}$$

so that:

$$q = -\,q_+\, e^{-t/RC} / RC.\ln(b/a) \int e^{t/RC} \ln\{b / \sqrt{[a^2 + 2\mu Vt/\ln(b/a)]}\}\, dt$$

We haven't managed to find an analytic solution for this. Note that the exponential term under the integral blows up with time and the solution is finite only because of the reciprocal exponential outside the integral. We therefore pursue a numerical integration. Starting with the initial condition $q = -\,q_+$ and stepping by Δt, dq/dt and hence $q(t+\Delta t)$ are found. This procedure converges as long as Δt is chosen to be less than RC. The accompanying graphs (i and $\int q dt$ vs t on lin-log and log-log scales) are for R = 0 (from eqns B8 & B9), R = 200Ω (the pre-amp input resistance) and R = 5kΩ. The corresponding values of RC are 0, 0.54 ns and 13.5 ns. The normalisation is for 10^6 ion pairs at the wire.

The principal feature is that for t >> RC both current and integrated charge are insensitive to RC: at 300ns in all three cases the fraction of anode charge collected is 34%, and the current is about 0.06mA, which is 2% - 10% of the peak current. Another obvious

feature at large t is the '1/t tail' in current, which appears as straight line behaviour of i(t) in the log-log plot and for ∫qdt in the lin-log plot. It appears that for large time intervals the signal is dominated by the motion of the ions in the SWDC. This is not surprising since the only other effect we have introduced is that of smoothing with a relatively small time constant: the effect of the series RC on the movement of charge round the external circuit is to delay and average its response on a time scale of RC.

It is doubtful whether accounting in detail for the pre-amplifier feedback and downstream components would significantly change the above picture, although it should help explain why the observed pulses correspond most closely to the 5kΩ curve (RC around 13 ns). In practice the primary ionisation does not avalanche simultaneously: it is spread over 80ns or so for 1cm track segments and even for X-rays may have a significant extent, due to variation in drift path to the anode. This does motivate a very close look at X-ray pulse shapes. But note that the fraction of charge collected after 200 ns (e.g. for the trailing edge of an avalanche) is about 30%, which is not very different from the 34% after 300ns.

We conclude that a correction factor of $1/(0.34 \pm 0.03)$ is appropriate for the SWDC FADC charge measurements.

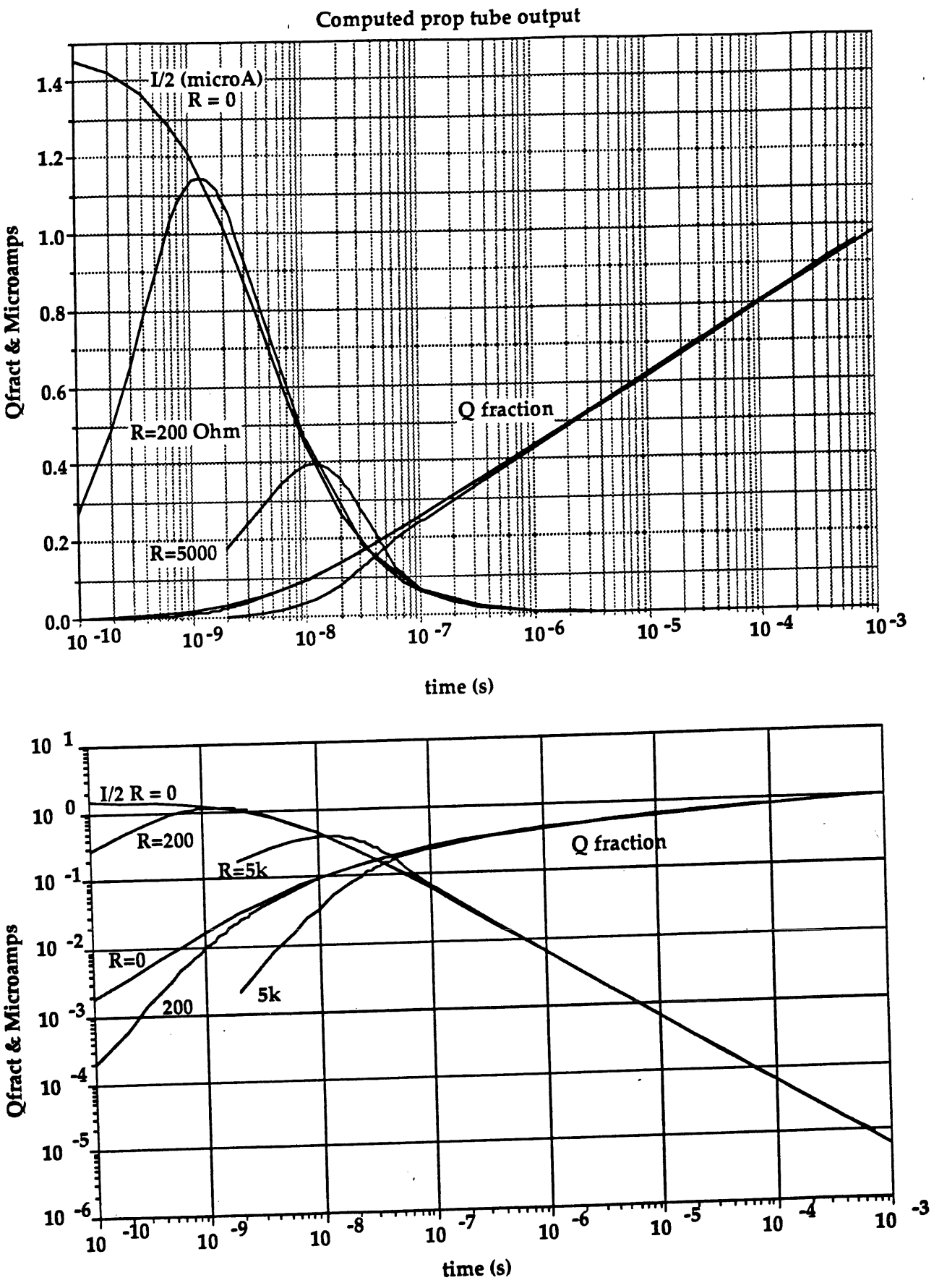

Figure B3 Computed proportional tube output

Supplement

Gas Gain results with other gas mixtures

S.1 Introduction

This supplement documents results which were obtained within the period 22/4/91 to 31/5/91. They were obtained using exactly the same equipment and data acquisition techniques as with those documented in "Some studies of gas gain measurements in proportional drift chambers" [a], however I only used the SWDC with the FADC and pA methods as described in [a]. The results were divided into three sets:

(i) Ar {50%}/C_2H_6 {50%} as a comparison to the data documented in [a], obtained with both FADC and pA methods using the SWDC.

(ii) Ar {90%}/CH_4 {10%}, obtained with both FADC and pA methods using the SWDC.

(iii) Xe {20.0%}/He {30.2%}/C_2H_6 {49.8%} obtained with both FADC and pA methods using the SWDC.

The Ar {50%}/C_2H_6 {50%} FADC data was completed at similar sense fields as with the data in [a], however very high noise levels restricted the range to that of 174.1 kV/cm < E_{SENSE} < 190.3 kV/cm. The Ar {90%}/CH_4 {10%} mix causes a much greater gain at much lower sense fields, and so the range of E_{SENSE} was shifted down by 30 kV/cm to

prevent overflows with the FADC data. Again excessive noise levels restricted the range of results attainable. The pA data seemed not to be affected by the high noise levels and so the complete range was accessible with all gases.

The value of N_{ip} will clearly be different with the different gas mixtures. Using the same methods and values from Sauli [b], we are able to evaluate the following:

$$W_{ip}\,(Ar\ \{90\%\}/CH_4\ \{10\%\}) = 26.2\ eV$$

$$W_{ip}\,(Xe\ \{20.0\%\}/He\ \{30.2\%\}/C_2H_6\ \{49.8\%\}) = 29\ eV$$

Which yield:

$$N_{ip}\,(Ar\ \{90\%\}/CH_4\ \{10\%\}) = 225$$

$$N_{ip}\,(Xe\ \{20.0\%\}/He\ \{30.2\%\}/C_2H_6\ \{49.8\%\}) = 200$$

These values are used in the calculation of G as described in [a].

S.2 Data Taking

The Ar $\{50\%\}/C_2H_6$ $\{50\%\}$ FADC data was taken first, it was immediately noticeable that the noise levels were much greater than those previously. Various attempts were made to reduce this level by shielding etc, but with no avail. So we simply had to ignore the sense fields below 174.1 kV/cm, and concentrate on the higher fields. Typical pulses with this gas can be seen in Figures S1 and S2. On completion of these results, the pA data was obtained. The data from these

measurements is shown graphically in Figure S3 (compared with the Ar {50%}/C_2H_6 {50%} data from [a]), and Figure S4 (along with the data with Ar {90%}/CH_4 {10%} and Xe {20.0%}/He {30.2%}/C_2H_6 {49.8%}). The 'tail correction' as described in [a] is included with the FADC data (equal to 1/0.34 [c]). On analysis of the FADC data we could see the 'shoulder' on the pulse shapes at the higher values of E_{SENSE} (i.e. $E_{SENSE} \geq 185$ kV/cm), delayed 240 ns after the start of the pulse (Figure S5), as in [a]. The data agreed very well with both the FADC and pA results from the previous set (1990)

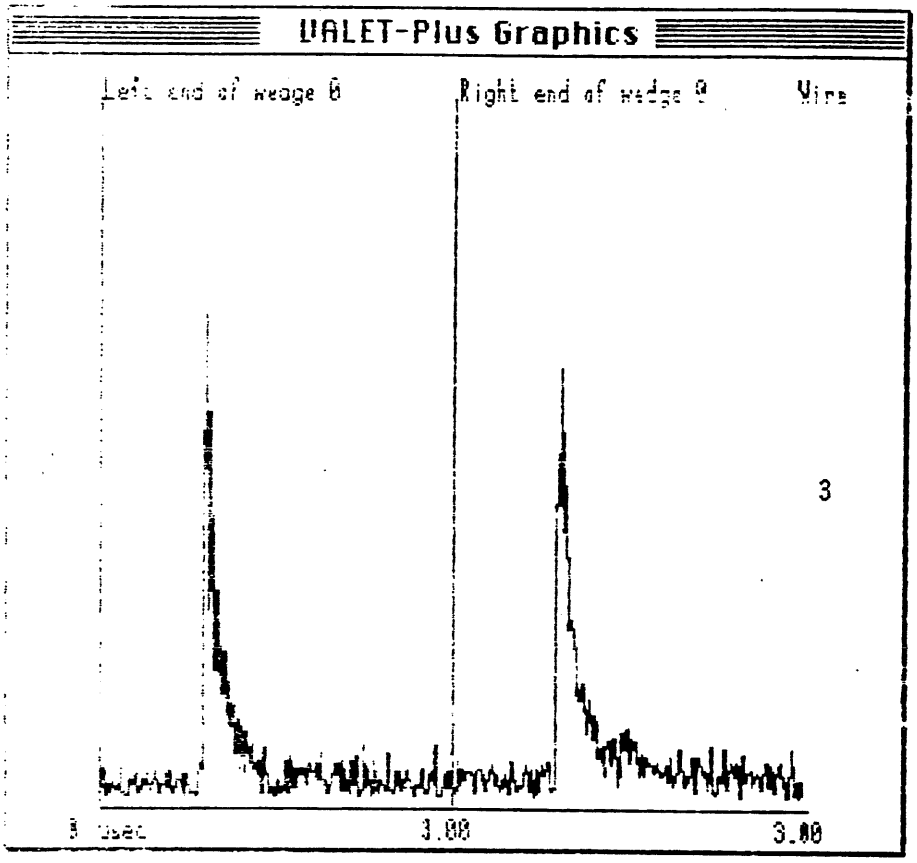

Figure S1 A non-linear digitised Fe^{55} X-ray pulse from the SWDC, showing the left and right components of the pulse (Ar {50%}/C_2H_6 {50%}), E_{SENSE} = 174 kV/cm.

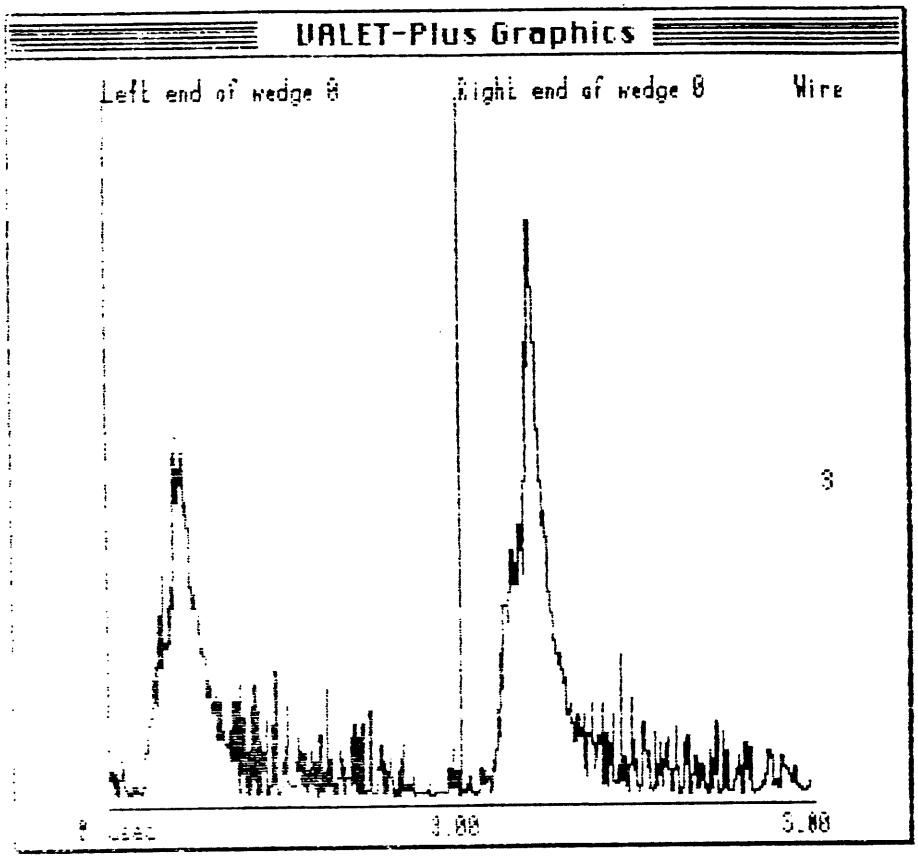

Figure S2 A non-linear digitised Cosmic ray pulse from the SWDC, showing the left and right components of the pulse (Ar {50%}/C_2H_6 {50%}), E_{SENSE} = 174 kV/cm.

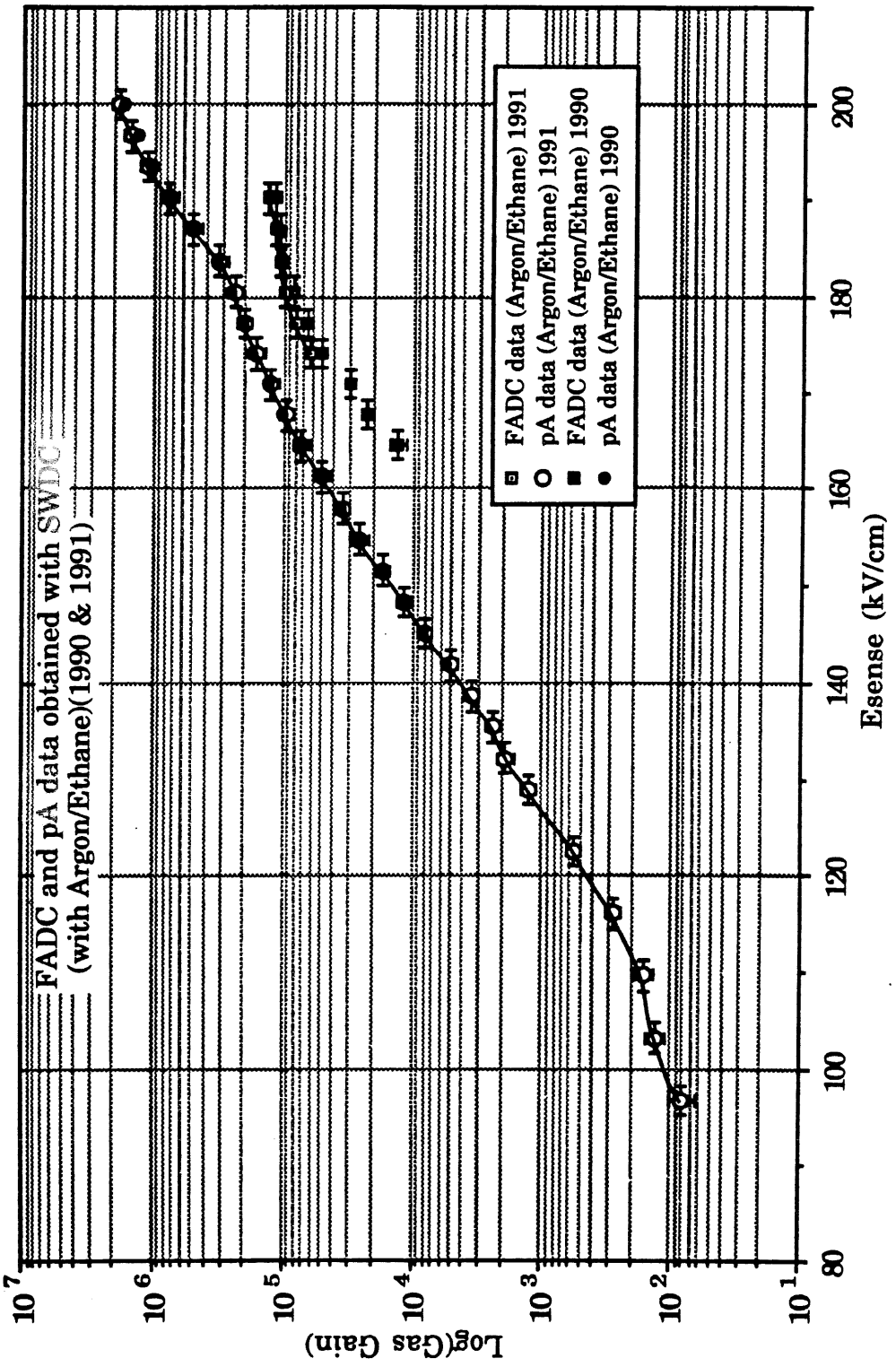

Figure S3 FADC and pA results with the SWDC with Ar {50%}/C_2H_6 {50%} (data from 1990 and 1991).

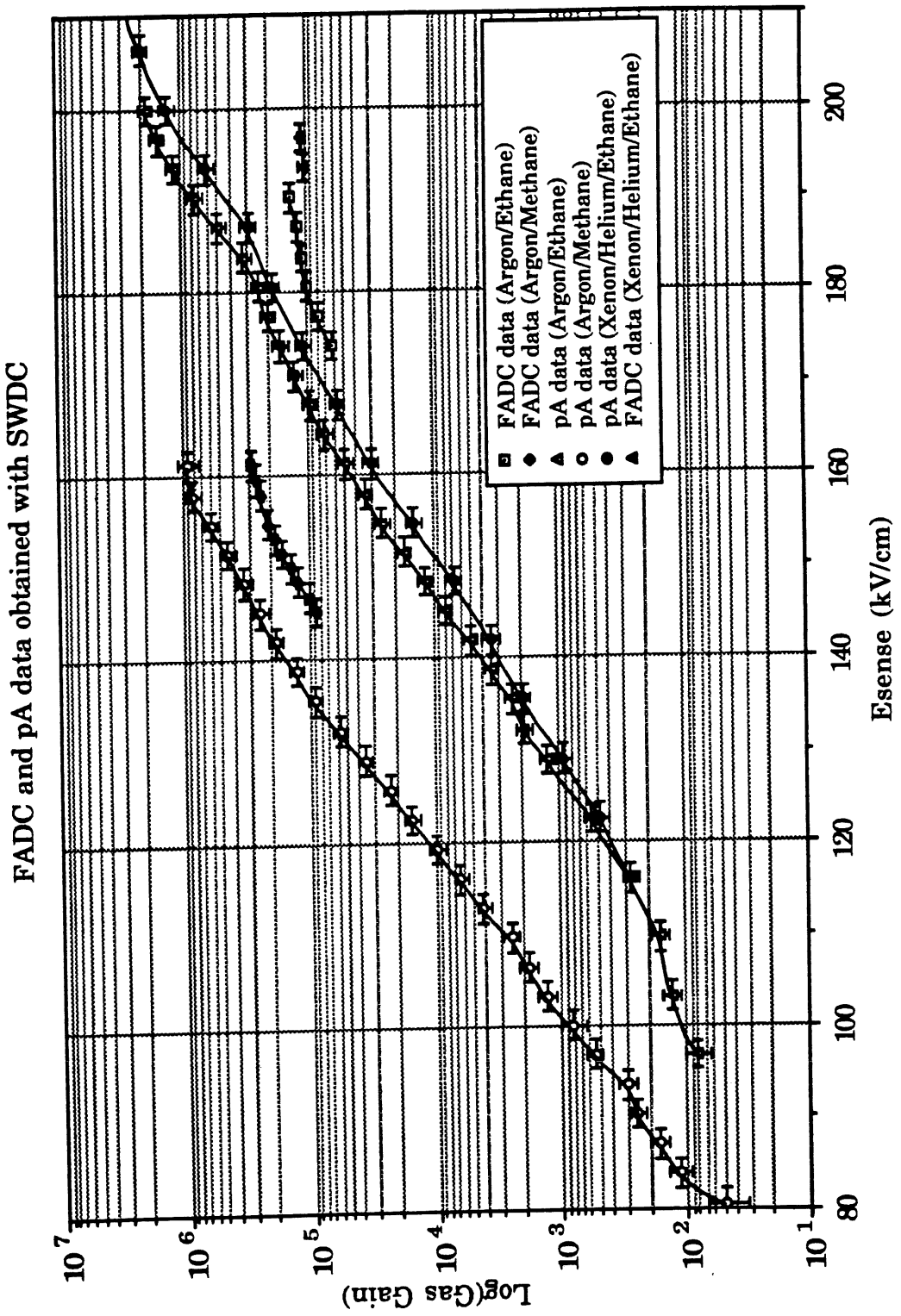

Figure S4 FADC and pA results with the SWDC with Ar {50%}/C_2H_6 {50%}, Ar {90%}/CH_4 {10%}, and Xe {20.0%}/He {30.2%}/C_2H_6 {49.8%} (data from 1991).

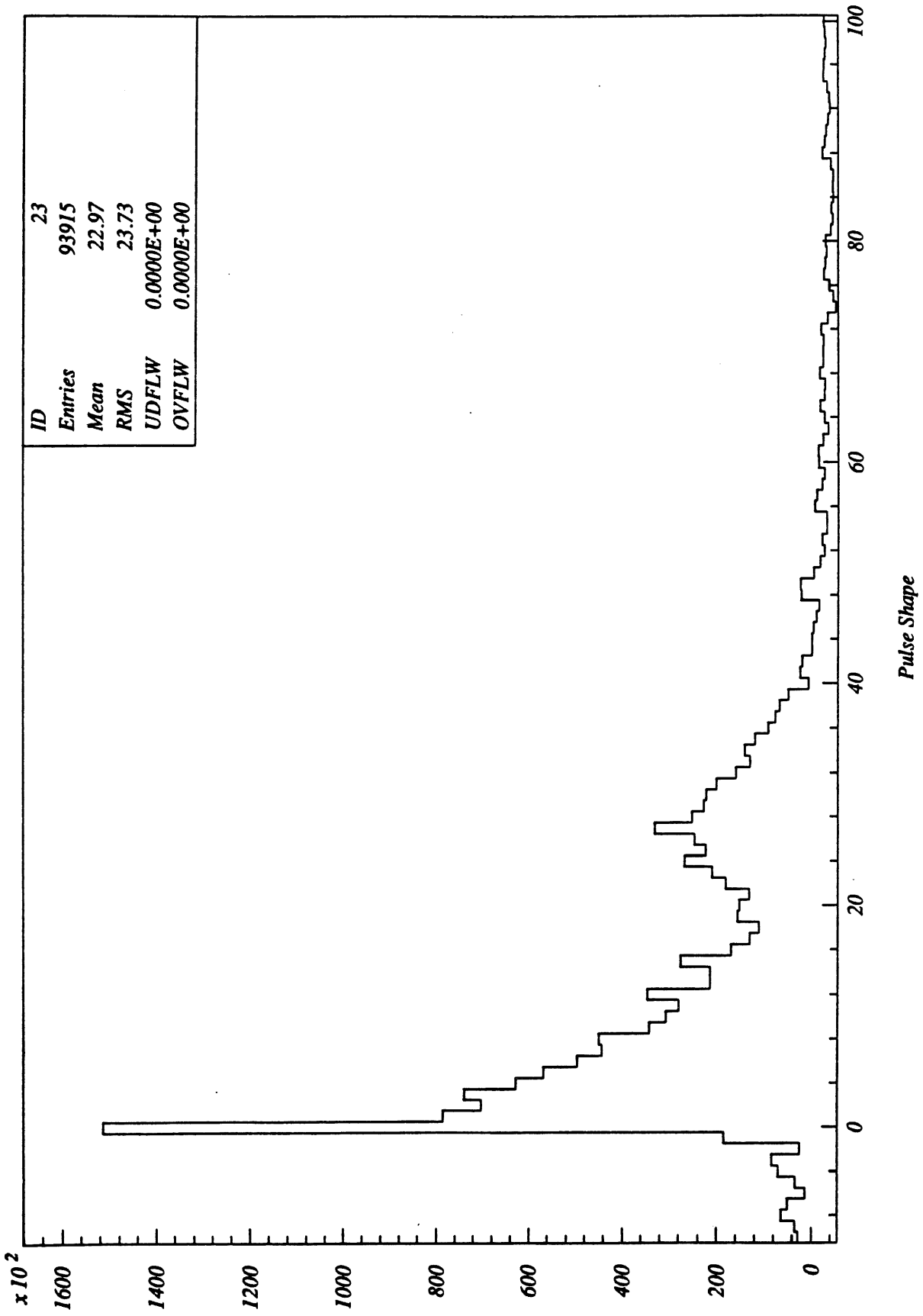

Figure S5 Analysed pulse shape for Ar {50%}/C_2H_6 {50%} showing 'bump', E_{SENSE} = 190.3 kV/cm.

The second set of results, obtained with Ar {90%}/CH_4 {10%}, were again completed with both the FADC and pA methods. Typical pulses can be seen in Figure S6. In Figure S7 we can see a definite 'bump' that appears with $E_{SENSE} \geq 150$ kV/cm. This sometimes becomes very large (Figure S8), and even appears larger than the original pulse itself in some cases (Figure S9). Not only that, but we sometimes see multiple pulse with 3 to 5 so called 'bumps', which quite clearly cannot be described as bumps no longer (Figure S10). As E_{SENSE} is increased these occur more frequently. On analysis the shoulder can be easily seen (Figure S11), and this time appears after 400 ns, this correlates with an average electron drift velocity of 40 ns/mm within Ar {90%}/CH_4 {10%}. This can be looked at as clear evidence for the existence of the "secondary processes" that (as we assume) causes the non-agreement of the pA and the FADC results. The results are shown graphically in Figure S5 along with the equivalent results obtained with Ar {50%}/C_2H_6 {50%} and Xe {20.0%}/He {30.2%}/C_2H_6 {49.8%}. The same correction factor is used with the FADC results.

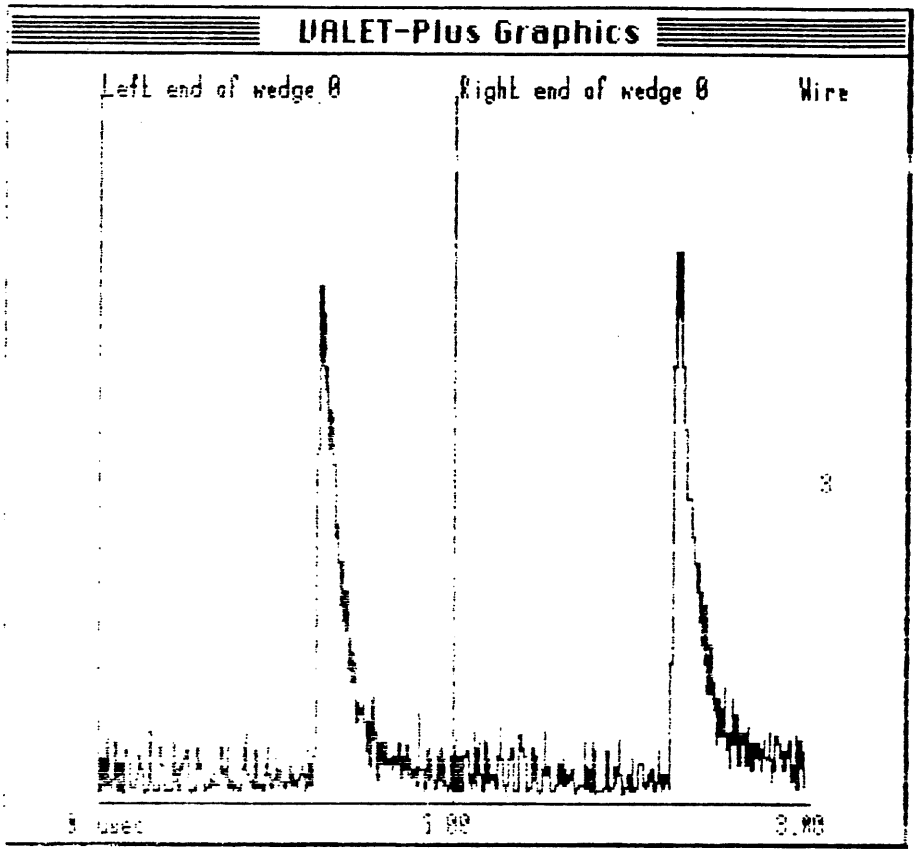

Figure S6 A non-linear digitised Fe^{55} X-ray pulse from the SWDC, showing the left and right components of the pulse (Ar {50%}/CH_4 {50%})(E_{SENSE} = 145 kV/cm).

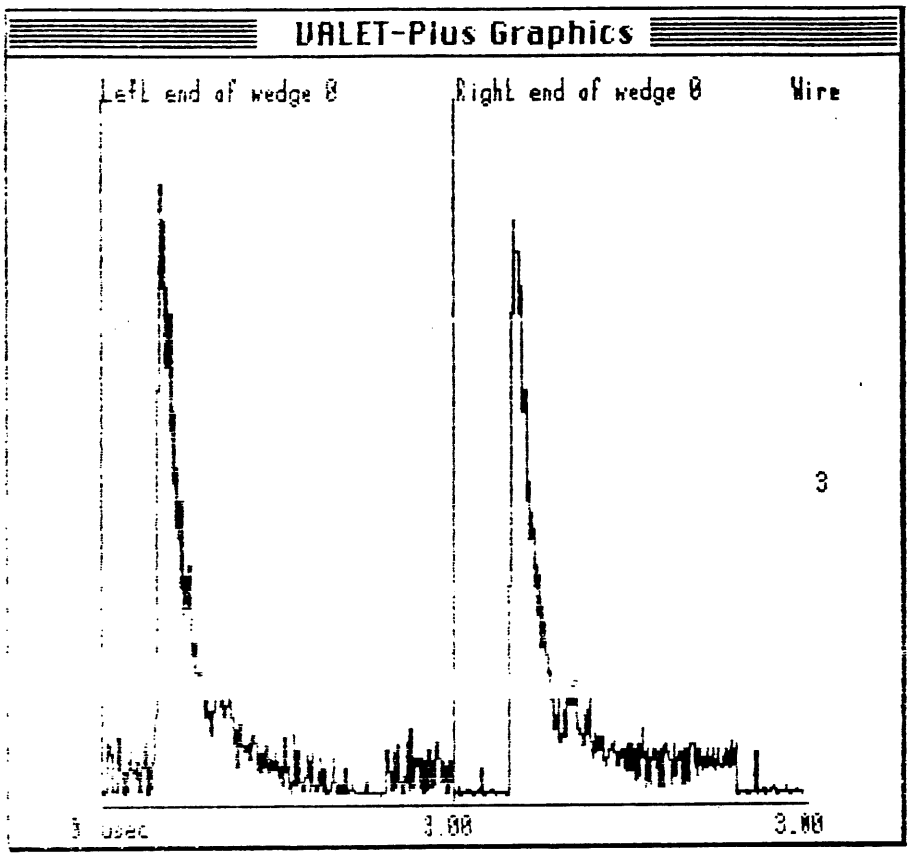

Figure S7 A non-linear digitised Fe^{55} X-ray pulse from the SWDC, showing the left and right components of the pulse (Ar {50%}/CH_4 {50%})(E_{SENSE} = 150 kV/cm). Showing small 'bump'.

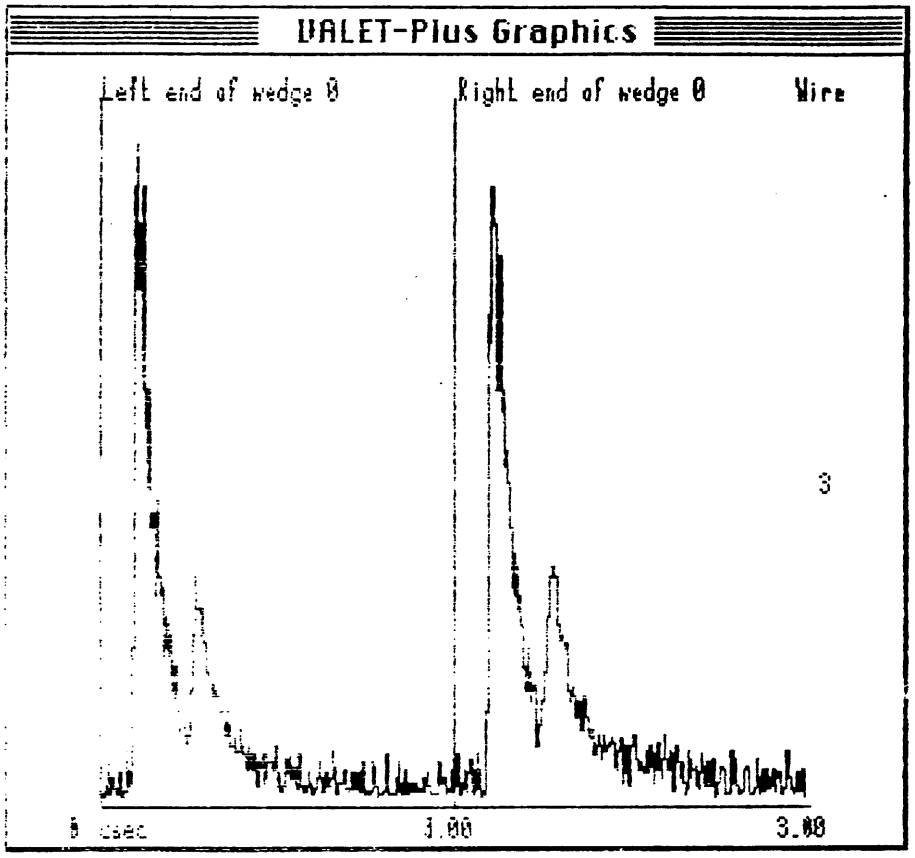

Figure S8 A non-linear digitised Fe^{55} X-ray pulse from the SWDC, showing the left and right components of the pulse (Ar {50%}/CH_4 {50%})(E_{SENSE} = 155 kV/cm). Showing larger 'bump'.

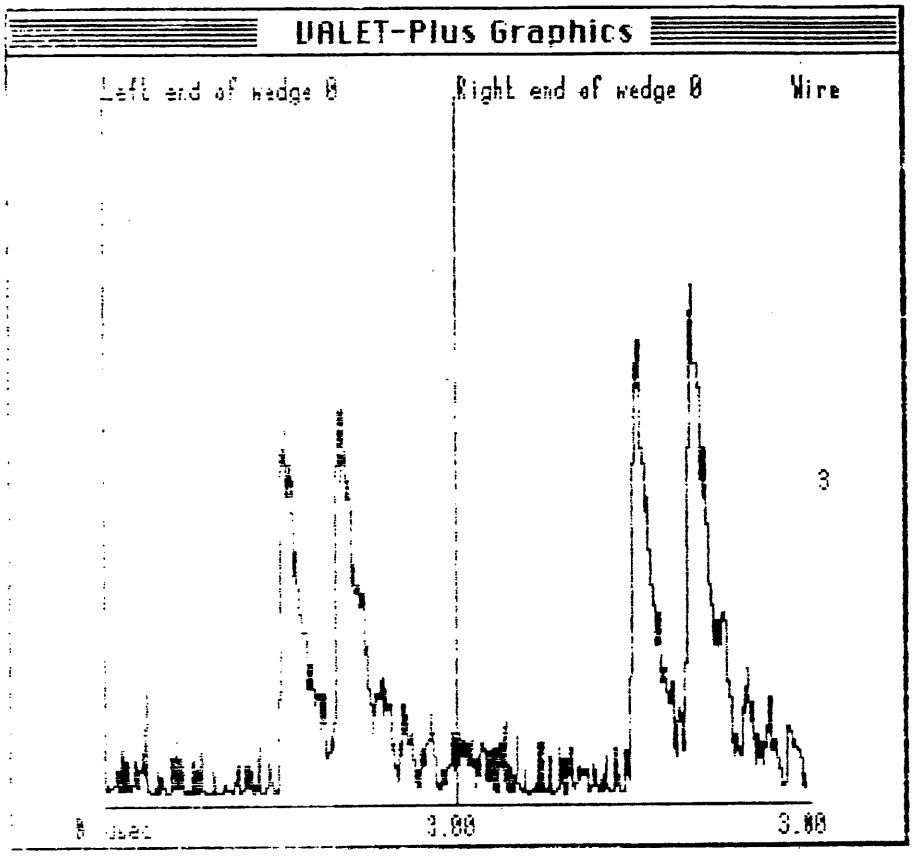

Figure S9 A non-linear digitised Fe^{55} X-ray pulse from the SWDC, showing the left and right components of the pulse (Ar {50%}/CH_4 {50%})(E_{SENSE} = 155 kV/cm). Showing 'bump' which is larger than the main pulse.

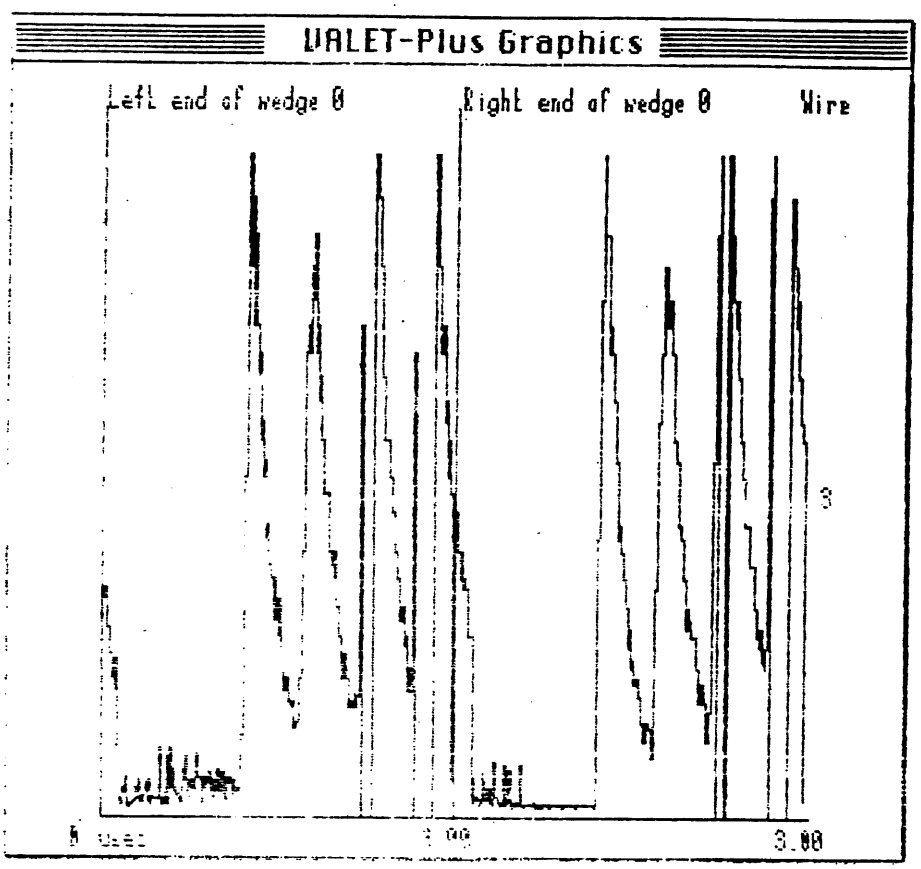

Figure S10 A non-linear digitised Fe^{55} X-ray pulse from the SWDC, showing the left and right components of the pulse (Ar {50%}/CH_4 {50%})(E_{SENSE} = 160 kV/cm). Showing multiple 'bumps' which are larger than the main pulse.

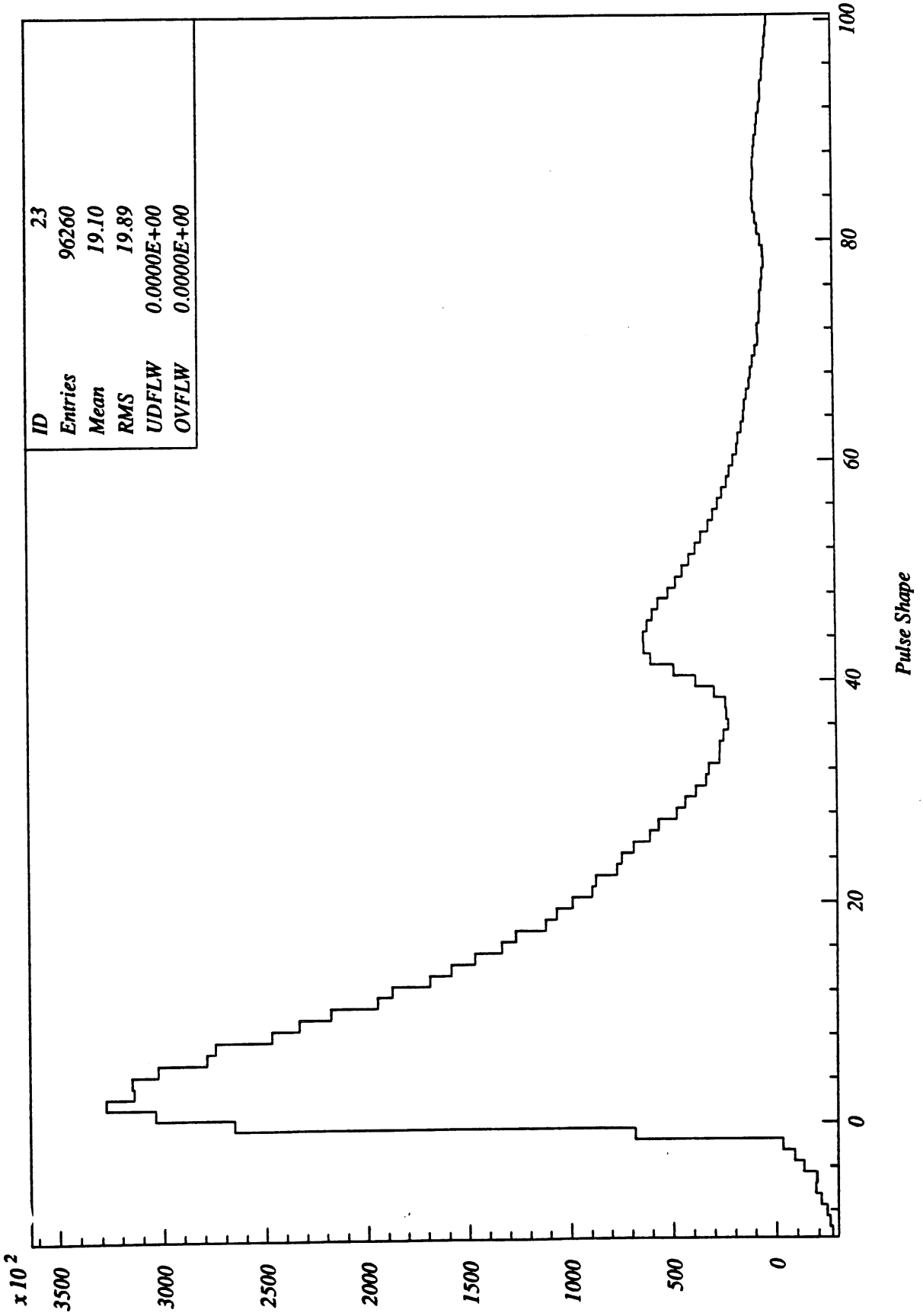

Figure S11 Analysed pulse shape for Ar {50%}/CH_4 {50%} showing 'bump', E_{SENSE} = 160 kV/cm.

The third set of results, obtained with Xe{20.0%}/He{30.2%}/C_2H_6 {49.8%}, were taken with great haste due to the expense of the Xenon gas (the bottle cost around £600!). The pA results were completed successfully, however the FADC runs were over-run with noise. This made these results impossible to complete, and hence only 2 sets of FADC data are documented. At E_{SENSE} = 190.3 kV/cm we found that a huge range of pulse shapes were being recorded, from small definite X-rays to X-rays that caused the system to overflow, this obviously ruined any chance of evaluating the gas gain.

S.3 Conclusion

The factor difference between the FADC and pA results with the various gases is as follows (pA gas gain / FADC gas gain):

Ar {50%}/C_2H_6 {50%}	= 2.6
Ar {90%}/CH_4 {10%}	= 2.9
Xe{20.0%}/He{30.2%}/C_2H_6	Unable to evaluate

This shows that the secondary processes that are assumed to produce the difference between the FADC and pA data are greater with Ar {90%}/CH_4 {10%}. This is not conclusive proof of the existence of these 'background' processes, but it does show that the discrepancy is not due to 'systematics'. It was expected that the difference would be larger with Ar {90%}/CH_4 {10%} as the amount of quencher is proportionally smaller.

S.4 References

[a] D.G. Nunn, "Some studies of gas gain measurements in proportional drift chambers", M.Sc. thesis, University of Liverpool, UK, 1991

[b] F. Sauli, Principles of operation of multiwire proportional and drift chambers CERN 77-09 (1977)

[c] G.A. Beck (private communication) Internal Liverpool note on Pulse Shapes